

Laser Induced Phased Arrays for Volumetric Imaging

PhD Thesis

Peter Lukacs

Centre for Ultrasonic Engineering (CUE)

Electrical and Electronic Engineering

University of Strathclyde, Glasgow

January 11, 2023

This thesis is the result of the author's original research. It has been composed by the author and has not been previously submitted for examination which has led to the award of a degree.

The copyright of this thesis belongs to the author under the terms of the United Kingdom Copyright Acts as qualified by University of Strathclyde Regulation 3.50. Due acknowledgement must always be made of the use of any material contained in, or derived from, this thesis.

Abstract

Ultrasonic phased array imaging is an effective tool to detect and characterise defects for NDE relevant applications. In order to achieve ultrasonic focusing in all dimensions for volumetric imaging, two dimensional arrays are required. However, in various applications, currently available transducer-based phased arrays are challenging to apply, such as in extreme environments, in places of restricted access or on objects with complex geometries.

Laser ultrasound is an alternative transduction method that utilises lasers for generation and detection of ultrasound. It is able to address various current challenges of NDE, as it is remote, non-contact, couplant-free, has a small footprint and can adapt to complex shapes. In comparison to transducers, the hardware for laser ultrasonic sources and detectors are significantly more costly per element. In consequence, laser ultrasound arrays with multiple lasers for generation and detection is not a viable option. Laser Induced Phased Arrays (LIPAs) overcome this challenge by scanning a single generation and a single detection laser over the desired array aperture, independently of each other, in order to capture the signal from each generation and detection element combination. This data acquisition method is called the Full Matrix Capture. Images are formed in post-processing by synthetically focusing on each pixel of the image, using a delay-and-sum algorithm called the Total Focusing Method. LIPAs require long acquisition time, due to the mechanical scanning of lasers, and the inability to perform parallel data acquisition. These characteristics of LIPAs, coupled with the fact that two dimensional (2D) arrays require significantly higher number of array elements have been limiting their application for three dimensional 3D imaging towards remote volumetric evaluation of defects.

In this Thesis, 2D laser induced phased arrays are explored for 3D imaging. Sparse array designs, that can perform imaging without producing high amplitude grating lobes are investigated towards reducing the number of LIPA elements without introducing imaging artefacts. For this purpose, two approaches are implemented: aperiodic designs and designs with decoupled generation and detection layouts. By utilising these sparse array designs, the imaging efficiency of LIPAs is increased, leading to faster acquisition.

A novel adaptive data acquisition method is proposed that is able to adjust array parameters, towards optimising the array designs for the need of inspection. This method utilises a selective array building strategy that maximises generation and detection efficiency. The ultrasonic image quality achieved by this method is compared to that of the Full Matrix Capture with respect to signal-to-noise ratio and defect characterisation ability. It is shown that images of comparable signal-to-noise ratio or characterisation ability are achieved with a 10 times faster data acquisition time, utilising the adaptive acquisition method.

Finally an infrastructure is developed to synthesise the first 2D Laser Induced Phased Array. This system is utilised to remotely inspect a Wire Arc Additively Manufacture component in 3D. Image combination is performed to provide high quality 3D images of the interior of the test component. High accuracy in defect sizing and defect locating abilities is demonstrated. Furthermore, the improvements in array design and data acquisition method are adapted to 2D LIPAs in order to increase the data throughput and reduce the subsequent acquisition time, towards improving the industrial adaptability of 2D LIPAs.

Contents

Abstract	ii
List of Figures	vi
List of Tables	xi
Preface/Acknowledgements	xiv
List of Symbols	xv
Abbreviations	xvi
1 Introduction	1
1.1 General Introduction	1
1.2 Ultrasonic Imaging using Laser Ultrasonics	5
1.3 Motivation	9
1.4 Thesis Outline	10
1.5 List of Publications	12
1.5.1 Publication Arising from this Thesis	12
1.5.2 Additional Publication by the Author	13
2 Experimental Framework	14
2.1 Experimental Setup	14
2.2 Laser Beam Scanning	19
2.3 Experimental Samples	22

3	Laser Induced Phased Arrays - Data Acquisition and Processing	25
3.1	Laser Ultrasonics	25
3.2	Data Acquisition and Processing	28
3.2.1	Adoption of Phase Information for Laser Ultrasonic Imaging	31
3.3	Frequency Content of Laser Ultrasonic Data	36
3.4	Ultrasonic Array Sensitivity	40
3.5	Summary	41
4	Sparse Laser Induced Phased Arrays for Grating Lobe Suppression	43
4.1	Ultrasonic Pressure Field Modelling	44
4.2	Two-way Radiation Pattern Optimisation	50
4.3	Aperiodic Sparse Array Design	55
4.4	Evaluation of Sparse Laser Induced Phased Arrays	56
4.5	Summary	60
5	Adaptive Data Acquisition	63
5.1	Selective Matrix Capture Concept	65
5.2	SMC stage 1: Defect Detection	67
5.2.1	Continuous Data Acquisition	67
5.2.2	Iterative Array Construction	68
5.2.3	Statistical Defect Detection	70
5.3	SMC stage 2: Defect Resolving Stage	73
5.3.1	Sensitivity Threshold Method	75
5.3.2	Sensitivity-Based Element Distribution	78
5.4	Experimental Validation of Adaptive Acquisition	80
5.5	Summary	90
6	Volumetric Imaging for 2D Laser Induced Phased Arrays	94
6.1	Adapting to the Third Dimension	97
6.1.1	Data Acquisition and Processing	97
6.1.2	Visualisation of Volumetric TFM Images	99
6.1.3	Sensitivity Maps	101

Contents

6.1.4	Ultrasonic Beam Forming in 3D	102
6.2	2D Phased Array Designs	104
6.2.1	Matrix Layout	105
6.2.2	Binned Random Array Layout	105
6.2.3	Two-way Radiation Pattern Optimisation - Vernier Array Layout	106
6.3	Adaptive Data Acquisition for Volumetric Imaging	107
6.4	Experimental Results for Remote Volumetric Imaging	110
6.4.1	Volumetric Image Combinarion on an Additively Manufactured Component	110
6.4.2	Evaluation of Array Designs	114
6.4.3	Comparison of the Conventional and Adaptive Acquisition . . .	121
6.5	Summary	122
7	Conclusions	124
7.1	Review of Thesis	124
7.2	Recommendation for Future Work	130
	Bibliography	133

List of Figures

2.1	Diagram of experimental setup	15
2.2	Photos of samples showing scan surface roughness and corresponding ultrasonic images.	16
2.3	Imaging setup and their respective source shapes for cross-section and volumetric imaging	18
2.4	User Interface for experimental setup control	19
2.5	User Interface for controlling array parameters and performing LIPA scans	20
2.6	Diagram of calibration process for the scanning galvo-mirror	22
2.7	Photos of experimental test samples used in this Thesis	23
3.1	Laser ultrasound generation mechanism in the thermoelastic and ablative regime	25
3.2	Ultrasonic directivity patterns for laser generated shear and longitudinal waves in the thermoelastic regime	27
3.3	Ultrasonic detection sensitivity pattern of an out-of-plane detector for shear and longitudinal wave modes	28
3.4	Diagram demonstrating ultrasonic phased array beam forming, for steering and focusing	29
3.5	Example Laser Induced Phased Array image	31
3.6	Phase diagram demonstration of the Vector Coherence Factor in various scenarios	34
3.7	Grating lobe suppression by VCF weighting of a sparse LIPA	35
3.8	SNR improvement by VCF weighting for a dense LIPA	36

List of Figures

3.9	Temporal profile and the spectrum of the laser beam	37
3.10	Diagram demonstrating the effects of ultrasonic pulse width on axial resolution	38
3.11	Ultrasonic images showcasing the effects of ultrasonic frequency and bandwidth on resolution and SNR	39
3.12	Ultrasonic sensitivity maps for LIPAs utilising direct and mode converted wave modes	41
4.1	Simulated ultrasonic pressure field produced by an array utilising omnidirectional sources	45
4.2	Simulated ultrasonic pressure fields produced by arrays utilising laser ultrasonic generation and detection patterns	47
4.3	Simulated ultrasonic pressure field produced by two-way focusing of a LIPA	47
4.4	Array directivity extraction from ultrasonic pressure field	48
4.5	Array directivity of a sparse LIPA	49
4.6	Diagram showing the effects of array aperture on lateral resolution	50
4.7	Ultrasonic sensitivity maps demonstrating the effects of array apodisation	52
4.8	Two-way focused array directivities of a phased array using the same generation and detection layout vs phased array using different generation and detection layouts	53
4.9	Ratio of grating lobe to main lobe ratio as a function of generation to detection array pitch ratio	54
4.10	Two-way focused array directivities of a phased array using the same generation and detection layout vs phased array using a layout with half the pitch for generation as detection	55
4.11	Diagram of random array design process utilising the binned approach	56
4.12	Array directivities results of the three sparse arrays: Same Tx & Rx array, Random array and Two-way optimised array	58
4.13	Experimental ultrasonic images produced by the three sparse arrays: Same Tx & Rx array, Random array and Two-way optimised array	60

List of Figures

5.1	Diagram showing the generation and detection efficiency of potential array elements relative to a specific point of the test sample	66
5.2	Sensitivity matrix for each generation and detection element combination, relative to a specific point in the test sample	67
5.3	Comparison of two partial acquisition strategies	69
5.4	Array sensitivity comparison of varying number of array elements	70
5.5	Pixel intensity distribution of an ultrasonic image with and without a defect	72
5.6	Pixel intensity distribution of an ultrasonic image with and without SAW artefacts	73
5.7	Methodology of surface projected generation directivity calculation	74
5.8	Surface projected directivity and detection sensitivity patterns	75
5.9	Threshold method for optimised adaptive generation array configuration	76
5.10	Threshold method for optimised adaptive detection array configuration	77
5.11	Diagram of aperture width for varying inspection angles	78
5.12	Method of converting a function to element density, utilising the integral method	79
5.13	Sensitivity based element distribution calculated based on the surface projected directivity and detection sensitivity patterns	80
5.14	Photo and diagram of test sample utilised for experimental demonstration of the adaptive acquisition	81
5.15	Experimental results of adaptive acquisition stage 1, showing three iterations	82
5.16	Pixel intensity distribution of the ultrasonic images produced in SMC stage 1	82
5.17	Experimental results of adaptive acquisition stage 2, utilising both optimisation methods, compared to conventional acquisition method	84
5.18	Close-ups of the defect on the ultrasonic images presented in the adaptive acquisition stage 2 results	85

List of Figures

5.19	Experimental results of adaptive acquisition stage 1, when using the restricted aperture, showing three iterations	87
5.20	Pixel intensity distribution of the ultrasonic images produced in SMC stage 1, when using the restricted aperture	88
5.21	Experimental results of adaptive acquisition stage 2, when using the restricted aperture, utilising both optimisation methods, compared to conventional acquisition method	89
5.22	Close-ups of the defect on the ultrasonic images presented in the adaptive acquisition stage 2 results, when using the restricted aperture	89
6.1	Diagram showing a 2D phased array design that is not achievable with current systems	97
6.2	Diagram of the ray-tracing methodology for 3D imaging	99
6.3	Volumetric images showing the isosurface visualisation method	100
6.4	Comparison figure of cross-section slicing and isosurface visualisation methods	101
6.5	3D ultrasonic sensitivity map	103
6.6	Diagram of 2D matrix array layout	105
6.7	Diagram of binned random array layout	106
6.8	Diagram of Vernier array layout	107
6.9	Surface projected ultrasonic directivity and detection sensitivity for volumetric imaging	109
6.10	Surface projected directivity and detection sensitivity for direct and mode converted wave modes	110
6.11	Methodology of 2D array optimisation as a part of adaptive acquisition	111
6.12	Experimental results of stitched 3D ultrasonic images of a WAAM sample	113
6.13	Composite image of ultrasonic image and photo of replicating compound	115
6.14	Diagrams of 2D phased arrays synthesised for experimental study	116
6.15	Array directivities of 2D phased arrays used in the experimental study	117
6.16	Experimental results for 2D arrays: Matrix, Random, Vernier and SMC arrays	119

List of Figures

6.17 Experimental results of 2D random and SMC arries at two frequency ranges	120
--	-----

List of Tables

2.1	Table of test sample parameters and characteristics of the corresponding defects.	22
4.1	Array parameters and calculated grating lobe to main lobe ratios of the three sparse 1D arrays: Same Tx & Rx array, Random array and Two-way optimised array	59
4.2	SNR and peak artefact levels of three sparse 1D arrays: Same Tx & Rx array, Random array and Two-way optimised array	61
5.1	Parameters and the respective imaging performance of the arrays requiring: FMC acquisition (FMC), sub-sampled FMC acquisition (Sub-FMC), SMC acquisition utilising the threshold method (SMC) and SMC acquisition utilising the Sensitivity-based Element Distribution (SMC-SED)	86
5.2	Array parameters and the respective imaging performance, of the FMC acquisition (FMC), sub-sampled FMC acquisition (Sub-FMC), SMC utilising the threshold method (SMC) and SMC utilising the Sensitivity-based Element Distribution (SMC-SED), utilising the limited scan region.	90
6.1	True and experimentally measured defect parameters and array parameters for WAAM sample	114
6.2	Array parameters for Matrix, Random, Vernier and SMC arrays	115
6.3	Calculated main lobe to grating lobe ratio of Matrix, Random Vernier and SMC arrays	118

List of Tables

6.4	Experimental SNR and peak artefact amplitude measurements for Matrix, Random, Vernier and SMC arrays	119
-----	--	-----

Preface/Acknowledgements

First and foremost I would like to say thanks to my supervisors Theodosia Stratoudaki and Anthony Gachagan. Their guidance over the course of my PhD were invaluable, and without their support I could not have made it this far. I am grateful both for the technical wisdom, as well as the personal support they provided, especially through the difficult times we all experienced during the pandemic. I'm grateful for them to always be around to discuss ideas and to provide helpful feedback to help me improve.

I would like to express my gratitude to the various current and past members of CUE, who I had the fortune to meet. I truly appreciate the connections and friendship I had developed over the course of my PhD. Thank you for all the fun time spent together. The quality of my Thesis would not have been the same without learning so much from the people that make up CUE.

I would also like to thank my parents, Mónica and János for their endless support. I would like to thank my friends, especially Ági and Bence for always being up for a drink.

Finally I would like to thank Connor for encouraging me to do better, believing in me when I couldn't and listening to me, even when I talk too much.

List of Symbols

θ	Wave angle relative to surface normal
κ	Ratio of longitudinal to shear wave velocity
I	Image intensity of pixel
S	Amplitude of signal
x	Primary/secondary imaging axis
y	Primary/secondary imaging axis
z	Depth imaging axis
tx	Generation element index
rx	Detection element index
c	Acoustic wave velocity
E	Sensitivity map
B	Beam spreading coefficient
P	Acoustic pressure field
k	Wavenumber
λ	Wavelength
N	Number of array elements
p	Inter-element spacing

Abbreviations

1D One Dimensional

2D Two Dimensional

3D Three Dimensional

LIPA Laser Induced Phased Array

LU Laser Ultrasound

NDE Non-Destructive Evaluation

M Mirror (static)

SM Scanning Mirror

FWHM Full Width Half Maximum

SDH Side Drilled Hole

EDM Electron Discharge Machining

FMC Full Matrix capture

TFM Total Focusing Method

DAS Delay-and-Sum

SAFT Synthetic Aperture Focusing Technique

PCI Phase Coherent Imaging

Abbreviations

VCF Vector Coherence Factor

PCF Phase Coherence Factor

SCF Sign Coherence Factor

SAW Surface Acoustic Wave

FFT Fast Fourier Transform

PWI Plane Wave Imaging

CPWI Compounded Plane Wave Imaging

SNR Signal to Noise Ratio

ROI Region of Interest

SED Sensitivity-based Element Distribution

WAAM Wire Arc Additive Manufacturing

Chapter 1

Introduction

1.1 General Introduction

Non-Destructive Evaluation (NDE) is a collection of methods that evaluate the qualities and properties of components, without causing damage. A commonly used NDE method is ultrasonic imaging, which can be used to produce images of the interior of opaque objects. This can be utilised for a wide range of applications in fields such as aerospace [1,2], nuclear power [3], manufacturing [4], locomotive [5] industries.

Ultrasonic imaging needs in industrial applications are most commonly addressed by the use of ultrasonic phased arrays. Ultrasonic transducer phased arrays contain multiple transducer elements, each of which capable of generating and detecting ultrasound. They are able to achieve focusing and steering of the ultrasonic field by constructively and destructively interfering the ultrasonic waves produced by the individual elements. These abilities of a phased array (i.e.: steering and focusing) enable the production of significantly higher quality imaging, when compared to imaging methods that do not use steering and focusing (e.g.: B scan) [6].

A one dimensional (1D) array, contains all of its elements in a linear manner, offering cross-sectional imaging capabilities, when used from a single location. Two dimensional, cross-sectional imaging however only offers information about a single slice of the test object and not about the entire test component. Another disadvantage is that observing three dimensional (3D) features through two dimensional (2D) images

can be misleading, as information at a wide range of angles relating to the shape of the defect is missing. Knowing the shape, size and orientation of defects is critical for evaluating their risk factor of component failure, thus 3D imaging is necessary for NDE towards more accurate assessment of defects. For this reason the adoption of volumetric evaluation for ultrasonic imaging has been rapidly gaining popularity over previous decades [7–9].

A commonly used approach to achieve 3D imaging with a 1D phased array is to translate the array perpendicular to the plane of imaging [10, 11]. Depending on the imaging algorithm, this approach, however can have significant disadvantages. When the most simple approach, the C scan is utilised, where A scan signals captured over a 2D region are stacked [2], information about the location of defects are provided, however overall low imaging quality (e.g.: low SNR, low resolution, etc.) is achieved [12]. Alternatively, when focusing is applied during the mechanical scanning of the 1D array [11], the focusing itself is limited to the plane of imaging, thus defects are considerably distorted in the direction of scanning, as demonstrated by McKee [13].

In order to characterise defects volumetrically, 2D arrays are required, which allow beam forming in 3D, achieving volumetric imaging [12–14]. However, the wide-spread adoption of 2D arrays is currently prevented by a number of factors such as: the cost of manufacturing the large number of array elements required for commonly used inspection array apertures (e.g.: a 1D array of 30 mm aperture and 0.5 mm pitch has 61 elements, while a 2D array with $30 \times 30 \text{mm}^2$ aperture requires 3721 elements); producing hardware capable of controlling arrays with such large number of elements; the corresponding data volumes produced by of 2D arrays and the associated processing time.

Focusing using ultrasonic phased arrays can be achieved either during data acquisition by physically focusing for every section of the imaging region, or synthetically in post-processing. Physical and synthetic focusing provide the same results based on the superposition theorem [12], however the former is significantly more time consuming when focusing is performed throughout the entire image. For this reason synthetic focusing is the most commonly used method when high quality imaging is required

within the entire imaging region.

There are a wide range of ultrasonic imaging algorithms available for synthetic ultrasonic focusing, of which the Total Focusing Method (TFM) is the most commonly used, due to the high quality and versatility that this technique offers [6,15]. The TFM achieves focusing at each point of the ultrasonic image by delaying and summing the signals of a Full Matrix Capture (FMC) data set, in post-processing. The acquisition of an FMC data set consists of capturing an A scan signal for every generation and detection element combinations, thus capturing all the information that can be achieved from a single position of the phased array [6].

Utilising the TFM and FMC can provide high quality imaging, however the current conventional ultrasonic phased array imaging paradigm (i.e.: utilising transducers for generation and detection), is challenging, or sometimes impossible to utilise for certain applications. Such applications include inspection in extreme environments (e.g.: elevated temperature or radiation), in places of restricted access (e.g.: within aeroengines) or on complex components (i.e.: arbitrary shapes manufactured using additive manufacturing). Currently wheel probes are being used to address some of these inspection needs.

Ultrasonic wheel probes, utilise a dry-coupling approach, such as rubber [16]. Ultrasonic wheel probes can adjust to slightly curved surfaces due to the flexibility of the rubber, which makes the technique suitable to address inspection for processes such as Wire Arc Additive Manufacturing (WAAM) [17]. Wheel probes can also be applied for high-temperature, in-process inspection of additive manufacturing, as the piezo-electric elements are not in direct contact with the test object, and the rubber can be made of materials that are able to cope with high temperatures. In a previous work, Vithanage et al. have demonstrated wheel probe inspection up to temperatures of 350 °C [10]. Using wheel probes, complex ray tracing must be employed in order to enable imaging through the multiple layers (i.e.: delay line, rubber and the test object), including the requirement for defining the surface profile of the test object and the consequent refraction, relative to the surface tangent [18]. Furthermore, as reflection also occurs at each interface, less energy is propagated into the test object,

when compared to conventional liquid coupling. To overcome this, Zimmermann et al. proposed the use of virtual sources, firing multiple elements simultaneously, increasing the amount of energy propagated into the material [18]. More complex components are commonly inspected in immersion [19], which allows for inspection of any arbitrary shapes. However, this approach is significantly time consuming, limiting in-process inspection capabilities, it cannot be used on all types of objects (eg.: object that contain electronics) and component sizes are limited by the size of the immersion tank.

The limitations of inspecting complex components described above are posed by the need for physical contact and couplant between transducers and the test components. There are various alternative means for ultrasound generation and detection that are non-contact, however many of these are not suitable to address the limitations in question. An example is the capacitive transducers [20], which needs to be in very close proximity to the sample, not addressing the need for hostile environments. Another example is the electromagnetic acoustic transducer (EMAT), which has a big footprint, limiting its ability to work in a phased array configuration, with sufficient number of array elements [21]. Currently EMAT phased arrays are limited to low element counts in the range of 8-12 elements [22, 23], which is not sufficient for high quality ultrasonic imaging [12].

From the non-contact ultrasonic transduction methods, only one technique can address all the previously mentioned challenges, which is laser ultrasound (LU). In laser ultrasonics, ultrasound is generated and detected by the use of lasers [24]. It is non-contact and couplant-free technique, that can be applied from considerable ranges, which has been demonstrated for up to 40 meters [25], making it a truly remote ultrasonic inspection technique. Laser ultrasound enables inspection through a pane of glass, which can be useful for inspection of radioactive components contained in a chamber with a window [26], or inspecting of components in a furnace [27]. Optical beams can be focused and coupled through optic fibres [28–30], and the technique has an overall small footprint, with the potential to offer NDE capabilities in hard to access spaces, such as the interior of aeroengines. Finally, laser beams can conform to any surface shapes, thus LU can be utilised on components with complex shapes [31, 32].

Laser ultrasonic imaging has the potential to address critical NDE challenges, as demonstrated in this section. The aim of this Thesis is to develop volumetric laser induced phased array imaging in order to provide 3D defect characterisation methods, as well as the ability to inspect the entire interior of test objects with respect to the depth and spatial dimensions of internal structures. In addition, the aim of this study is to develop techniques towards improving data acquisition speed of LIPAs, to increase the adaptability of the technique towards industrial use.

1.2 Ultrasonic Imaging using Laser Ultrasonics

As stated in the previous section, a couplant-free, remote transduction method that has a small footprint and can be used on components with complex shapes is required to address various current NDE challenges. Also volumetric imaging is necessary to achieve more accurate defect characterisation. Laser ultrasonic volumetric imaging can address these requirements.

Laser ultrasonics cannot utilise the same approach for imaging as transducer-based ultrasonics for imaging, which is the approach of having multiple array elements and electronically scanning them to acquire phasing of the ultrasonic waves. For lasers this would be significantly more hardware demanding as different lasers are used for generation and detection. The current cost of suitable laser systems makes a hardware approach of laser ultrasound phased arrays significantly more costly than transducers per array element. While laser ultrasound arrays have been reported in the literature [33, 34], with a maximum of 16 elements [33], this is not comparable to the 32, 64 and 128 elements which are commonly used in conventional, transducer-based phased arrays. Furthermore the arrays were only achieved for generation, utilising a single detection point (i.e.: no parallel data acquisition).

Synthetic arrays have been proposed for laser ultrasonic imaging as a means to overcome the hardware limitations of LU [35]. A synthetic array is produced by scanning a single generation and single detection laser over the surface of the sample, forming the images in post-processing. This technique was initially used for two dimensional, cross sectional ultrasonic imaging. B-scan imaging was performed by stacking multiple

laser ultrasound acquired A scan signals without focusing [36, 37] and later utilising the Synthetic Aperture Focusing Technique (SAFT) [35, 38, 39], using the same acquisition method (i.e.: coincidental generation and detection points). The SAFT method performed focusing in post-processing, using a delay-and-sum algorithm on a dataset acquired in the same manner as B scan, with the generation and detection lasers scanned at the same time. As focusing is performed over the entire imaging region, this technique achieves significant improvements over B scan imaging in terms of Signal to Noise Ratio (SNR) and imaging resolution [40]. However, a significant disadvantage of the SAFT method as it was presented by Blouin et al. [35] and Levesque et al. [41, 42] is that, a laser beam with a significantly high power was utilised leading to ablation of the test objects. This was needed in order to overcome the low generation efficiency and detection sensitivity associated with laser ultrasonics [41, 42]. This characteristics of the technique however means that the technique is not truly non-destructive (i.e.: not an NDE method) and cannot be used in a range of applications where damage cannot be afforded even at the micro-scale level of laser ablation.

C-scan imaging has been the most prevailing method to provide 3D imaging using laser ultrasonics [43–45]. This method is similar to the B-scan imaging method, such that individual A scans are stacked to produce an ultrasonic image, however in this case acquisition is performed by a 2D array, producing a 3D image. C-scan imaging can provide depth information of internal features, however as it does not utilise focusing, overall low SNR and resolution is achieved. Furthermore, this technique is only suitable for detecting the closest feature to the inspection surface axially, thus, in the case that two features are offset in the z axis (depth), only the feature closest to the surface would be detected, whereas any other features would be shadowed. C scan imaging provides the same quality imaging as the B scan method, as they utilise the same acquisition and image forming strategies. B scan imaging has been shown to provide limited quality imaging, especially when it is compared to the modern paradigms of TFM imaging [12], thereby C scan imaging is also not sufficient for high quality 3D imaging.

There have been very limited instances in the literature where synthetic laser ultrasound arrays have been demonstrated for 3D imaging for NDE, outside the basic C-scan

imaging. These very few instances have been achieved by scanning the lasers in two dimensions and synthetically focusing the acquired signals in 3D to create 3D SAFT images [41]. Two medical implementations have also been reported in the literature, one using a static detection point [46], and another using the conventional approach of coincidental generation and detection points [47]. The SAFT method utilises the acquisition method of the C-scan imaging, however additional post-processing is carried out to synthetically focus on every pixel of the image. To the author's knowledge, two demonstrations of laser ultrasonic 3D SAFT imaging for NDE have been reported in the literature, by Levesque et al. [41] and very recently by Ni et al. [48]. In [41] the data acquisition is done at the ablation regime, hence the same associated problems of damage mentioned earlier in this section are prevailing. In [48], the authors state that imaging is performed in the low power, non-destructive regime [48]. However in this case, in order to achieve generation of waves with sufficient amplitude, a line source was used and imaging was performed by producing multiple cross-section slices and stacking them. Thus imaging is performed using SAFT in 2D, and 3D images are produced by stacking the 2D SAFT images, leaving one of the dimensions under-resolved. McKee [13] has demonstrated that this approach of 3D imaging (i.e.: stacking slices) causes considerable distortions in the dimension of stacking (i.e.: the unresolved dimension) and thus it is not sufficient for 3D defect characterisation, which is one of the main goals of 3D imaging for NDE. Overall, SAFT imaging has been demonstrated to be an imaging algorithm that produces lower quality ultrasonic imaging compared to algorithms such as TFM [12]. This is because of the limited angles of inspection viewed by the ultrasound, using this algorithm.

Recently another method has been proposed for laser ultrasonic imaging, the Laser Induced Phased Array (LIPA) that significantly outperforms the previous SAFT method by employing the Full Matrix Capture for data acquisition and Total Focusing Method for image processing [49]. In laser ultrasonics, this is achieved by scanning the generation and detection lasers independently of each other, as opposed to the simultaneous scanning utilised for SAFT. This enables capturing signals for each generation and detection element combination, acquiring N^2 A scan signals, compared to the N signals

of SAFT, where N is the number of array elements.

Advantages of LIPAs, using the FMC and TFM, include the increased sensitivity afforded by the increased number of signals, and the ability to detect and characterise a wider range of defects [50], as well as the capability to apply various post-processing algorithms [50, 51]. However, a disadvantage associated with the FMC acquisition is the requirement to capture large volumes of data. A current limitation of LIPAs is the considerable acquisition time, due to the mechanical scanning of lasers to synthesise an array, and due to the single detection laser preventing parallel acquisition of signals. Previous demonstrations of the technique were in the data acquisition time range of hours, to image regions of around $\sim 30 \times 30$ mm [49, 52].

LIPAs for NDE applications that are able to produce 3D images, with all three dimensions resolved through focusing, has not been demonstrated in the literature, prior to the present study. SAFT can only be utilised either destructively or by sacrificing focusing in one of the dimensions. Furthermore it significantly limits the viewing angles and consecutively the information in the produced image. On the other hand, LIPAs utilising the FMC and TFM achieve much higher sensitivity, thus theoretically, they can achieve 3D imaging, with point sources (i.e.: not line sources) towards true 3D imaging, with all dimensions resolved, in the non-destructive, thermoelastic regime. This technique has the potential to address various NDE needs highlighted towards NDE 4.0: volumetric imaging in extreme and hazardous environments, in-process inspection, places of restricted access and couplant-free inspection of complex components. [53] In these cases a variety of defects must be detected and characterised, such as cracks, delamination, lack of fusion or pores. LIPA inspection utilising FMC and TFM is a recent development in the field of ultrasonic imaging, thus before it can address the volumetric imaging requirements for NDT-relevant cases which are detailed in this paragraph, the basic methodology for 2D LIPAs must be established. In order to realise this, idealistic defects (i.e.: cylindrical and flat-topped defects) are utilised throughout this thesis. These have the advantage of being omni-directional scatterers at the planes of ultrasonic imaging presented, which makes them excellent cases to examine some of the fundamental of ultrasonic principles of laser ultrasonic arrays, before addressing

the varying scattering profile of defect types more relevant to the field of NDT. The aspiration of this thesis is to become a starting point for a future study where the defect scattering behaviour will be examined.

1.3 Motivation

The aims of this PhD Thesis is to: 1) investigate the capabilities of LIPAs to perform 3D imaging towards addressing current NDE challenges and 2) to demonstrate the industrial potential of 2D LIPAs by increasing the data acquisition speed through advanced signal processing, data acquisition and phased array designs techniques.

Multiple factors must be considered towards volumetric imaging for LIPAs, most important of which is the data acquisition time. It was stated in the previous section that data acquisition times for 2D LIPA imaging has been demonstrated in the order of hours [49, 52]. Another factor highlighted in Section 1.1 is the fact that 3D imaging requires a significant increase in array elements, and consequently the number of signals captured. Thereby scanning a 2D LIPA for 3D imaging would lead to long acquisition times, which is not industrially viable. Hardware improvements (e.g.: higher laser detector power, faster acquisition hardware, etc.) can increase LIPA acquisition speed, however these are not sufficient to fully address the problem. Thus this study aims to address the challenge by introducing novel LIPA imaging concepts in terms of data acquisition strategy, phased array design and advanced signal processing.

In this Thesis the first aim is to investigate the phased array improvements for LIPAs towards faster acquisition without compromising imaging performance. Previously LIPAs have only been demonstrated using equidistant, periodic phased array designs, which can lead to artefacts, when spatial under-sampling occurs. Data acquisition times can be improved by developing new sparse LIPA designs, that can suppress these artefacts.

A second aim is to consider the data acquisition strategy of Full Matrix Capture. This method was designed for transducer-based phased, where parallel acquisition is possible, and the array design is set. In comparison LIPAs are reconfigurable and can adapt to the inspection needs. Thus the question is, whether the acquisition strategy

designed for transducers is the most suitable for LIPAs and whether adaptive acquisition strategy can improve the data-throughput of LIPAs.

An infrastructure is necessary in order to synthesise 2D LIPAs and realise remote, 3D imaging. This infrastructure can demonstrate the 3D imaging capabilities of LIPAs. Finally, the demonstration of improved acquisition times and imaging performance, will progress 2D LIPAs towards industrial applications.

1.4 Thesis Outline

Chapter 2 describes the experimental setup constructed during this Thesis, including both the hardware and software elements. In this chapter the experimental test samples used in concurrent chapters are shown.

The structure of the rest of the Thesis is split into two main sections: one section, consisting of Chapters 3, 4 and 5, presents developments to 1D Laser Induced Phased Arrays, demonstrated on cross-sectional imaging; the other section consists of Chapter 6, where these advancements are utilised to 2D LIPAs, towards realising a remote volumetric imaging system. The first section's improvements are targeted towards reducing the required LIPA scan time by means of: a) improved data processing (Chapter 3); improved phased array design (Chapter 4); and development of a fast, adaptive data acquisition technique (Chapter 5).

In Chapter 3 the concept of a Laser Induced Phased Array is introduced and explained in detail. The mechanisms of ultrasound generation by lasers is introduced. Phased Array imaging is then explained, and is adapted to laser ultrasonics. This is then advanced by proposing the use of phase information during post-processing. The ultrasonic frequency produced by laser ultrasonics, and its effects on ultrasonic imaging is investigated. Furthermore, ultrasonic array sensitivities are calculated to demonstrate ultrasonic blind spots.

Sparse designs for LIPAs are considered, compared and experimentally explored in Chapter 4, with the aim of achieving phased array layouts with comparable grating lobe levels to that of a conventional array layout with more array elements, thus achieving faster acquisition without introducing imaging artefacts, while using fewer

Chapter 1. Introduction

array elements than a dense array. An analytical model based on Huygens' principle is constructed in order to evaluate the proposed array designs. Finally, the improvement in grating lobe suppression of the optimised sparse array designs is validated experimentally and compared to a conventional equidistant array layout.

Chapter 5 presents a novel, highly efficient, adaptive data acquisition strategy. This technique consists of two stages: an initial, rapid defect detection stage and a second stage with a focused scan, optimised to the location of the defect to achieve high quality imaging. The data acquisition during the first stage follows an iterative scanning process that builds multiple periodic sparse arrays until a defect or the lack thereof can be decisively found. During the second stage, an array with the ideal sensitivity can be constructed for the location of a defect, without synthesising redundant array elements, by possessing the information about the location of the defect provided from the first stage. Data acquisition is significantly improved and data volume is significantly reduced because signals from array elements that do not contribute information to the final image are not scanned. This is a key process towards enabling 3D LIPA imaging for real-life applications.

The methods presented in the previous chapters are applied and adapted for 3D imaging in Chapter 6. This includes data acquisition and image processing, sensitivity map calculation and array modelling. Phased array designs are explored for volumetric imaging, based on the concepts presented in Chapter 4. Furthermore, the optimised array concept presented in the second stage of the adaptive acquisition is developed for 3D imaging. Finally, the interior of a large additively manufactured steel component is imaged through the use of image combination and the above detailed techniques.

The work presented in this Thesis is summarised and concluded in Chapter 7 where the potential for future work and developments is discussed.

1.5 List of Publications

1.5.1 Publication Arising from this Thesis

- P. Lukacs, T. Stratoudaki, P. Wilcox, M. Clark, and A. Gachagan, “Optimisation of data acquisition and processing for laser induced ultrasonic phased arrays,” in Proceedings of Meetings on Acoustics ICU, vol. 38, p. 030015, Acoustical Society of America, 2019.
- D. Pieris, T. Stratoudaki, Y. Javadi, P. Lukacs, S. Catchpole-Smith, P. D. Wilcox, A. Clare, and M. Clark, “Laser induced phased arrays (lipa) to detect nested features in additively manufactured components,” *Materials & Design*, vol. 187, p. 108412, 2020.
- P. Lukacs, G. Davis, T. Stratoudaki, S. Williams, C. N. MacLeod, and A. Gachagan, “Remote ultrasonic imaging of a wire arc additive manufactured Ti-6Al-4V component using laser induced phased array,” in 2021 IEEE International Instrumentation and Measurement Technology Conference (I2MTC), pp. 1–6, IEEE, 2021.
- P. Lukacs, T. Stratoudaki, G. Davis, and A. Gachagan, “Adaptive data acquisition for fast ultrasonic imaging using laser induced phased arrays,” in Quantitative Nondestructive Evaluation, vol. 85529, p. V001T18A003, American Society of Mechanical Engineers, 2021.
- P. Lukacs, G. Davis, T. Stratoudaki, Y. Javadi, G. Pierce, and A. Gachagan, “Remote, volumetric ultrasonic imaging of defects using two-dimensional laser induced phased arrays,” in Quantitative Nondestructive Evaluation, vol. 85529, p. V001T18A001, American Society of Mechanical Engineers, 2021.
- P. Lukacs, G. Davis, D. Pieris, A. Gachagan, T. Stratoudaki, ”Grating Lobe Suppression Through Novel, Sparse Laser Induced Phased Array Design”, in International Ultrasonics Symposium, Manuscript submitted for publication.

Chapter 1. Introduction

- P. Lukacs, G. Davis, A. Gachagan, T. Stratoudaki, "Online evolution of a phased array by means of an adaptive data acquisition method", to be submitted to Scientific Reports.

1.5.2 Additional Publication by the Author

- E. Mohseni, C. Macleod, Y. Javadi, R. K. Vithanage, Z. Qiu, D. Lines, E. Foster, P. Lukacs, M. Vasilev, R. Zimmermann, et al., "A model-based study of transmit-receive longitudinal arrays for inspection of subsurface defects," *Journal of Non-destructive Evaluation, Diagnostics and Prognostics of Engineering Systems*, vol. 3, no. 3, p. 031102, 2020.
- E. Mohseni, Y. Javadi, N. E. Sweeney, D. Lines, C. N. MacLeod, R. K. Vithanage, Z. Qiu, M. Vasilev, C. Mineo, P. Lukacs, et al., "Model-assisted ultrasonic calibration using intentionally embedded defects for in-process weld inspection," *Materials & Design*, vol. 198, p. 109330, 2021.

Chapter 2

Experimental Framework

In this Thesis multiple experiments and experimental results are presented. The general experimental setup used is the same in all experiments with a few variations. The aim of this chapter is to describe this experimental setup, and its differences when used for the data acquisition of 1D and 2D LIPA . This will serve as a guide which can be referred to in the following chapters.

2.1 Experimental Setup

A generalised version of the experimental setup used in this work can be seen in Fig. 2.1. In this setup two lasers were utilised, one for generation and one for detection of ultrasonic waves. The generating laser was an Nd:YAG, Q switched laser (Elforlight, FQ1064) with a pulse width of 8 ns at Full Width Half Maximum. The laser beam had a wavelength of 1064 nm and an average power of ~ 600 mW, measured using a powermeter. The repetition rate of this laser was 1 KHz, thus the energy per pulse was $600 \mu\text{J}$, calculated using the following equation:

$$\text{Energy per pulse} = \frac{\text{Average Power}}{\text{Repetition Rate}} \quad (2.1)$$

The laser used for the detection of ultrasound was a rough surface interferometer (Sound & Bright, Quartet), that measures the displacement caused by the ultrasonic waves where the laser illuminates the surface of the test object. An Nd:YAG continuous

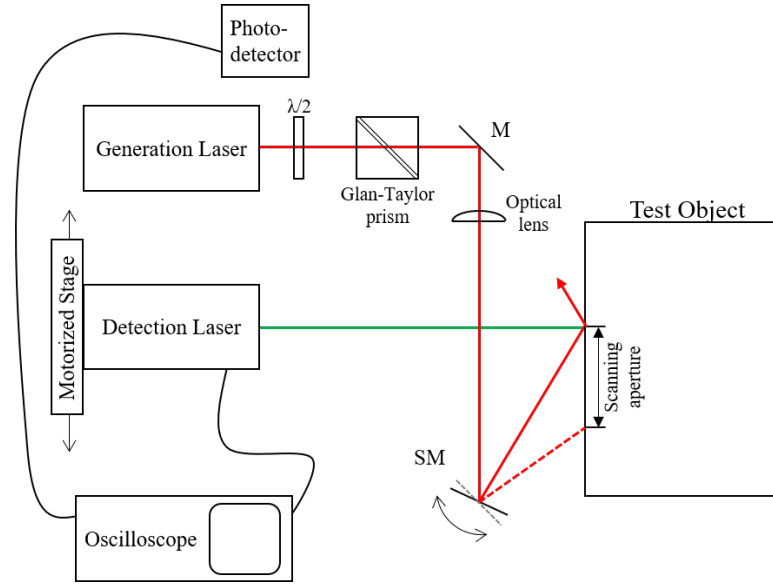


Figure 2.1: Graphical representation of experimental setup. M is a stationary mirror, SM is a galvo scanning mirror. Half-wave plate is signified by $\lambda/2$. Diagram is not to scale.

wave laser is used in this equipment, operating in its second harmonic, thus the emitted light has a wavelength of 532 nm. It has an average power of 780 mW, operates in continuous wave mode and is coupled through an optic fibre to an optical head with a 50 mm diameter light collecting lens. The interferometer had a lens, provided by the manufacturer, of 200 mm focal depth which determined its stand-off distance from the inspected sample and was mounted on two linear, motorised stages (Thorlabs, KMTS50E/M with 50 mm travel range & PI, M-511.DD1 with 100 mm travel range).

Multi-Channel Random Quadrature detection is utilised by the Quartet, thus it can operate on rough surfaces [54, 55]. By using a random quadrature demodulation, the random nature of the reflected light speckles reach the multi-channel sensor where they interfere with the reference beam, providing high sensitivity to displacement, even on rough surfaces. Figure 2.2 shows three samples with differing surface roughnesses including: (A) machined and polished surface, (B) machined surface and (C) as-deposited surface with no surface alteration. The component in Fig. 2.2 (C), was manufactured by the additive manufacturing process called Selective Laser Melting (SLM), and had a surface Roughness Average (RA) of $0.43 \mu m$ [56]. A 1D LIPA was synthesised on

Chapter 2. Experimental Framework

each sample in order to image interior defects located in each of them. Note that these results are not comparative. On the contrary, the shape and location of the defects, as well as the the material types, manufacturing processes and consequently the microstructure properties varied, leading to significant differences in imaging capabilities. However these images demonstrate that LIPAs utilising a rough surface detector such as the Quartet, can successfully be utilised from polished (Fig. 2.2 (A)) to rough (Fig. 2.2 (C), $RA = 0.43 \mu m.$) surfaces. These samples were titanium (A) and aluminium (B-C), had 1 mm (A), (B) and 0.25-0.75 mm (C) diameter cylindrical defects. Note that these figures are only utilised to demonstrate the imaging capabilities of LIPAs on varying surfaces and will not be referred to later on in this Thesis.

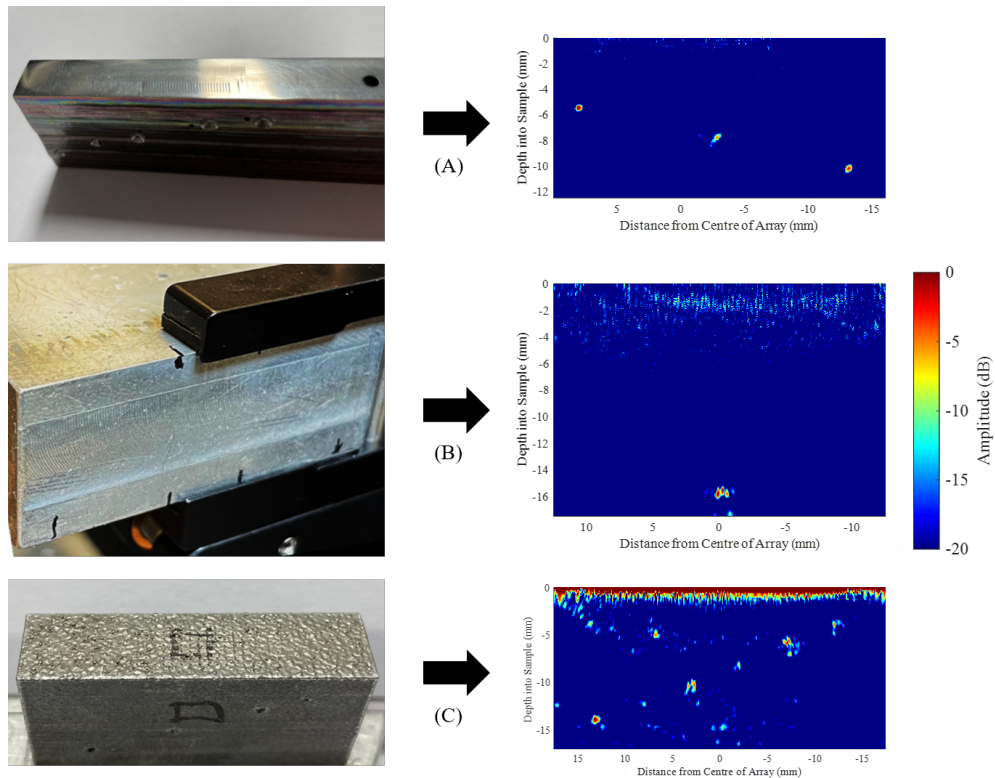


Figure 2.2: Photos of surface finish of a polished (A) a machined (B) and an as-deposited (C) samples and the corresponding ultrasonic images produced by inspecting the samples. Colour bar indicates the intensities of the ultrasonic images.

Furthermore, the detection system has a bandwidth of 1 to 66 MHz and it detects the out-of-plane component of the displacement caused by the ultrasonic waves, while

being insensitive to the in-plane component. The signals that are output by the receiver are then captured by an oscilloscope (InfiniiVision DSO5014A, Agilent Technologies), which then transfers the data to a computer.

The optics used in this setup, are shown on Fig. 2.1 and included a half-wave plate ($\lambda/2$, Edmund Optics, 43705), a Glan-Taylor prism (Edmund Optics, 89548), a stationary mirror (M, Thorlabs, BB1-E03), a focusing lens and a motorised, 2-axis galvo mirror (SM, Thorlabs, GVS302), with a maximum scan angle of $\pm 10^\circ$. The Glan-Taylor prism is a polarising beam splitter, that divides the incoming beam based on its polarisation into transmitted and reflected beams. The half-wave plate located in front of the Glan-Taylor prism rotates the polarisation of the generation beam with respect to its optical axis. Thus the ratio of the horizontal and vertical components of the polarisation is controlled by the orientation of the half-wave plate. As the Glan-Taylor prism reflects one of the components, changing the ratio consequently changes the amplitude of the transmitted beam. Thus these two components provide a mechanism to control the amount energy of the generating laser beam that is incident on the stationary mirror.

The optical lens used after the stationary mirror, before the scanning mirror, focuses the generating beam on the surface of the test object, to achieve high optical density. Two types of lenses were used in this work, a plano-convex cylindrical (Thorlabs, LJ1558RM-C) and an achromatic doublet (Thorlabs, AC254-200-AB) lenses. The cylindrical lens focuses the laser beam of diameter d into a line of length d and width of w where $d \gg w$ ($\sim 0.5 \times 4$ mm). The spherical lens focuses the incoming circular beam of diameter d into a small circular spot with diameter of c (~ 1.5 mm), where $d \gg c$. The focal depths of these lenses were respectively, 300 and 200 mm. The linear source from the cylindrical lens was used for the 2D imaging setup (1D LIPA synthesis) and the point source from the spherical lens was used for volumetric imaging (2D LIPA synthesis) as demonstrated on Fig. 2.3. The fluence of the laser was ~ 0.03 J/cm² for both cases.

The 1 kHz repetition rate of the generation laser translated to a time interval of 1 ms between each emission. Synchronisation of the data acquisition on the oscilloscope was

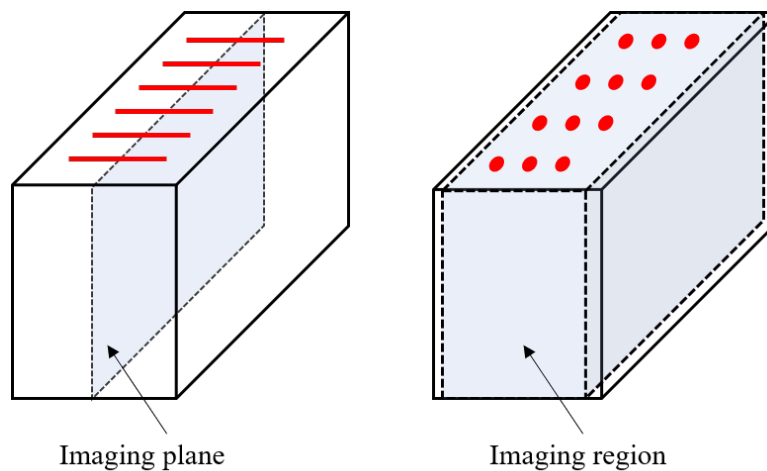


Figure 2.3: Graphical representation of source shapes and their respective imaging setups.

achieved by setting a rising edge trigger on the output of the photo-detector (Thorlabs, PDA10A2). Hence, as soon as the photo-detector senses the generating laser-pulse, it triggers the data acquisition.

The multiple instruments on the experimental setup were interfaced using the software called LabVIEW. Figure 2.4 shows the User Interface (UI) that was developed during the course of this study for setting up experiments and optical alignment for experiments presented in this Thesis. Using this UI, the 2-axis galvo mirrors and the motorised stages can be independently controlled in order to locate the desired starting position for LIPA scanning. Within this UI a section for controlling and viewing the screen of the oscilloscope is present. Using this, the generation and detection beam positions can be precisely aligned on the inspection surface by measuring the arrival time of the surface acoustic wave. Finally, a section of the code within this UI, performs calculations for calibration of the galvo mirror to enable translation of mirror rotation to linear movement of the generation beam on the scan surface. This calibration is further explain in section 2.2.

On the second panel of the UI shown in Fig. 2.5, the scanning parameters of the LIPA can be defined, and scanning can be initiated. This scanning can be performed, either in 1D or 2D and independently for the generation and detection lasers alike. The step sizes for scanning can be independently defined for generation and detection, in

Chapter 2. Experimental Framework

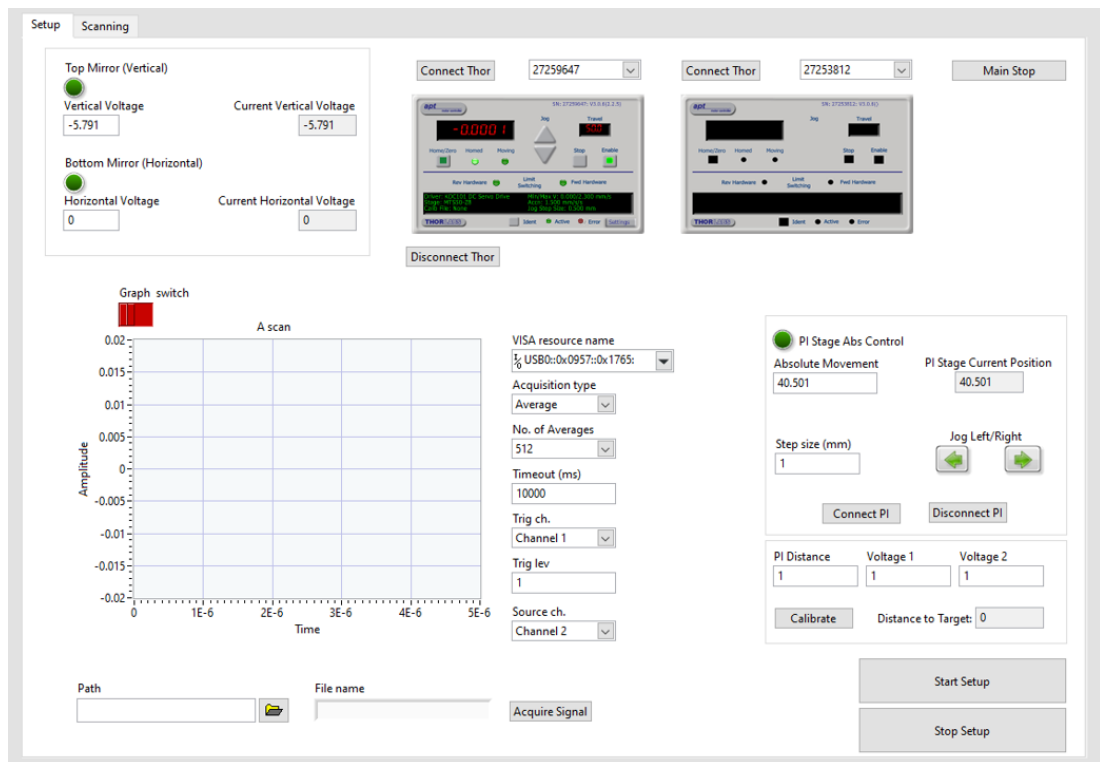


Figure 2.4: The user-interface constructed for the code that was utilised for alignment purposes for experiments.

both scanning dimensions. A section of this UI was constructed for the purposes of controlling the oscilloscope parameters for the scanning, such as the number of signal averaging, or length of time trace. Finally two indicators were installed: a graph that shows the currently captured A scan signals, and progress bars that show the progression of the scan.

2.2 Laser Beam Scanning

Scanning of the two lasers was achieved by two different mechanisms. Two motorised, linear stages (Thorlabs, KMTS50E/M with 50 mm travel range & PI, M-511.DD1 with 100 mm travel range) were used to translate the detection laser beam horizontally and vertically and a 2-axis galvo scanning mirror (Thorlabs, GVS302) comprised of two independently controlled mirrors was used to translate the generation laser beam. The galvo mirrors were optimised to reflect light at 532 and 1064 nm, had a damage

Chapter 2. Experimental Framework

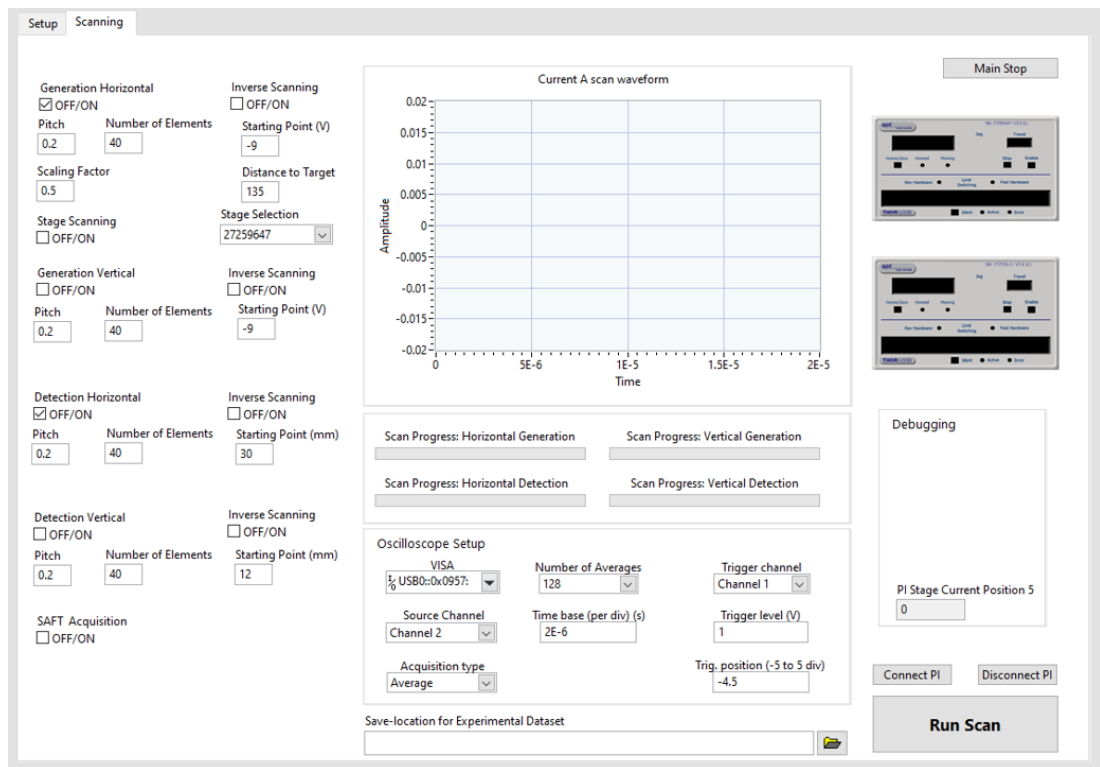


Figure 2.5: The user-interface constructed for the code that was utilised for scanning purposes for experiments

threshold of 5 J/cm^2 and mirror size of 8.5 by 14.5 mm for ones axis and 10 by 8 mm for the other. While the linear, motorised, scanning stages achieve slower scanning due to the higher inertia, they were necessary for the detection in order to maintain the laser beam's normal incidence angle relative to the inspection surface. A deviation from the normal incidence would result in some loss of the returning light, reducing SNR and this would depend on the roughness of the reflecting surface and the spread of the reflected scattered beam at the entrance of the receiving lens with respect to the lens aperture size. As the translation of the detection beam in both dimensions was achieved in a linear manner (i.e.: the movement of the stage results in an equal amount of movement of the laser beam position on the surface), the arbitrary positioning of the detection point was simplified. However, the positioning of the generation laser beam, required the need to convert spatial values to rotations of the galvo mirror.

The relationship between the rotation of the galvo mirror and the movement of the

beam is tangential. In order to find the rotation required for the galvo mirror to move the beam a certain distance the following equation was used:

$$\theta = \tan^{-1}(xd_t) \quad (2.2)$$

Where θ is the rotation of the mirror relative to its zero position, x is the desired movement of the laser beam relative to when the mirror is at its zero position, and d_t is the distance between the galvo mirror and the test object, which will be referred to as stand-off distance for the remainder of this Thesis. As the stand-off distance between the galvo mirror and the surface of the test object is unknown, a calibration process was developed and followed prior to each experiment, with the aim of experimentally measuring the stand-off distance with high precision. This was achieved by positioning the detection laser beam at two subsequent arbitrary positions on the sample, and finding precisely the angles that correspond to the same positions for the generation laser beam. As the relative distance can be measured by the change in position of the linear stage where the detection laser head was mounted on, the following equation was used to calculate the stand-off distance:

$$d_t = \frac{\Delta x}{\tan(\theta_1 + \Delta\theta) - \tan(\theta_1)} \quad (2.3)$$

Where Δx is the distance between the two positions, θ_1 and θ_2 are the angles between the stand-off distance and the 2 sequential positions of the laser beam and $\Delta\theta$ is the relative angle difference between angles θ_1 and θ_2 . Figure 2.6. visually demonstrates this procedure.

The scanning utilised throughout this Thesis performs N^2 signal measurements, where N is the number of array elements. Each signal is captured for a unique combination of generation and detection laser positions, thus this results in the movement of one laser N times (slow axis) while the other laser N^2 times (fast axis). In this work to achieve high scanning speeds, the generation laser was selected to be the fast axis, which is moved by the galvo mirror. This was done to achieve faster scanning, as the detection laser as the fast axis, moved by the linear stages would lead to limited

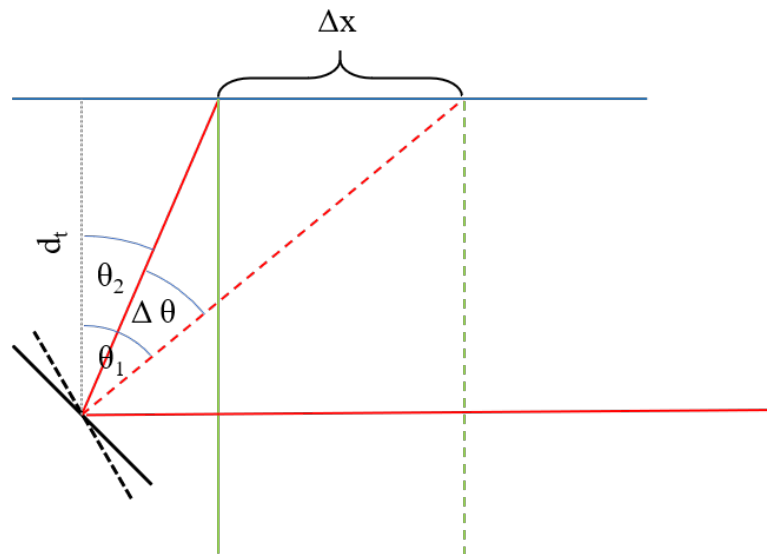


Figure 2.6: Graphical representation of the mirror calibration process. Red and green continuous lines show the generating and detecting beam paths respectively, for the first position. Red and green dashed lines show the beams for the second position. Gray dotted line shows the distance between galvo mirror and the inspection surface (stand-off distance, d_t).

scanning speed.

2.3 Experimental Samples

	Defect types	Defect diam.	Dimensions	In Chapter
Sample A	Through holes (E)	1 mm	$58 \times 58 \times 25$ mm	3
Sample B	Blind holes (E)	1 mm	$90 \times 49 \times 20$ mm	4,5,6
Sample C	Blind holes (D)	2 & 3 mm	$106 \times 61 \times 10$ mm	6

Table 2.1: Table of defect types (E - EDM, D - Drilled), defect diameter, test sample dimensions, and corresponding chapter number where the sample is used.

In this work three test samples were utilised for imaging which are shown on Fig 2.7. These samples were made of aluminium (Sample A and B) and steel (Sample C) and had acoustic shear velocities of ~ 3350 m/s and ~ 3250 m/s respectively. Each sample

Chapter 2. Experimental Framework

had artificially introduced defects. Sample A, contained 9 cylindrical through-holes in a radial layout relative to the the centre of the sample. Each defect was 1 mm in diameter. Sample B had three types of defects: 1 mm diameter through holes, 1×3 mm through slots and 1 mm diameter blind holes at varying depths. Only one of the blind holes were imaged in this work, which is marked by a yellow arrow in Fig. 2.7 while the rest of the defects were outside the imaging region. All imaged defects on Sample A and B were produced using electron discharge machining (EDM). The defects on Sample C were created by drilling. The way defects are created affects the surface finish of the defect, for example EDM produces smooth defect-walls, while drilling generally results in rougher walls relative to the acoustic wavelengths that are commonly used in NDT (i.e.: 1-10 MHz). This is important when the interaction of the ultrasonic waves is considered at the defect interface. The quality of roughness impacts the way defects scatter ultrasound, with smooth interfaces leading to more specular reflections, while rougher defects causing the reflections to be more diffused [57, 58].

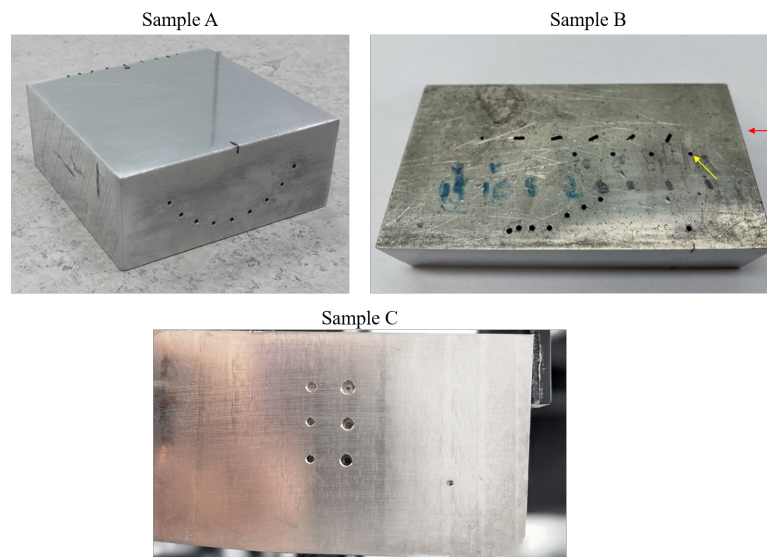


Figure 2.7: Aluminium (Samples A & B) and steel (Sample C) test samples used for experimental inspection.

The scan surface of the different samples varied. Sample A had a polished scan surface. Sample B, when imaged from the side indicated by the red arrow (Fig. 2.7 for cross-section imaging had a rough machined side, while when it's imaged from the

Chapter 2. Experimental Framework

opposite side from the one that is visible in Fig. 2.7 (i.e.: imaging the tip of the blind-hole shown by the yellow arrow) it had a smooth, polished surface. Finally Sample C had a rough, machined scan surface. Table 2.1 summarises the properties of the samples and their corresponding defects.

Chapter 3

Laser Induced Phased Arrays - Data Acquisition and Processing

3.1 Laser Ultrasonics

In laser ultrasonics, acoustic waves are generated by illuminating the surface of an object with a pulsed laser beam. Depending on the energy density of the laser light, there are two LU generation mechanisms: in the thermoelastic and in the ablative regime as shown on Fig. 3.1.

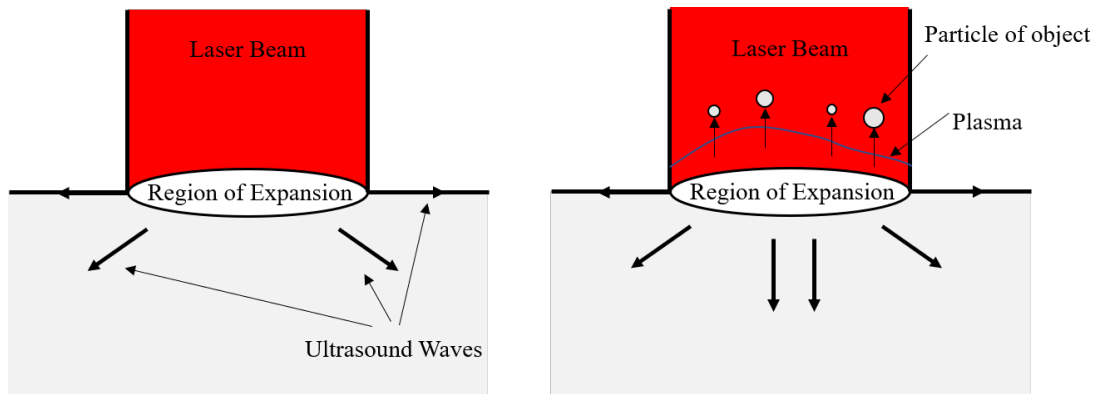


Figure 3.1: Laser Ultrasound generation mechanism in the thermoelastic regime (left) and the ablative regime (right)

When the laser light illuminates the test sample, a portion of the optical beam is absorbed by the test sample, while the rest is reflected. In the case of metallic

objects this absorption happens in the electromagnetic skin depth, which extends at the order of nanometers from the surface. For example, for irradiation using the 1064 nm wavelength of a Nd:YAG laser, the absorption depth would be 5 nm for the case of aluminium [24]. In the thermoelastic regime, some of the energy absorbed by the sample is then converted into heat which in turn causes the region that absorbed the energy to expand. As the material tries to expand, stresses and strains are generated, producing elastic waves also known as acoustic waves.

The other generation mechanism, the ablative regime occurs when the energy density of the light on the surface exceeds the damage threshold of the sample. The high-power beam results in the production of plasma on the surface, causing the material to evaporate. During this process, the particles from the test object are ejected away from the surface. This produces a recoil force with an opposite polarity, directed towards the bulk of the sample.

These mechanisms produce all wave modes: surface acoustic waves (SAW), as well as bulk longitudinal and shear waves. In general, waves produced in the thermoelastic regime exhibit lower amplitudes [36], however as this generation mechanism is truly non-destructive, only this regime is considered and utilised for experiments, described in this Thesis.

In the thermoelastic regime, ultrasound is not generated uniformly at all angles relative to the normal to the surface. The directivity of the induced waves can be defined by the following equation for shear and longitudinal wave, respectively [59]:

$$G_L(\theta) = \frac{\sin \theta \sin 2\theta (\kappa^2 - \sin^2 \theta)^{1/2}}{2 \sin \theta \sin 2\theta (\kappa^2 - \sin^2 \theta)^{1/2} + (\kappa^2 - \sin^2 \theta)^2} \quad (3.1)$$

$$G_T(\theta) = \frac{\sin 2\theta \cos 2\theta}{\cos 2\theta^2 + 2 \sin \theta \sin 2\theta (\kappa^2 - \sin^2 \theta)^{1/2}} \quad (3.2)$$

Where θ is the angle of ultrasound wave propagation relative to the surface normal, within the sample and κ is the ratio of longitudinal to shear acoustic velocity of the test object.

As shown in Eq. 3.1 and 3.2, the ultrasound directivity of laser generated shear and

longitudinal waves are defined solely by the acoustic velocity properties of the material. For example, the directivities of laser induced ultrasound in aluminium can be seen in Fig. 3.2, obtained by substituting the corresponding velocities in Eq. 3.1 and 3.2. The values used were 3200 and 6300 m/s for shear and longitudinal waves respectively, which are typical values for aluminium. These figures indicate that ultrasound is generated at the highest intensities at $\sim 30^\circ$ and $\sim 60^\circ$ relative to the surface normal, for shear and longitudinal waves, respectively.

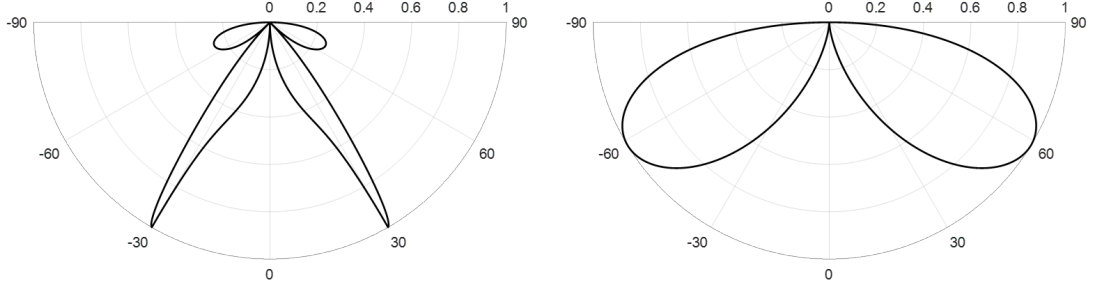


Figure 3.2: Ultrasonic directivity patterns of laser generated ultrasonic transverse (left) and longitudinal (right) waves in aluminium.

In the thermoelastic regime, laser generated shear waves are generally stronger than longitudinal waves for metals [60]. For the case of aluminium, this difference is of an order of magnitude [60]. It is due to this reason, that in the work presented in this Thesis shear waves are utilised for imaging, while the longitudinal waves are ignored.

Acoustic wave detection is also performed by optical means, in laser ultrasonics. The detection hardware used in the present study is an interferometric detector, which is sensitive to the out-of-plane component of the detected ultrasound waves [54]. It is due to this reason that the sensitivity of the system is not uniform at all ultrasonic incidence angles of the received ultrasound waves. The sensitivity pattern of an out-of-plane detector can be calculated using the following equation [61]:

$$D_L(\theta) = \frac{\cos \theta (\kappa^2 - 2 \sin^2 \theta)}{F_0(\sin \theta)} \quad (3.3)$$

$$D_T(\theta) = \frac{\sin 2\theta (\kappa^2 \sin^2 \theta - 1)^{1/2}}{F_0(\kappa \sin \theta)} \quad (3.4)$$

Where,

$$F_0(\xi) = (2\xi^2 - \kappa^2)^2 - 4\xi^2(\xi^2 - 1)^{1/2}(\xi^2 - \kappa^2)^{1/2} \quad (3.5)$$

Similarly to the case of the directivity, the ultrasonic sensitivity is governed by the acoustic velocities, as per Eq. 3.3 and 3.4. Applying the same velocity values used to produce the directivity pattern on Fig. 3.2 (i.e.: 3200 and 6300 m/s for shear and longitudinal waves, respectively) to Eq. 3.3 and 3.4, the sensitivity patterns for an out-of-plane component detector on an aluminium sample are shown on Fig. 3.3.

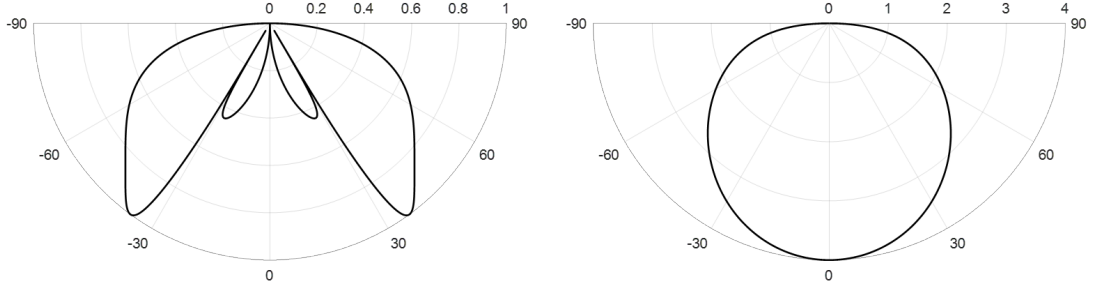


Figure 3.3: Ultrasonic sensitivity patterns of an out-of-plane component detector for transverse (left) and longitudinal (right) waves in aluminium.

3.2 Data Acquisition and Processing

In order to produce high quality ultrasonic images, phased arrays utilise ultrasonic beam steering and focusing through constructive and destructive interference. This is achieved by applying delays to each array element, carefully calculated in order to produce the desired ultrasonic field. These delays applied to the array are called the delay law and a visual representation of their use for beam steering and focusing can be seen in Fig 3.4.

For data acquisition, LIPAs use the Full Matrix Capture technique, where the generation and detection elements are scanned over each element position, independently of each other. Thus an ultrasonic signal is captured for each generation and detection element combination [6]. The FMC method ensures that all the possible information that is available from a single position of the ultrasonic phased array is obtained.

Beam steering and focusing is achieved synthetically, in post-processing, on a Full

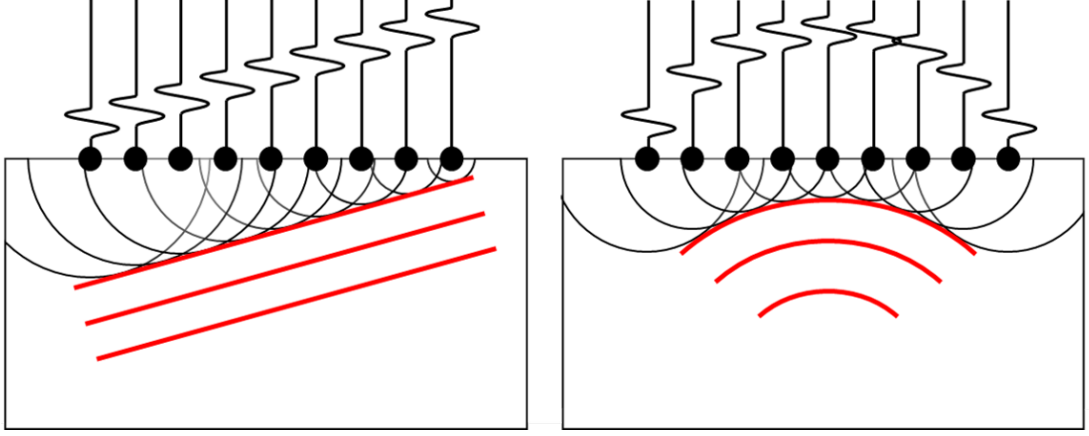


Figure 3.4: Ultrasonic beam steering (A) and focusing (B), when applying the appropriate time delays to individual array elements

Matrix data-set by using a Delay-and-Sum (DAS) algorithm. Of these DAS algorithms, the most commonly used is the Total Focusing Method, where a user defined grid is established over the imaging region, and the ultrasonic signals are delayed and summed based on the superposition theorem to achieve synthetic focusing at each pixel of the image. TFM achieves significantly higher imaging quality compared to other imaging technique such as unfocused B scan or SAFT, due to the high number of signals used for focusing, the wide range of angles probed in the sample by ultrasound and because focusing is performed at every single point of the image, both in transmission as well as reception [6]. The TFM algorithm can be described by the following equation:

$$I(x, z) = \left| \sum_{tx=1}^n \sum_{rx=1}^n S_{tx,rx} \left(\frac{d_{tx} + d_{rx}}{c_{mode}} \right) \right| \quad (3.6)$$

Where d_{tx} and d_{rx} are the distances between the pixel at (x,z) and the transmitter and receiver element, respectively. c_{mode} is the acoustic velocity of the imaging mode for the given material, $S_{tx,rx}$ is the A scan signal at tx and rx element combination and I is the pixel intensity at (x,z) co-ordinates of the imaged area. The distances d_{tx} and d_{rx} can be calculated using the following equations for the case of cross-sectional imaging:

$$d_{tx} = \sqrt{(x_{tx} - x)^2 + z^2} \quad (3.7)$$

$$d_{rx} = \sqrt{(x_{rx} - x)^2 + z^2} \quad (3.8)$$

Utilising FMC as the data acquisition method is simple for transducer-based phased arrays, as the array can be electronically scanned and simultaneous reception from many array elements is possible. The cost of generation and detection lasers are however significantly higher than that of a single element of a transducer-based phased array, with current laser technology. Thus, constructing a system containing 32, 64 or 128 lasers, representative of a common phased array, is not viable, due to hardware constraints, especially when considering that two lasers are required per element, one for generation and one for detection. LIPAs overcome this challenge by synthetically constructing the array [49]. A single generation and a single detection laser are scanned over the surface of the test object. Independent scanning of the two lasers enables capturing all the generating and detection element combinations. Based on the superposition theorem, acquiring signals with a synthetic array is equal to that of a physical array [12].

Element positions are defined by the scanning mechanism, hence array parameters such as number of elements, inter-element spacing, layout and aperture can be reconfigured between and during experiments. Furthermore the decoupled generation and detection also enables constructing phased arrays with any arbitrary generation and detection array layout, including partially or completely overlapping elements, of which the former is not possible with conventional phased array systems.

In Fig. 3.5 an example of a cross-sectional TFM image is shown, produced on Sample A (See Fig. 2.7), imaging 1 mm diameter holes. The LIPA synthesised consisted of 161 elements, with 0.155 mm inter-element spacing, in order to fully populate a 25 mm aperture with an $\lambda/2$ spacing at 10 MHz. Band-pass filtering was used at 5MHz centre frequency, with a bandwidth of 130%, using the filtering process explained in further detail in Section 3.3. A signal averaging of 16 was used for each A scan signal captured. In total, 25921 A scan signals were captured (161×161), leading to a total acquisition time of ~ 30 minutes.

The image itself was normalised and converted to dB values to simplify interpretation of the data, which was achieved using Eq. 3.9.

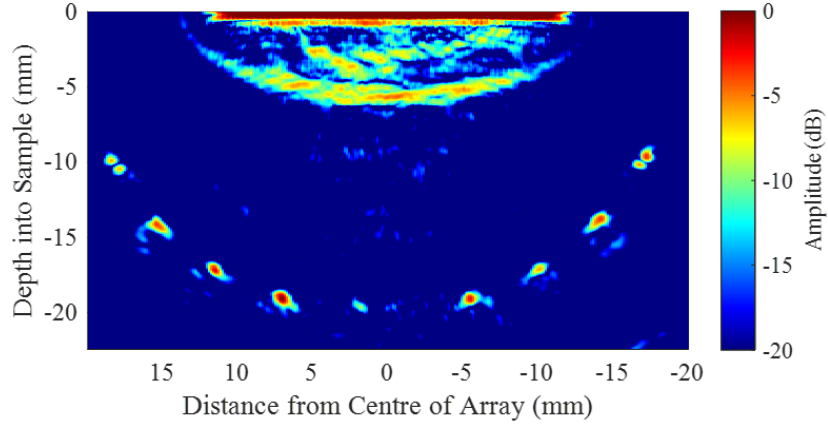


Figure 3.5: An ultrasonic image produced using a 1D, 161 element Laser Induced Phased Array, with 0.155 mm inter-element spacing. Ultrasonic A scan signals were processed at 5 MHz centre frequency, using 130% bandwidth.

$$I_{dB} = 20 \log_{10} \left(\frac{I_{abs}}{I_{max}} \right) \quad (3.9)$$

A large amplitude region can be seen near the top of the TFM image in Fig. 3.5, called the SAW cross-talk region. This is caused by the wave travelling along the surface of the sample, from the generation points to the detection points. As this is an undesirable imaging artefact, for the purposes of normalisation, this region was excluded manually, ensuring that normalisation is performed relative to the highest amplitude defect pixel and not the SAW artefact.

3.2.1 Adoption of Phase Information for Laser Ultrasonic Imaging

In standard ultrasonic beam forming techniques, including DAS algorithms, multiple ultrasonic waves are combined either physically or in post-processing to achieve constructive or destructive interference. As the received ultrasonic waves are spatially sampled by a physical or synthetic array, under-sampling can cause the generation of undesirable grating lobes. As per the Nyquist sampling theorem, the inter-element spacing, must be less than half the acoustic wavelength to avoid grating lobes [62]. However, this can often be challenging as reducing the pitch by increasing the number of array elements or reducing overall aperture, will lead to higher system complexity or compromised lateral resolution, respectively.

Phase Coherence Imaging (PCI) has been proposed in the literature in order to address the challenge of undesired grating lobes [63]. In PCI the phase information of acquired A scan signals is measured and combined in order to produce a weighting factor for each individual pixel of the image, that reduce intensities where low coherence of phase is observed through the time-shifted A scan signal. The use of PCI reduces imaging artefacts and increases overall image quality [63].

The concept of phase coherence imaging can be described as measuring and comparing the phases of each ultrasonic signal at the focal point. If a reflector is present at the focal point, the phases will be similar, leading to high phase coherence. In contrast, if no feature is present at the focal point, reflections are not produced, thus the time-shifted signals will not contain any structural information (i.e.: only noise is present). Due to the stochastic nature of noise, the phase of the individual data points from each A scan signal will be randomly distributed, leading to low phase coherence. A weighting factor based on this coherence is computed, which is then applied to the ultrasonic imaging processed by conventional imaging techniques such as SAFT or TFM.

In the study presented here, the potential use of PCI for LIPAs is explored. As the contribution of random noise and noise from scattering is reduced, the generally low SNR of LU is significantly increased, allowing the reduction of array elements without compromising imaging quality. Furthermore, due to the suppressed grating lobes, the array pitch can be increased beyond half the acoustic wavelength without producing artefacts, thus element count of the array can be further reduced. Finally, PCI is presented as a method to reduce the effects of unwanted wave modes that are generated by laser ultrasound, such as the case of the high amplitude surface acoustic waves.

In previous studies, researchers have presented various implementations of PCI [64]. Each variation calculates the weighting factor based on the phases through a different methodology and thus PCI is performed with different efficiency in each case. Of these, the Vector Coherence Factor (VCF) has been shown to outperformed previous implementations, such as the Phase Coherence Factor (PCF) or the Sign Coherence Factor (SCF), due to its ability to overcome the discontinuity at $\pm\pi$ [64]. The circular

coherence factor is another factor that has also previously been proposed. It similarly overcomes the discontinuity, however with a higher computational complexity without providing any benefits in performance over VCF. For this reason, the VCF weighting factor is used throughout this Thesis whenever phase coherence is utilised, and it is applied by taking the product of the TFM image and the weighting factor.

The Vector Coherence Factor defines the phases of the signal at each data point as a complex number that can be represented by vectors on the complex plane, unlike previous PCI methods, where a singular value was used. By representing the phases as vectors, similar phases will constructively sum, while summing randomly distributed phases will tend towards zero. As vectors do not exhibit phase-wrapping at $\pm\pi$, the effects of discontinuity is eliminated. The factor itself can be calculated by the following equation [64]:

$$VCF(x, z) = \sqrt{\left(\sum_{tx=1}^n \sum_{rx=1}^n \frac{Re(S_{tx,rx}(x, z))}{|S_{tx,rx}(x, z)|}\right)^2 + \left(\sum_{tx=1}^n \sum_{rx=1}^n \frac{Im(S_{tx,rx}(x, z))}{|S_{tx,rx}(x, z)|}\right)^2} \quad (3.10)$$

Where $S_{tx,rx}$ is a complex number composed of the real part and the imaginary part of the A scan signals. The imaginary part is calculated by applying the Hilbert transform on the real component of the signals.

As shown on Fig. 3.6 (A), when focusing onto a reflector, high coherence of the phases is observed. In contrast on Fig. 3.6 (B) and (C), when focusing is preformed where no features are present, low coherence is observed, due to the random phases of noise. Thus, the weighting factor will tend to 1 in Fig. 3.6 (A) and 0 in (B) and (C).

The results of applying the VCF weighting factor to a LIPA image can be seen on Fig. 3.7. The same test object, Sample A, was used, as shown in Fig. 3.5, however in this case the array was sub-sampled to 54 array elements, down from the image with 161 elements shown in Fig. 3.5. Without the VCF weighting factor, a considerable section of the image is masked by the high amplitude artefacts produced by the grating lobes.

Considering the sub-sampling of the LIPA, the inter-element spacing increased to

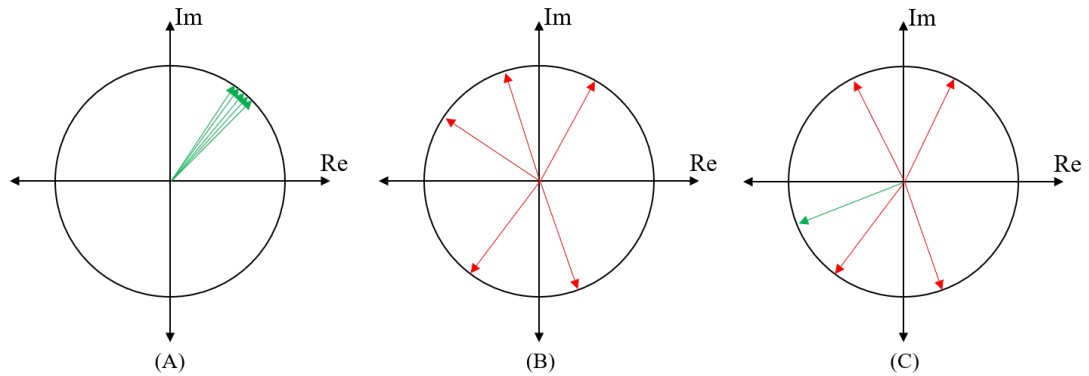


Figure 3.6: Normalised phase diagrams of data points on A scan signals, when focusing where a point reflector is present (A), where no feature is present (B) and where a grating lobe is present (C). Green arrows represent the phase from signals reflected from a defect, whether the signal is coming from the focal point or from a grating lobe, while red arrows represent the phase of noise.

0.465 mm compared to the previous 0.155 mm in Fig. 3.5, while utilising the same aperture width. The wavelength of the acoustic waves is 0.64 mm at the 5 MHz centre frequency of the digital filter used in post-processing for both these TFM images. It is reminded here that in Fig. 3.5 the pitch of 0.155 mm satisfies the Nyquist sampling theorem ($0.155 \text{ mm} < \lambda/2$), while the inter-element spacing in Fig. 3.7 does not satisfy it ($0.465 \text{ mm} > \lambda/2$). It is due to this spatial under-sampling that grating lobes are now produced, which in turn create imaging artefacts as seen at the right side of Fig. 3.7 (A). These high amplitude artefacts appearing on the image are mainly due to the interaction of the grating lobes with the high amplitude surface acoustic waves that are reflected from the edges of the sample and they compromise the imaging capabilities of the TFM, as can be seen in Fig. 3.7 (A). On this image, the effects of grating lobes (i.e.: artefacts) appear more concentrated on the right side of the image. This was achieved by miss-aligning the optical focal point of the generation laser, such that the laser beam is more in focus when approaching the right edge of the array, producing higher intensity SAWs compared to the amplitude of the SAWs produced at the left side of array. This was done in order to concentrate the effects of grating lobes to one side of the image.

In comparison when observing Fig. 3.7 (B) where VCF was used in the post-

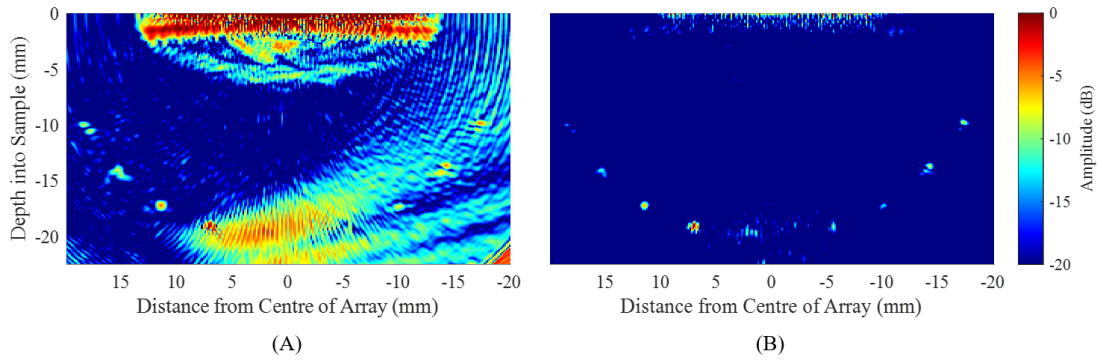


Figure 3.7: Ultrasonic images produced by a sparse array using the Total Focusing Method, without applying VCF (A) and with VCF (B). LIPA of 54 array elements and 0.465 mm inter-element spacing.

processing, the artefacts produced by the grating lobes are suppressed, uncovering regions previously concealed by them. Furthermore an additional benefit of the technique is the reduction of other undesirable effects, such as noise due to ultrasonic scattering, the inherent noise of the laser detection system, as well as signals from undesirable wave modes, such as the high amplitude SAW region near the scan surface. This improvement is demonstrated on Fig. 3.8, showing the images produced by a dense LIPA without (A) and with (B) the Vector Coherence Factor weighting. In this case a dense array is used, as opposed to the sparse array that was presented in the previous figure (Fig. 3.7), thus grating lobes are not produced, leading to an image without grating lobe artefacts. However noise occurs on the ultrasonic image, caused by factors such as ultrasonic scattering from the micro-structure or the inherent noise of the ultrasonic detector. Observing the two images shown in Fig. 3.8, it can be seen that when VCF is applied as a weighting factor, it can reduce the effects of this noise and increase overall SNR.

It is important to note that while, VCF offers improvement regarding imaging quality and grating lobe suppression, it performs best with point-like defects which reflect ultrasound uniformly in all directions. Applying VCF requires the detection of ultrasonic echoes at all elements and failure to achieve this results in the deterioration of the performance of phase coherent imaging [65]. Porosities and other similar defects act as point scatterers and work well with VCF. However many other defect types,

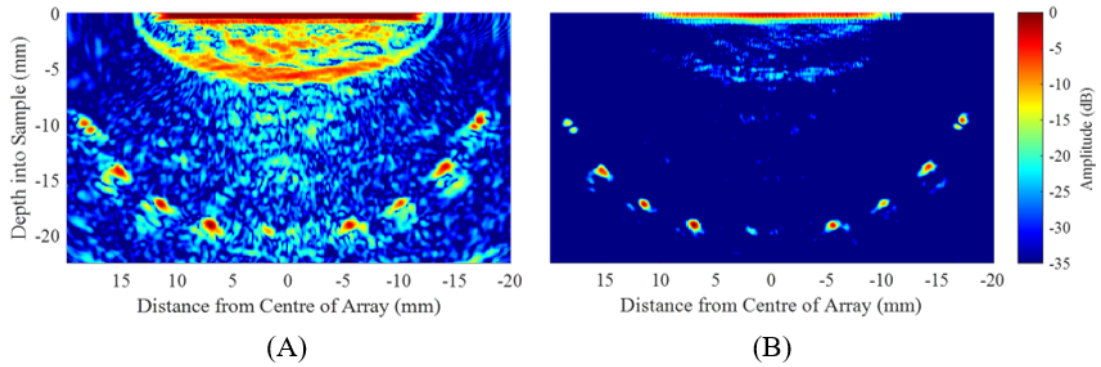


Figure 3.8: Ultrasonic images produced by a dense array (161 elements, 0.155 mm inter-element spacing) using Total Focusing Method, without applying VCF (A) and with VCF (B).

such as cracks, act as specular reflectors and do not scatter ultrasound uniformly at all angles [50]. Hence phase coherence does not perform equally for all types of defects.

3.3 Frequency Content of Laser Ultrasonic Data

In the case of materials examined in this Thesis, the laser energy is absorbed in a layer much thinner than the ultrasonic wavelength (a few nanometers in aluminium). As a result, the bandwidth of the generated wave depends on the temporal characteristics of the laser pulse is broadband [24]. As described in Chapter 2, the laser in the experimental setup has a pulse width of 8 ns Full Width Half Maximum. The temporal profile of the beam is shown on Fig. 3.9, along with the frequency content of this beam, obtained through Fast Fourier Transform (FFT). Due to the short pulse-width, a wide-band frequency signal is generated by the laser with frequency content ranging from DC up to above 100 MHz, with a Full Width Half Maximum (FWHM) of ~ 27 MHz. This range is limited by the detection system, which has a bandwidth of 1-66 MHz.

Depending on the application, not every component of this spectrum contains useful information. In the case of NDE, acoustic attenuation becomes so severe above a certain frequency, due to scattering, that ultrasonic waves rapidly disappear within the sample. Conversely, low frequencies also have disadvantages, as ultrasonic waves will

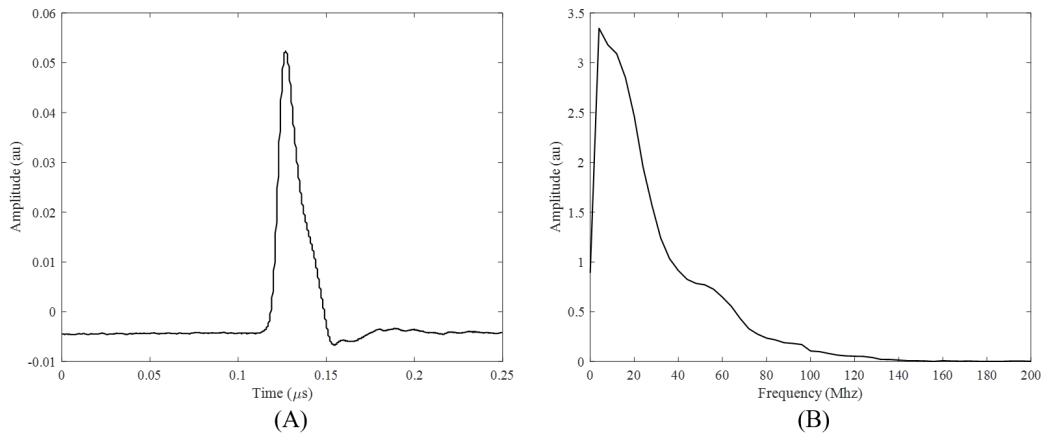


Figure 3.9: Temporal profile (A) and the spectrum (B) of the generating laser beam

not interact with features smaller than half the acoustic wavelength, due to the diffraction limit. Hence, high frequency components only containing noise, and low frequency components that cannot interact with small features, contain very little structural information and are undesirable.

In order to discard undesirable frequency components, filtering can be performed on the acquired signals. Digital filtering can be applied to signals in post-processing, with the additional benefit of being able to choose various frequency ranges and filter shapes, without altering the original raw data. In this work, band-pass filtering was realised using a Gaussian shape, defined by two characteristics: the centre frequency and the bandwidth. The bandwidth is described as a percentage of the centre frequency by -6 dB drop. Considering a filter centred at 5 MHz, with a 100% bandwidth (i.e.: 5MHz bandwidth at -6 dB drop) would translate to lower and upper cut-off frequencies of 2.5 and 7.5 MHz, respectively.

When performing imaging using LIPAs, the frequency content to utilise must be carefully considered. The spectrum of the ultrasound waves used has a wide range of effects on ultrasonic inspection and imaging. In addition to the attenuation and the diffraction limit, which were mentioned, another critical characteristic is ultrasonic resolution, which defines the ability to resolve two closely located features. In ultrasonic imaging the a critical objective is to achieve high resolution, allowing accurate iden-

tification of defects. In cross-sectional, ultrasonic imaging, resolution is described as lateral and axial resolution. As lateral resolution is mainly controlled by the aperture width of the array, for the remainder of this section, when resolution is mentioned, it refers to axial resolution. Lateral resolution will be further discussed in Section 4.1.

From the available wide ultrasonic frequency band, higher frequencies resolve smaller features. Furthermore, the bandwidth of the signal also has an impact on this resolution: wide bandwidth leads to higher resolution, due to the shortened pulse width in time [66]. A larger bandwidth produces shorter acoustic pulses in time, thus they achieve higher resolution when compared to a narrow-band pulse. A graphical representation of how the shorter temporal pulses achieve higher axial resolution towards resolving two defects located in close proximity is shown on Fig. 3.10.

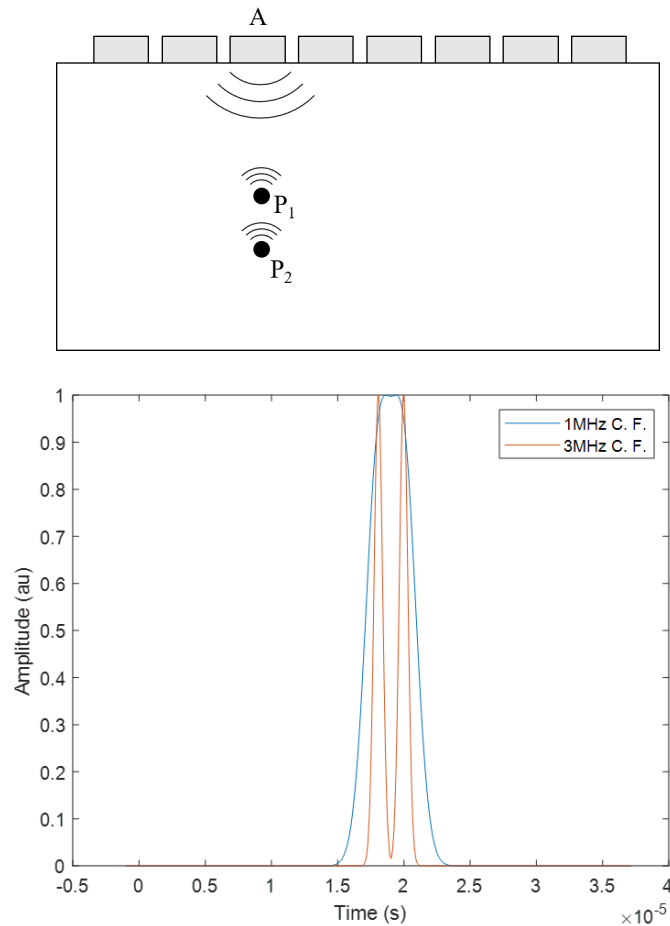


Figure 3.10: Visual demonstration of resolution as a function of centre frequency (C.F.).

As detailed in the previous paragraph, utilising high frequencies and a wide bandwidth provides increased resolution resulting in improved imaging quality, however this can lead to higher attenuation due to ultrasonic scattering. Hence, when selecting the frequency range of the digital filter, a compromise between resolution and attenuation must be made. Images shown on Fig. 3.11 demonstrate the relationship between frequency, bandwidth, ultrasonic resolution and attenuation. These images were produced by applying various digital filters on the signals used for the production of Fig. 3.5. In this case Phase Coherence Imaging was not applied.

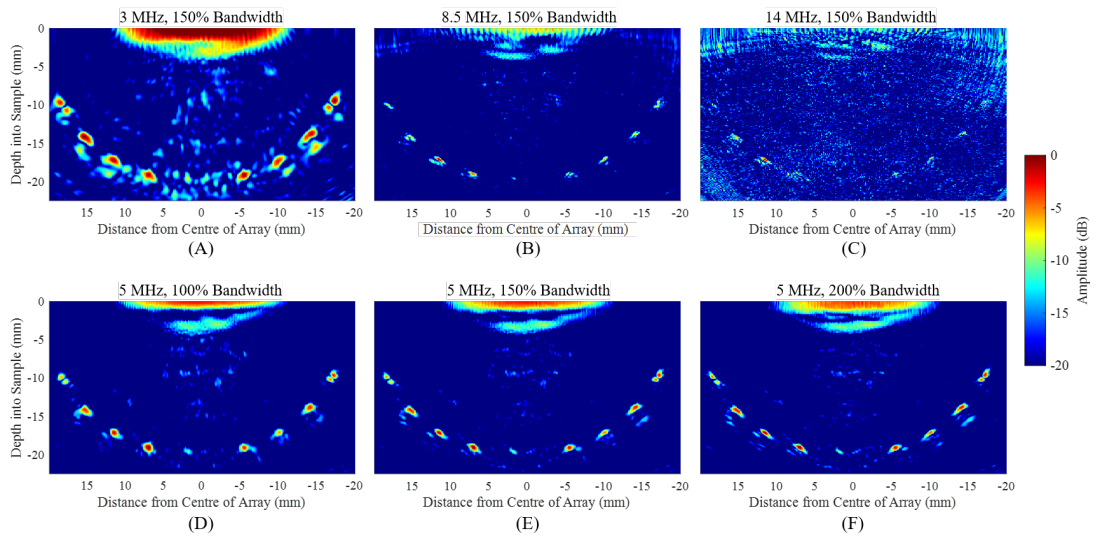


Figure 3.11: TFM images of the same LIPA data-set (161 elements and 0.155 mm inter-element spacing) demonstrating the effect of ultrasonic frequency and bandwidth to the resolution of point scatterers (1 mm side drilled holes).

In the first case shown on Fig. 3.11 (A-C), the filter bandwidth is static at 150%, and the centre frequency of the filter is varied. The results show that as frequency is increased the resolution is improved, however as the imaging frequency keeps increasing, ultrasonic attenuation dominates the signals decreasing overall SNR of the resulting images as shown on Fig. 3.11 (C). The second case, shown on Fig. 3.11 (D-F) the filter was centred at a static 5 MHz, while the filter bandwidth was varying. As the bandwidth is widening the defects are resolved smaller, due to the increased resolution.

3.4 Ultrasonic Array Sensitivity

In order to characterise defects accurately, the response of the imaging system is required to be consistent. Using an ideal imaging system, two identical defects are expected to appear identical in amplitude on the ultrasonic images. This however is not always the case. The lack of consistency can be partially explained when considering the ultrasonic directivity and sensitivity patterns, as well as beam spreading and attenuation. From this, it becomes clear that depending on the defect's location and orientation relative to the array elements, the response on the resulting image will vary. This can be defined by the ultrasonic sensitivity map, which is a metric that indicates the amplitude of the response of the imaging system to a point reflector, at any position relative to the ultrasonic phased array [67].

Ultrasonic sensitivity maps are calculated by assuming an ideal, omnidirectional point scatterer (i.e. reflecting ultrasound uniformly in all directions, at every pixel of the user-defined grid within the imaging region). The general equation for calculating sensitivity maps for laser ultrasound can be defined by the following equation [49]:

$$E(x, z) = \left| \sum_{tx=1}^n \sum_{rx=1}^n G(\theta_{tx}(x, z)) D(\theta_{rx}(x, z)) B_{tx,rx}(x, z) \right| \quad (3.11)$$

Where B is the beam spreading coefficient and is defined by the following equation:

$$B_{tx,rx}(x, z) = \sqrt{\frac{1}{(d_{tx}(x, z) d_{rx}(x, z))}} \quad (3.12)$$

And the angles between the generating element and pixel, and the detecting element and the pixel are defined as:

$$\theta_{tx} = \tan^{-1} \left(\frac{\sqrt{(x_{tx} - x)^2}}{z} \right) \quad (3.13)$$

$$\theta_{rx} = \tan^{-1} \left(\frac{\sqrt{(x_{rx} - x)^2}}{z} \right) \quad (3.14)$$

Shear and longitudinal waves exhibit different patterns both for ultrasonic genera-

tion and detection, as shown on Fig. 3.2 and 3.3, thus the sensitivity maps will vary depending on what wave mode is being considered, including mode conversion, such as shear generation and longitudinal detection and vice versa. Calculating the sensitivity maps for the different modes can be achieved by inserting either shear or longitudinal patterns for the generation and detection patterns in Eq. 3.11. Figure 3.12 shows a numerical example of sensitivity maps for a 100 element LIPA for shear, longitudinal and the two mode converted waves considering the acoustic properties of aluminium.

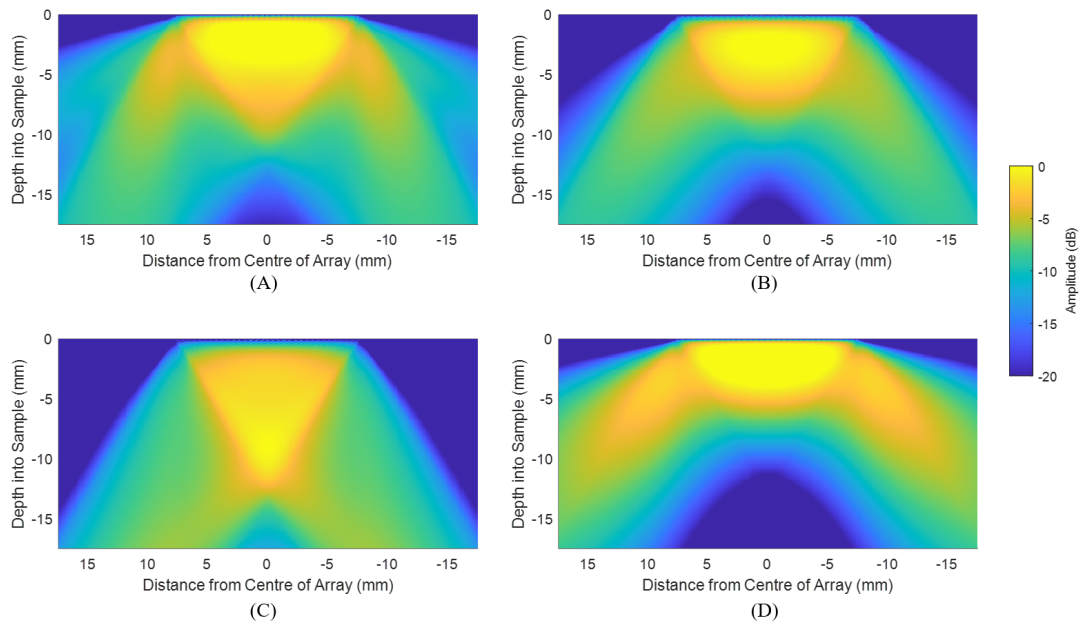


Figure 3.12: Sensitivity maps produced using shear waves (A), longitudinal waves (B), shear-longitudinal mode converted waves (C) and longitudinal-shear waves (D)

3.5 Summary

The aim of this chapter was to provide a sufficient background information on laser ultrasonics for this Thesis. Basic concepts of laser ultrasonics were explained, including the ultrasonic generation mechanisms along with the characteristics of the laser generated ultrasound waves, such as propagation directivity and detection sensitivity. The theory of phased array ultrasonics was presented, as well as the Full Matrix Capture acquisition method and the relevant post processing imaging algorithm, the Total Fo-

cusings Method. The adaption of these concepts for laser ultrasonic was then presented which is called Laser Induced Phased Arrays.

In order to improve the imaging capabilities, phase information was utilised for LIPAs for the first time, providing better SNR and suppressing grating lobes when spatial under-sampling of the aperture occurs. The results have shown, that by employing the vector coherence factor weighing, defects could be located on images produced by a sub-sampled LIPA (See Fig. 3.7), in spite of a threefold reduction in array elements, translating to a nine-fold reduction of A scan signals captured in the Full Matrix. This improvement is critical towards enabling volumetric imaging for LIPAs, as currently acquisition times are limited by the high array element count and the mechanical scanning of the lasers. As a result it is also critical for the industrial implementation of LIPAs.

The concept of wide-band ultrasonic signals and band-pass filtering for ultrasonic imaging was introduced. The relationship ship between frequency, bandwidth, attenuation and resolution was explained and a comparative study (See Fig. 3.11) was performed to validate this, using varying digital filters on experimental LIPA data.

Finally the effects of ultrasonic generation directivity and detection sensitivity for ultrasonic imaging was explained. This was quantified by calculating the array sensitivity maps, providing information regarding how sensitive the phased array is to a defect at any given location.

Chapter 4

Sparse Laser Induced Phased Arrays for Grating Lobe Suppression

Reducing acquisition times of ultrasonic phased arrays and improving imaging efficiency, while maintaining high imaging quality has been the goal of many researchers over previous decades [68–70]. The motivation behind this activity has always been to boost the application potential of phased arrays. Various techniques have been proposed in order to increase imaging efficiency and these are roughly focused around research on phased array designs and signal processing.

The Laser Induced Phased Array is a relatively new technique, that utilises the Full Matrix Capture data acquisition, capturing an A scan signal for each generation and detection element combination. It has been demonstrated to be an effective tool for inspecting additively manufactured components [52] and objects with complex shapes [31], however a limiting factor is the time-consuming data acquisition. The aim of this chapter is to reduce LIPA acquisition time towards enabling volumetric imaging and improve industrial applicability. Optimisation of the ultrasonic phased array design is explored for Laser Induced Phased Arrays for faster acquisition, exploring designs that suppress or do not induce imaging artefacts. In this study the array optimisation is achieved by taking advantage of the fact that of LIPAs can be reconfigured into any

arbitrary array layout for ultrasonic generation and detection.

Initially, an analytical model is established, based on Huygens' principle. In this work, Huygens' principle is utilised to calculate the ultrasonic field produced by a phased array in order to evaluate the performance of multiple designs by measuring the undesirable grating lobes. The improvements achieved in the analytical model are then experimentally demonstrated on metallic test objects.

Two categories of phased array designs are presented: periodic and aperiodic layouts. Each individual design methodology is described in detail, and are evaluated using the analytical model. Previously an array with a reconfigurable generation layout has been presented by Alles et al. [71], however, to the author's knowledge, in this study the first ultrasonic phased array system with independent and reconfigurable ultrasonic generation and detection layouts is presented. Furthermore this is the first study into optimising sparse array focusing for laser ultrasonic imaging as well as.

4.1 Ultrasonic Pressure Field Modelling

Evaluation of the pressure field produced by an ultrasonic phased array can be calculated utilising Huygens' principle [66, 72, 73]. Huygens' principle states that an ultrasonic wave front can be divided into various individual spherical or cylindrical sources based on the concept of superposition. Conversely, a wave produced by a phased array can be calculated as a depth varying function after applying a specific delay law. The amplitude of side-lobes and grating lobes (when spatial under-sampling occurs) can be measured by analysing the calculated pressure field away from the focal point.

The acoustic pressure field can be defined by the following generalised equation, where the time delays are expressed as phase shifts [66]:

$$P(x, z) = \sum_{el=1}^n e^{i(kd_{el}-kd_f)} \quad (4.1)$$

Where, el is the array element, d_{el} is the distance between pixel and element el , d_f provides the distance to calculate the time delay for the focal point for element el relative to the centre of the array:

$$d_f = \sqrt{(x_{el} - x_f)^2 + z_f^2} - \sqrt{x_f^2 + z_f^2} \quad (4.2)$$

and k is the wave-number calculated by the following equation:

$$k = 2\pi\lambda \quad (4.3)$$

Figure 4.1 shows an example pressure field calculated when focusing at a depth of 20 mm from the surface, without applying any beam steering (i.e.: focal point at $(x,z)=(0,20)$ mm). For this calculation, an array aperture of 25 mm, element number of 80, inter-element spacing of 0.32 mm, ultrasonic frequency of 5 MHz, and a shear acoustic velocity of 3200 m/s was assumed. The model does not provide absolute pressure field measurements as the input does not take into consideration the amplitude of the waves produced by the individual array elements. The image was normalised to its highest value as the pressure field calculation provides relative information .

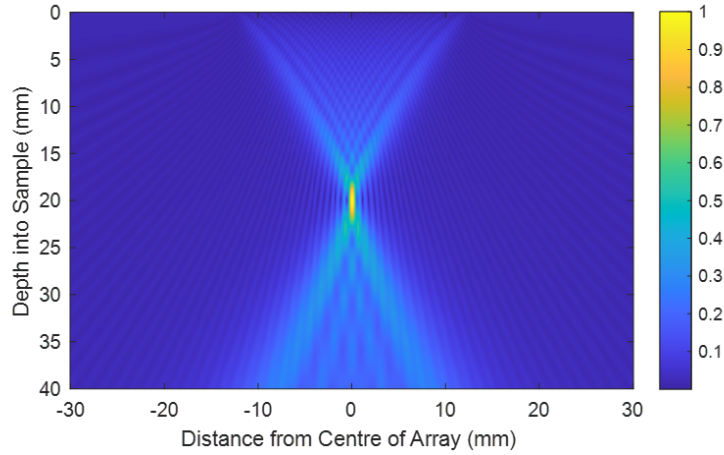


Figure 4.1: Simulated pressure field of a phased array, based on the analytical model described by Eq. 4.1. Colour scale shows normalised amplitude of the pressure field.

The general Eq. 4.1 assumes uniform directivity at all angles, however this is not representative of the physical scenario in laser ultrasonics at the thermoelastic regime. For this reason, Eq. 4.1 adapted to account for the shear directivity and sensitivity patterns defined by Eq. 3.2 and 3.4 in order to account for non-uniformity of the ultrasonic field. In addition, focusing in transmission and reception produces two

independent pressure fields because the angular patterns are different for generation and detection. Thus in the following equations the pressure field will be expressed by two separate equations, one for transmission (P_{tx}) and another for reception (P_{rx}). Another effect that influences the pressure field is the beam spreading of the wavefront, which has been defined by Eq. 3.12. If all these effects are taken into consideration then the pressure field calculation can be expressed by the following two equations:

$$P_{tx}(x, z) = G_T(\theta_{tx})B(x, z) \sum_{tx=1}^n e^{i(kd_{tx} - kd_f)} \quad (4.4)$$

$$P_{rx}(x, z) = D_T(\theta_{tx})B(x, z) \sum_{tx=1}^n e^{i(kd_{tx} - kd_f)} \quad (4.5)$$

Where θ_{tx} and θ_{tx} are the angles between array elements and pixels as defined by Eq. 3.13 and 3.14.

Figure 4.2 shows the pressure field produced when focusing is applied in transmission (A) and reception (B) to a LIPA. The array parameters and focusing was identical to values utilised to produce Fig. 4.1. As can be seen in this figure showing the laser ultrasound adapted focused pressure fields, the array cannot constructively and destructively interfere the ultrasonic waves as efficiently as when waves with uniform directivity were utilised, due to the limited angles of generation and detection. This is especially evident when observing the strong side lobes appearing around the main lobe at the focal point.

Currently, pressure fields only in transmission or reception, were considered, also called one way focusing. This is equivalent to using an imaging method such as the Plane Wave Imaging where focusing is only achieved in reception. However, the imaging method utilised in this study is the TFM which achieves focusing both in transmission and reception at the same time, leading to two-way focusing. The ultrasonic field produced by applying two-way focusing to a phased array is defined by the product of the two independent pressure fields as follows:

$$P_{total} = P_{tx} * P_{rx} \quad (4.6)$$

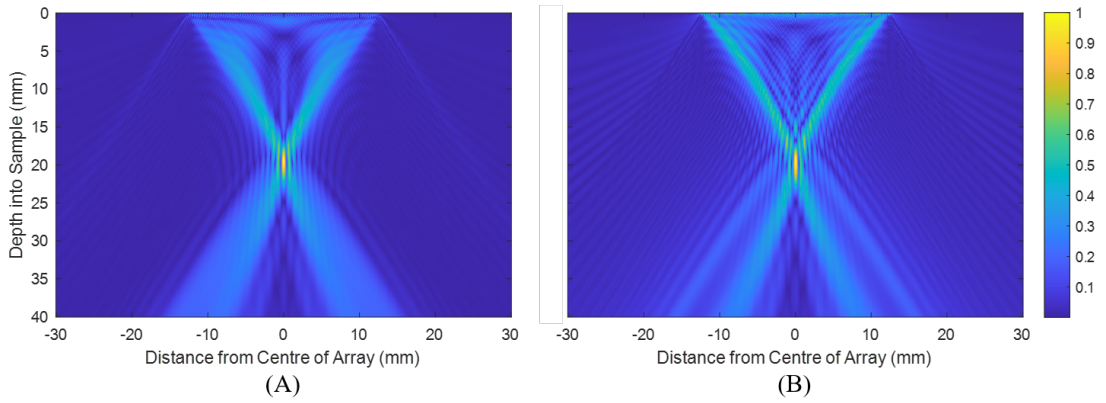


Figure 4.2: Simulated pressure field of a phased array when focusing in transmission (A) and reception (B), based on analytical model described by Eq. 4.4 and 4.5, respectively. Colour scale shows normalised amplitude of the pressure fields.

The acoustic pressure field produced in two-way focusing can be seen in Fig. 4.3 based on the pressure fields previously shown on Fig. 4.2. As can be seen in Fig. 4.3, a significant improvement in concentrating the pressure fields at the focal point is achieved by performing focusing in transmission and reception simultaneously. A reduction in amplitude away from the focal point can be observed, leading to an amplitude reduction in undesirable side-lobe levels.

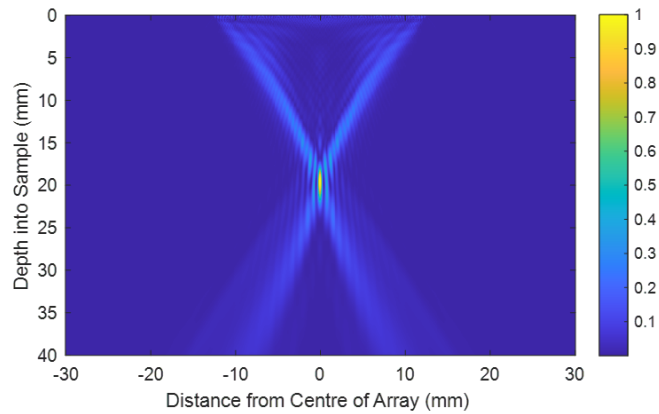


Figure 4.3: Simulated pressure field of a phased array when focusing in transmission (A) and reception (B), based on analytical model described by Eq. 4.4 and 4.5, respectively. Colour scale shows normalised amplitude of the pressure fields.

As the aim of this work is to calculate the pressure field for grating lobe level evaluation, the array directivity (i.e.: pressure field at the radius equal to the focal distance,

from the centre of the array, as shown on Fig. 4.4 (B)) provides sufficient information, eliminating the need to determine the pressure field within the entire imaging region. The array directivity is calculated by measuring the produced ultrasound along all angles relative to the surface normal at a constant radius of the focal distance, as shown by the red, dashed circle in Fig. 4.4. In Fig. 4.4 (B) the array directivity extracted, along the red, dashed circle can be seen.

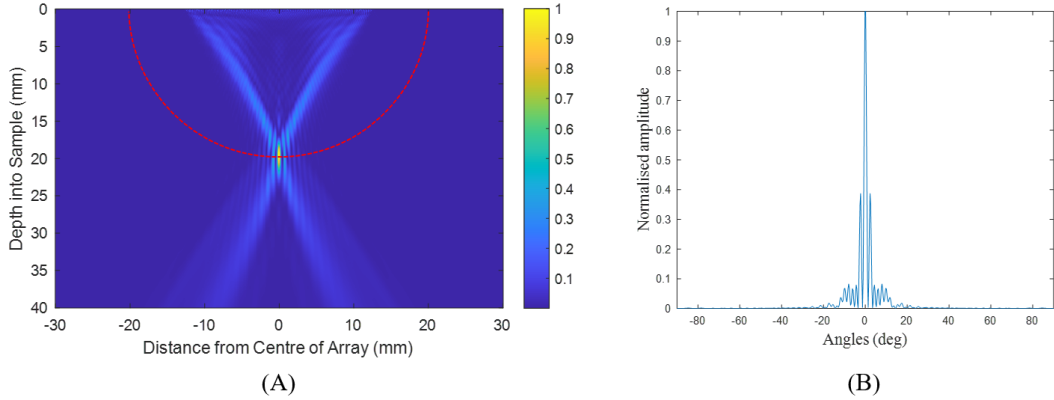


Figure 4.4: Pressure field produced by an array (80 elements, 0.32 mm inter-element spacing, at frequency of 5 MHz) using two-way focusing (A). The array directivity is highlighted along the red dashed circle. The extracted array directivity (B) as a function of angles at a constant radius of focal distance.

The array directivities is an effective tool to evaluate the array performance of the ultrasonic phased array [62, 66]. Information relating to the lateral resolution, and artefacts can be extracted through inspection of the main lobe width and side lobe and grating lobe levels. A wide range of optimisations can be performed in order to improve various array characteristics, such as reducing the width of the main lobe and suppressing side lobes. In this study the aim is to suppress the artefacts induced by grating lobes.

In this section and up until now, pressure fields have been modelled for densely populated arrays. An array is defined as dense when the inter-element spacing (p) is equal to or less than half the acoustic wavelength ($p \leq \lambda/2$), thus no spatial under-sampling occurs during focusing. When a sparse array, with a pitch larger than half the acoustic wavelength, is utilised for focusing, grating lobes are produced at undesirable

angles. Figure 4.5 shows the array directivity of a sparse array. The same values were used for this array directivity as for Fig. 4.4, however with half the number of array elements (i.e. 40 array elements, 0.64 inter-element spacing, at 5 MHz frequency). In this case, the same array aperture was used and the inter-element spacing became equal to the acoustic wavelength. As can be seen in the array directivity plotted in Fig. 4.5, undesirable grating lobes appear at around 70° . This was expected due to the array being sparse and not satisfying the Nyquist criterion.

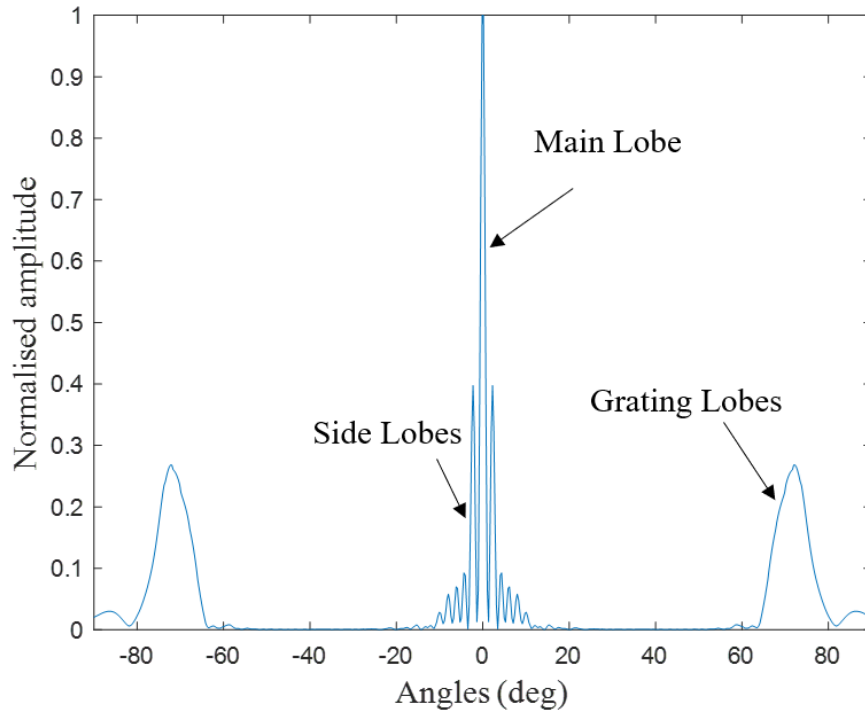


Figure 4.5: Array directivity of a sparse array (40 elements, 0.64 mm inter-element spacing, at frequency of 5 MHz) with an inter-element spacing equal to the acoustic wavelength, when focusing at). Main lobe, side lobes and grating lobes are indicated on the figure.

The above detailed sparse array can be converted into a dense array without introducing more array elements by reducing the inter-element spacing. This however leads to an overall decrease in array aperture. The aperture width is a main defining factor of lateral resolution [66] for ultrasonic imaging, as demonstrated on Fig. 4.6. Thus, decreasing the overall aperture size in order to overcome the sparsity of an array compromises the resolution. As resolution is a critical factor, this approach is not desirable.

Hence, an optimised sparse array must be explored for LIPAs to ensure that resolution is not compromised while grating lobes are suppressed.

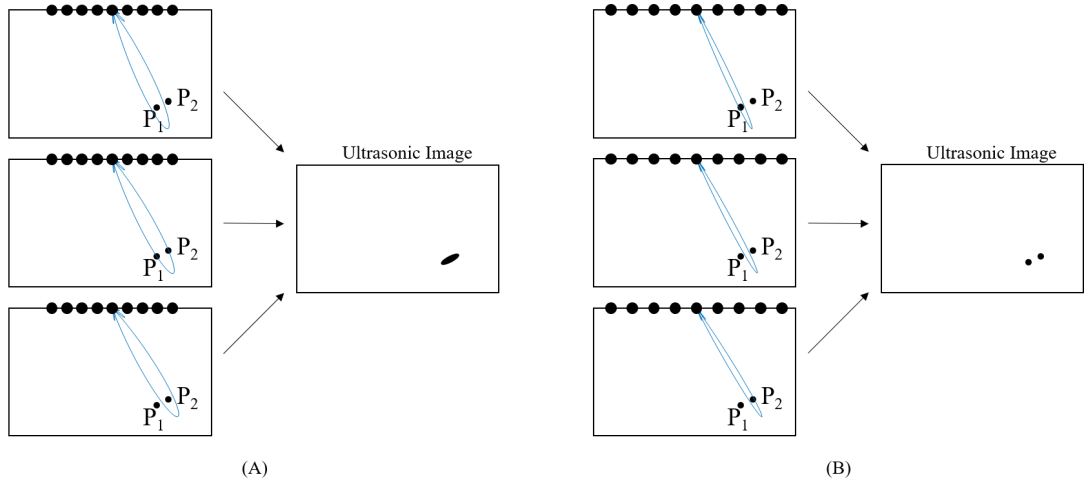


Figure 4.6: Graphical demonstration of the effect of the main lobe on lateral resolution. When the width of the main lobe is larger than the distance between the two features, (A) the two defects are not resolved separately. In comparison, when the width of the main lobe is reduced, the two features are each imaged.

4.2 Two-way Radiation Pattern Optimisation

In the previous subsection the concept of two-way focusing was presented. It was shown how focusing can be achieved in generation and detection independently, meaning that a different pressure field is produced in transmission and reception. Lockwood et al. [68] have utilised this capability of ultrasonic phased arrays in order to optimise the transmit and receive array directivities relative to each other and suppress grating lobes of the sparse arrays, in the two-way focused pressure field. Using the concept of the effective aperture, it was demonstrated that by applying apodisation to two carefully designed sparse arrays, with different generation and detection array layouts, the two-way radiation pattern of a dense array can be achieved. The number of elements in the array was reduced by four times, without compromising the side-lobe to main lobe ratio [68].

However, a considerable disadvantage of this technique was that a fully populated

dense transducer-based phased array had to be partially excited to achieve one sparse array layout for generation and a different sparse array layout for detection, resulting in a highly inefficient use of the transducer-based phased array. Likely for this reason, this technique has not been popular for the use of 1D transducer-based ultrasonic phased arrays.

In contrast to transducer-based arrays, LIPAs are synthetically created and have decoupled generation and detection capabilities. Therefore, it is possible to apply a two-way radiation pattern optimisation, and have multiple generation and detection elements, potentially overlapping with each other, because the array elements are created using light. This flexibility of LIPAs expands the possibilities for this optimisation technique.

For the effective aperture approach presented in [68], the assumption that the generation and detection have the same directivity is made. In this case, the pressure field produced by a generation array is identical to that of a detection array with the same layout. However, the patterns obtained for LU, are not the same (see Section 3.1) and this is not a valid assumption to make. Thus, in the present study, the evaluation is done by the two-way radiation pattern by taking the product of the individual pressure fields, as shown in Section 4.1.

Commonly, apodisation is applied to sparse array designs, in order to achieve optimised beam directivity [68, 74]. This technique entails applying different weighting factors to the array elements, similar to the concept of applying a windowing function in digital signal processing. However, by doing so, the overall array sensitivity is compromised. Figure 4.7 demonstrates the effect of applying a cosine apodisation function on the array sensitivity (see Section 3.4). This is compared to the case where no apodisation is applied, which can be treated as a rectangular apodisation. In transducer-based phased arrays, the excitation function is amplified in order to overcome this reduction in sensitivity. However this method cannot be applied to laser ultrasonics as the maximum excitation function is limited by the ablation threshold. Furthermore transducer-based phased arrays have generally high generation efficiency and detection sensitivity. This is not the case in laser ultrasonics, at the thermoelastic regime, on both accounts, es-

pecially because the main limiting factor for imaging is the low sensitivity. For this reason, in the present study no amplitude apodisation was considered for sparse arrays, in order to avoid reduction in overall sensitivity.

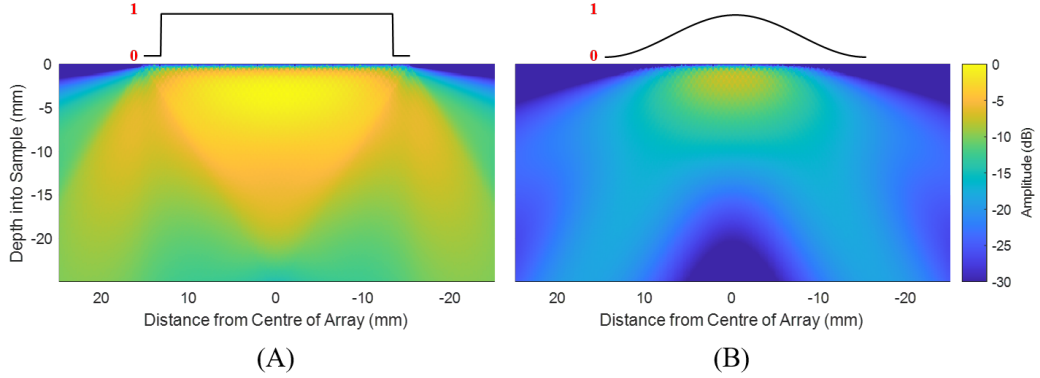


Figure 4.7: Sensitivity maps of a LIPA (50 elements, 0.51 mm inter-element spacing) with no apodisation function (A) and with a cosine apodisation function (B). The graphical representation of the apodisation function used in each case is shown above the respective sensitivity map. Amplitude of the functions is indicated using red 1 (maximum amplitude) and 0 (minimum amplitude)

The two-way radiation pattern optimisation towards grating lobe suppression is evaluated using the model based on Huygens' principle described in the Section 4.1. The angle that the array grating lobes appear at is defined by the amount of spatial under-sampling, which is defined by how large the inter-element spacing is relative to the acoustic wavelength. When the pitch is different for generation and detection, the grating lobes will appear at different angles in transmission as in reception. When the two-way focusing is considered, the product of the generation and detection array directivity achieves suppression of the grating lobes due to the misalignment of these lobes. The concept is visually demonstrated on Fig. 4.8, where the same array was utilised in transmission as in reception (A) and where different array pitch was utilised in transmission and in reception (B). The total number of array elements was 100 in both cases, with 50 generation and 50 detection elements in (A) and 47 generation and 53 detection elements in (B). The parameters utilised were 7.5 MHz ultrasonic frequency, 25 mm aperture, acoustic velocity of 3200 m/s and a focal point at $(x,z)=(0,20)$ mm. A clear difference in grating lobe amplitude can be observed between the two cases.

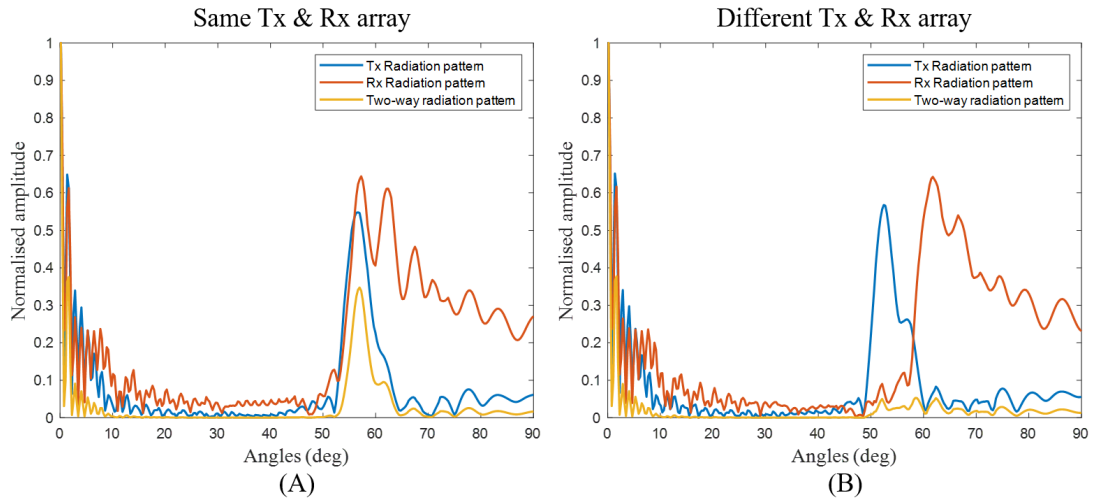


Figure 4.8: Array directivity with same generation and detection layout (50 generation and 50 detection elements) (A) and with different generation and detection layout (47 generation and 53 detection elements) (B). Both arrays were sparse and had the same aperture width (25 mm) and number of total array elements.

The approach taken towards array optimisation in the present study was to select a set of array parameters for either the transmitting or receiving array, such as the array aperture, number of elements and pitch. The other array, either receiving or transmitting, is then varied. That is the number of array elements and corresponding pitch are swept through a range of values. By doing so, the performance of the two-way radiation pattern array can be measured and optimised as a function of generation-to-detection-pitch ratio. The amplitude of the first order grating lobe is measured relative to the main lobe, as a measure of quantitative evaluation between array designs.

In the present study, the generation array was selected to have set parameters of 25 mm aperture and 64 array elements resulting in a pitch of 0.4 mm. The acoustic velocity was chosen to be 3200 m/s, a common value for shear acoustic velocity within aluminium. A lambda of 0.267 mm was selected, in order to achieve high grating lobe amplitudes. In this case the Nyquist sampling criterion is not satisfied as it is smaller than twice the pitch. The corresponding acoustic frequency for this wavelength and velocity was calculated to be 12 MHz. Next, the number of detection elements were varied from 24 to 64 elements. The detection aperture was constant and selected to be

identical to that of the generation array, (i.e. 25 mm). Hence the detection pitch was consequently varied from 1.09 to 0.4 mm. The ratio of the generation versus detection inter-element spacing was used as a comparative measure. This ratio varied from 0.37 (37%) to 1 (100%) and for the value 1 the same layout was used in transmission as in detection. The results of this study can be seen on Fig. 4.9. Higher values mean worse performance due to higher amplitude of artefacts being produced by the grating lobes.

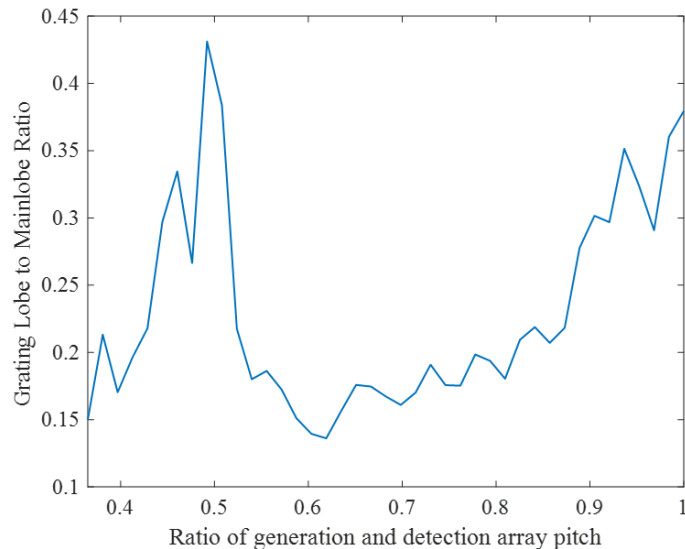


Figure 4.9: Ratio of the first order grating lobe and the main lobe as a function of generation to detection array pitch ratio. The generation array consisted of 64 elements and had a 25 mm aperture. The generation array had a consistent aperture of 25 mm, with the number of elements ranging from 24 to 64, thus achieving variable pitch.

Relative to the case where the same generation and detection layout is used (i.e.: ratio = 1), grating lobes are shown to be reduced from ~ 0.38 to ~ 0.14 relative to the main lobe amplitude, which is a reduction by 63%. This occurs when applying a 0.62 times smaller generation pitch relative to detection pitch. For 0.54 - 0.86 relative pitch, every data point exhibits at least a 43% improvement for grating lobe reduction. However, when the generation inter-element spacing becomes half that of the detection, grating lobes appear at a higher value. This can be explained by the fact that halving the spatial sampling points produces a higher order grating, that occurs at the same angle as the previous order when using twice as many sampling points.

Figure 4.10 demonstrates the effects of higher order grating when halving the number of elements, thereby doubling the inter-element spacing. As the 2^{nd} order grating lobe of the transmission array aligns with the 1^{st} order grating lobe of the detection array, in the two-way radiation pattern a high amplitude grating lobe appears in spite of the different layout used for generation and detection. Thus when designing the generation and detection arrays for two-way radiation pattern optimisation, the detection pitch must not be a multiple of the generation pitch in order to avoid grating lobes.

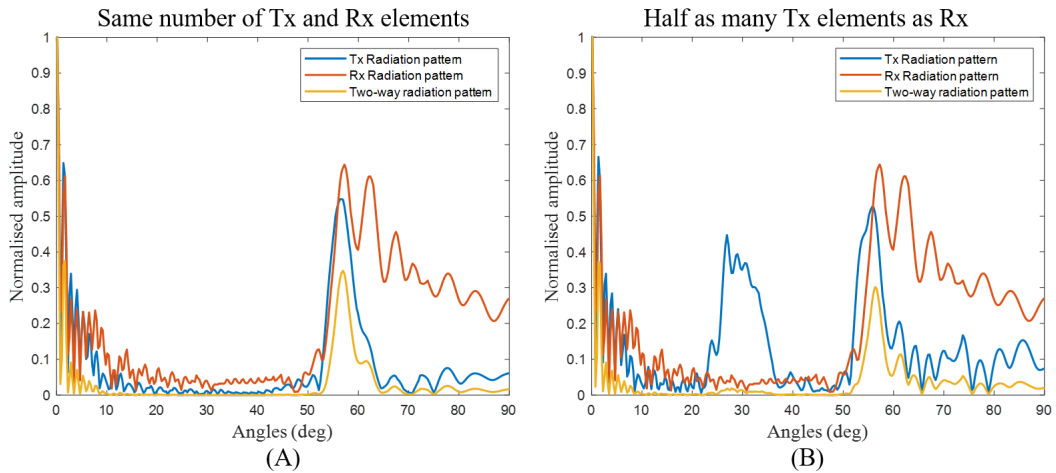


Figure 4.10: Array directivity pattern when using the same Tx and Rx arrays (A) and when the number of Tx elements is half of the Rx elements (B), showing a second order grating in the transmit radiation pattern.

4.3 Aperiodic Sparse Array Design

The other category of sparse designs considered in this work is the random array, which improves the array directivity by breaking the periodicity of the elements [14]. This is because the grating lobes are produced by the periodic under sampling of the waves, as discussed in Section 4.1. While there are various aperiodic sparse array design [12, 71, 75], the one considered in this study is the random array. Random arrays can be performed using a completely randomised process, with elements located at a random position within the aperture. An alternative approach is to apply a restricting rule for the design, such as the bin distribution approach [76], where each element is

randomly placed within a predefined bin, as shown on Fig. 4.11.

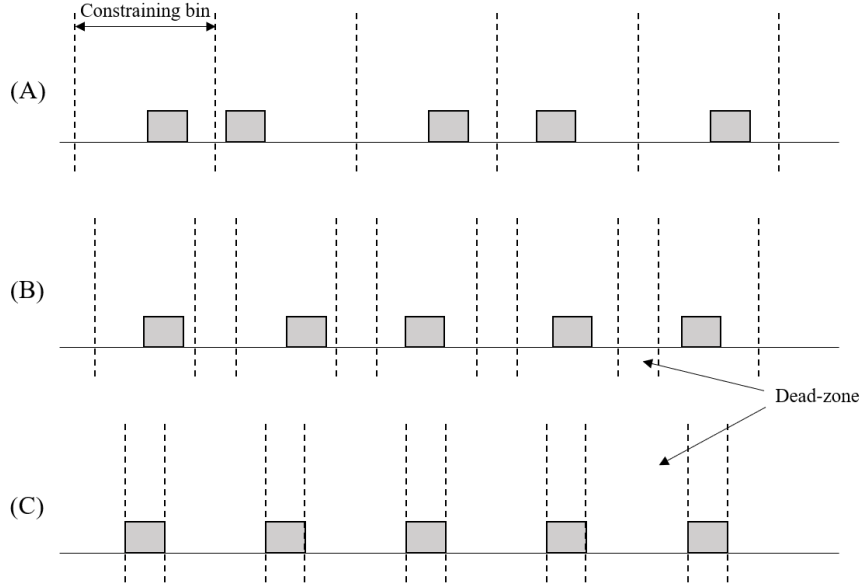


Figure 4.11: Demonstration of how the binned random arrays are designed. Arrays with three different bin sizes are shown: bin size equal to the inter-element spacing (A), bin size smaller than the inter-element spacing but larger than element width (B), bin size of the element width (C). The last array (C) is equivalent to a periodic array. Each element is represented by a gray square.

The centre of the bins are fixed and located periodically within the total array aperture. The elements are then randomly positioned within their corresponding bin. Widening the width of the constraining bin results in increased randomness and when the constraining bin is equal to that of the width of an element, the array exhibits a periodic, non-random layout. This binned approach is utilised in the present study instead of a completely random array in order to avoid the possibility of having significantly denser and less dense areas of the aperture, leading to potential blind-holes in the resulting array sensitivity [76]. Here, the width of the bin is defined relative to the inter-element spacing as a percentage.

4.4 Evaluation of Sparse Laser Induced Phased Arrays

A comparative study is presented here, between the conventional periodic array design with identical transmit and receive apertures, the two-way optimised array and the

random array with the aim to evaluate them. Initially the parameters of the conventional periodic phased array with identical generation and detection arrays are defined. The ultrasonic frequency was selected as 6 MHz leading to an acoustic wavelength of ~ 0.53 mm (acoustic velocity 3200 m/s). The total aperture was selected to be 30 mm, to cover the entire imaging region. In order to achieve $\sim 1:1$ relationship between pitch and λ , to produce high amplitude grating lobe, a pitch of 0.5 mm with 61 elements was chosen.

Two-way optimisation was carried out by using an initial array as described in Section 4.2, with 61 generation and 61 detection elements. Progressively, the distribution of generation and detection elements was varied, by taking away a generation element while at the same time adding a detection element. A distribution of 57 generation and 65 detection elements was found to provide a good level of grating lobe reduction. This translates to a generation pitch of 0.54 mm and detection pitch of 0.47 mm.

The other optimised array, the random array was designed by applying a random variable to the periodic array with same generation and detection pattern, as described in Section 4.3. The bin width was limited to 50% of the 0.5 mm pitch, thus each element was allowed to move either to the left or right by up to 0.25 mm. The array directivity results calculated using the analytical model for these three designs can be seen on Fig. 4.12.

Table 4.1 shows the array parameters along with the performance calculated from Fig. 4.12. These array parameters were used in the experimental setup in order to evaluate the designs in practise. The array parameters were controlled and varied by the LabVIEW code detailed in Chapter 2, while the experimental setup (hardware) did not require any change when switching between array designs. Reconfiguring the LIPA was achieved completely through software.

Sample B was selected for experimental demonstration such that the side-drilled hole, highlighted by a yellow arrow in Fig. 2.7, is imaged from the side indicated by the red arrow on the same figure. From this perspective, a cylindrical defect located ~ 15.5 mm deep from the scan surface is imaged. Gaussian filtering with a 100% bandwidth was applied, centred at 3 MHz, in order to allow detection of the 6 MHz components,

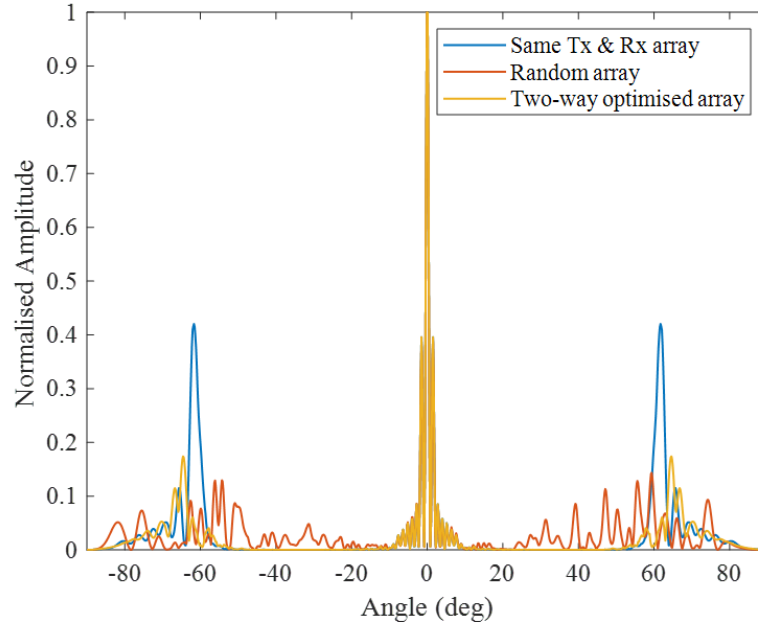


Figure 4.12: Array directivities of three sparse array designs with a total of 122 elements (T_x and R_x): a periodic array with same pitch for T_x and R_x ; a random array with 50% limited bin; a two wave optimised array with detection vs. generation pitch ratio of 87%.

which were utilised in the analytical model. During acquisition each signal was averaged a total of 512 times and the acquisition time of each array was ~ 11 minutes. Regarding post processing of the three arrays' data-sets, two methodologies were followed: The TFM algorithm was applied with and without the VCF algorithm. The reason is that VCF is an algorithm that has been shown to suppress grating lobes as well as increase SNR (See Section 3.2.1) and its effect had to be decoupled from the evaluation of the three arrays due to their design. Two sets of TFM images were produced and are shown in Fig. 4.13, where (A-C) and (D-F) have been processed without and with the VCF algorithm respectively.

The defect can be clearly seen in Fig. 4.13 (D-F) where the VCF algorithm has been applied to the TFM. However high amplitude artefacts can be seen on the image produced by the periodic array utilising the same layout for generation and detection (Fig. 4.13 (D)). This is in good agreement with analytical results from the theoretical model. Based on the calculated array directivities, the random array, utilising identical

Array Design	Tx Elements	Rx Elements	GL to ML Ratio
Same Tx & Rx Layout	61	61	42%
Random	61	61	17%
Two-Way Optimised	57	65	14%

Table 4.1: Array parameters and calculated grating lobe (GL) to main lobe (ML) ratios, linked to Fig. 4.12.

generation and detection layout, exhibited a lower maximum grating lobe peak than the two-way optimised array, however on the experimental results, the random array produced higher peak artefact values. This can be explained when analysing the analytical array directivities from Fig. 4.12. The two-way optimised array has a single prominent peak on either side of the main lobe at $\pm 65^\circ$. In comparison, the random array spreads out its grating lobe levels over the range of angles of the array directivity, thus it produces multiple peaks. While the maximum grating lobe peak is lower than that of the two-way optimised array, there is a high average energy, spread out over multiple grating lobe peaks.

To quantitatively compare the images, two metrics were measured: the image SNR and the peak artefact amplitude. The former was measured by dividing the signal (i.e.: 0 dB, as normalisation is performed relative to this value) by the noise floor. The noise floor was measured between -3 to -15 mm depth. This range was selected in order to exclude the effects of the SAW cross-talk region as well as the defect. The peak artefact level was determined by measuring the highest intensity pixel within this same region. The final measured results can be seen on Table 4.2.

The Random and the Two-way optimised arrays both achieved SNR improvements of ~ 11 dB, when compared to the conventional periodic array which utilised the same generation and detection layout, both with and without utilising the VCF weighting. These arrays also offered reduced peak artefact levels: the Random array by ~ 4 and ~ 7 dB, while the Two-way optimised by ~ 6 and ~ 12 dB, without and with VCF, respectively. This demonstrates that while the two sparse arrays proposed for LIPAs

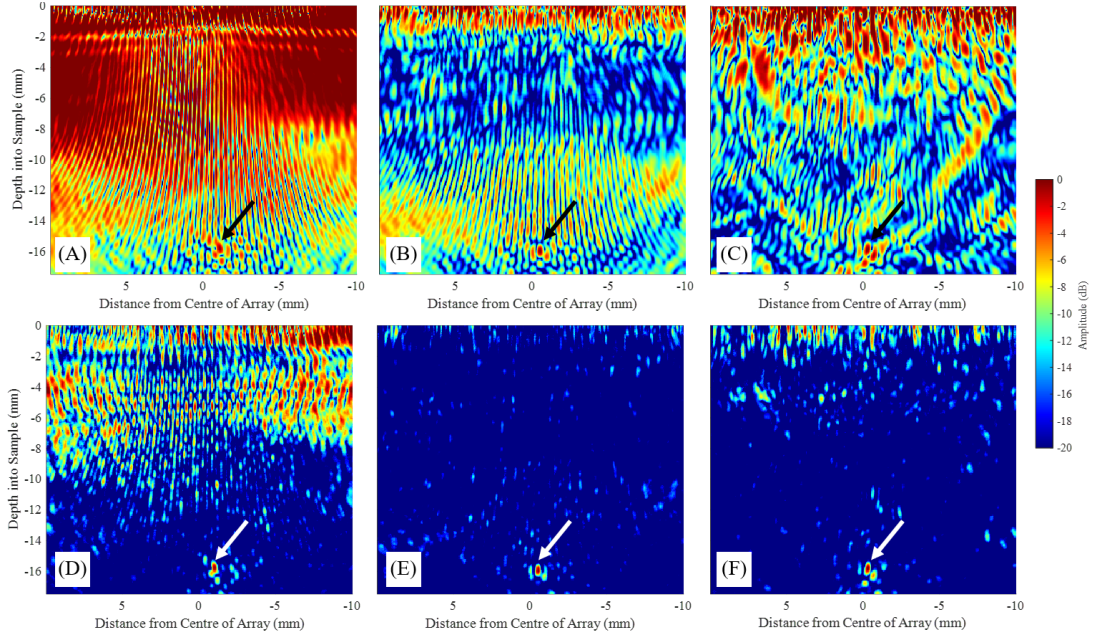


Figure 4.13: Experimental TFM images produced by periodic array utilising the same layout for generation and detection (A,D), two-way optimised array (B,E) and random array (C,F) without (A-C) and with phase coherence (D-F). The defect is indicated on the images by black and white arrows. Different colouring of arrows was utilised to achieve better contrast compared to the ultrasonic images. Filtering was performed at 3 MHz using a 200% bandwidth. Same array parameters are used as for Fig. 4.12.

(Random and Two-way optimised) offer comparable SNR improvements for 2D imaging, the Two-way optimised array offers improved artefact reduction.

4.5 Summary

A study employing sparse array designs for LIPAs was presented in this chapter, towards reducing number of array elements, and the subsequent data acquisition time, while suppressing grating lobes. A comparison between a sparse array with the previously presented layout of LIPAs (i.e.: periodic array with identical generation and detection layout) and the optimised designs was carried out. High intensity artefacts appeared on the image produced by the conventional array (i.e.: periodic array, with same generation and detection layout), which compromised image interpretation. The artefacts at certain points appeared at higher amplitude than the defect itself, even af-

	TFM		TFM + VCF	
	SNR	Peak Artef Amp	SNR	Peak Artef Amp
Same Tx & Rx	4.54 dB	3.67 dB	19.55 dB	1.30 dB
Random	13.29 dB	-0.13 dB	30.38 dB	-6.61 dB
Two-way optimised	14.10 dB	-3.49 dB	30.41 dB	-11.00 dB

Table 4.2: SNR and Peak artefact amplitude of images shown on Fig. 4.13

ter applying phase coherent processing. In comparison, the two optimised arrays were able to suppress grating lobes, which was demonstrated in terms of overall SNR gain as well as lower peak artefact values. Furthermore, after applying the VCF weighting on the optimised array, all artefacts were suppressed below the amplitude of the defect, reducing the probability of false detection.

A theoretical improvement in grating lobe to main lobe ratio from 63% to 28% and 21% was achieved for the two improved designs presented here. The results were experimentally demonstrated by synthesising the three sparse arrays with designs as detailed in the comparative analytical study. The TFM image produced by the periodic array consisting of identical transmit and receive layouts could not be used for defect detection due to the high amplitude artefacts produced by the strong grating lobes. As predicted by the analytical model, the other two designs produced significantly lower grating lobes and thus it was possible to locate the defects on the resulting TFM images.

The sparse array designs explored in this chapter were implemented with a digital filter with an upper cut-off frequency (defined by -6 dB drop) of 6 MHz, corresponding to acoustic wavelength of ~ 0.53 mm for the experimental parameters chosen. A dense array that satisfies the Nyquist sampling theorem would require an inter-element spacing of 0.27 mm, which for this aperture would require 111 array elements. An array consisting of so many elements would acquire 12321 A scan signal, compared to the 3705 and 3721 signals of the two-way optimised and the random array respectively. This translate to an improvement of ~ 3.3 times reduction in data size and consequently acquisition speed.

It is important to note that the scope of this chapter only covered the effects of artefact reduction, while not considering other array performance criteria, such as array sensitivity. An increased number of array elements will always increase array sensitivity, thus while these improved designs reduce artefacts, they do not in fact improve array sensitivity. In other words, a compromise should be made between array element sparsity and sensitivity and it is critical to populate enough array elements, such that sufficient sensitivity is reached within the imaging region.

With this note in mind, the results presented in this chapter demonstrate how and which sparse array designs can be used for reliable defect detection while reducing data acquisition times of ultrasonic phased arrays and maintaining imaging efficiency and imaging quality. For example the results in Fig. 4.13 show that the two-way optimised array is more suitable for consistent imaging quality whereas a random array would be more suitable for image efficiency with respect to artefact levels, when compared with a periodic array using same generation and detection layout. In all cases, these research results pave the way for many more array designs to be implemented for this goal.

Chapter 5

Adaptive Data Acquisition

The Total Focusing Method provides advanced imaging quality compared to other techniques such as the Plane Wave Imaging (PWI) [12], Synthetic Aperture Focusing Technique (SAFT) [49] or B Scan [6], addressing a critical need for high quality imaging in various fields. This capability helped establish TFM as the golden standard of ultrasonic imaging [77, 78]. However, this imaging algorithm requires the Full Matrix Capture acquisition, which means that a signal from each generation and detection element pairs. The total number of signals captured by the FMC is N^2 , where N is the number of phased array elements. In contrast, the other imaging techniques mentioned, PWI, SAFT and B scan only require N number of signals, leading to an N times faster acquisition process, when compared to FMC. For example, in the case of a 128-element phased array this therefore would lead to a 128 times faster acquisition. Considering the acquisition time needed for the LIPA image presented in Fig. 3.5, in Section 3.2, the 30 minute scan for FMC would be reduced to 11 seconds if SAFT was utilised instead of TFM for imaging. In other words, the TFM imaging quality is counterbalanced by the data acquisition speed required, compared to other, lower imaging quality algorithms. This is one of the main reasons why laser ultrasonic imaging has been limited to B scan and SAFT until now. Data acquisition speed could be increased by hardware improvements such as using a laser with faster repetition rate, or a more sensitive detector, which would reduce the the need for averaging. However these improvements alone are not sufficient to entirely address this problem. Instead, the acquisition method

needed to achieve TFM imaging must be reconsidered. The aim of this chapter is to introduce a novel data acquisition strategy that improves acquisition speed while retaining the imaging quality of TFM, thus increasing overall efficiency of the phased array. This method reduces data volume, as well as data acquisition time, making it ideal for implementation using 2D ultrasonic arrays.

A significant limitation of the FMC acquisition is the considerable data acquisition time and the large data-set volumes that are produced especially related to 3D imaging [70]. While it provides all the information that can be acquired from a single position of the phased array, in many cases this approach is redundant. When a component to be inspected is flawless, acquiring the maximum available information is unnecessary. Similarly when a defect is present, in a small confined region of a large component, acquiring the same amount of information throughout the sample, regardless of how much *useful* information is obtained, is a highly inefficient approach.

In certain applications ultrasonic imaging is required to be performed rapidly. Such applications include in process inspection during manufacturing such as additive manufacturing, where components are built layer by layer. In this case, in-process inspection can reduce manufacturing time, wastage and costs. Another example is medical imaging where the acquisition time must be faster than the fluctuations of muscles, other organs or blood flow.

All the imaging techniques mentioned above have been developed for transducer-based ultrasonic phased array designs. These transducer-based arrays are rigid, that is their characteristics: number of elements, inter-element spacing and frequency are defined and fixed during manufacturing of the phased array probe. In contrast, the equivalent LIPA characteristics can be defined during data acquisition, thus they are completely flexible and can be changed on-the-fly, during acquisition. With this added level of freedom, the capabilities of ultrasonic phased arrays are considerably extended with the potential to create new array designs, acquisition techniques and data processing algorithms that are more efficient and have higher performance than that of the transducer-based counterparts.

In this chapter this flexibility is used to challenge the current golden standard of ul-

trasonic imaging, the FMC, by creating an adaptive acquisition method. The proposed method, called the Selective Matrix Capture, deploys a decision-based algorithm to adapt the array parameters to the internal features detected, thus it achieves a highly efficient acquisition method without compromising imaging quality.

5.1 Selective Matrix Capture Concept

Using the Full Matrix Capture data acquisition method, a large volume of data is acquired equally over the aperture, providing high quality imaging throughout the constructed image. However, tested components commonly do not contain any defects, or when they do these are confined to a small region within a large area, making it unnecessary and redundant to use high quality inspection, uniformly, throughout the entirety of the test object. Instead, using an adaptive acquisition method, producing images with high quality only where features are present and reduced quality where nothing is to be observed, data acquisition time and data size can be improved.

The Total Focus Method imaging algorithm sums the A scans signals of the Full Matrix according to the delay laws for each user-defined pixel. However, as demonstrated previously in Chapter 3 by the sensitivity maps, it is evident that not all elements will have equal contribution of energy and equal sensitivity to a reflection from a defect, depending on its location. In fact, various elements might not provide any contribution to signals when they have sufficiently low directivity or sensitivity towards the said defect as shown on Fig. 5.1. In these cases when low generation directivity and/or detection sensitivity are observed, the acquired signal will only contribute to the incoherent noise originating from structural features as the ultrasonic echo from defects is absent from the A scan signal. In other words, these signals are not only redundant but they can degrade the quality of the ultrasonic image. Thus, acquiring only the information-rich (i.e.: high directivity and detection sensitivity) signals is expected to lead to improvement of signal level as well as a significant increase in acquisition time.

Figure 5.2 shows a matrix of how much sensitivity (i.e. useful information in the signal) is achieved by every generation and detection element combination of a 90 element array, with an aperture of 30 mm, for a defect located at 15 mm depth, hori-

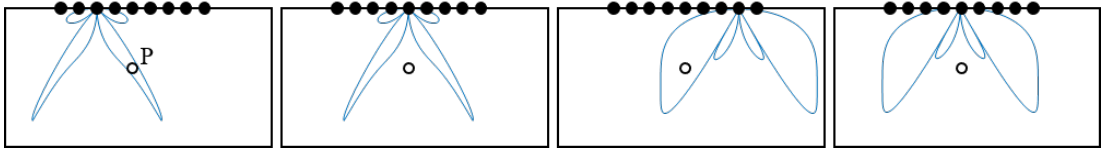


Figure 5.1: Graphical representation of generation and detection efficiency relative to point P, at various locations. Black dots array element positions.

zonally at the centre of the array. In Fig. 5.2, the colour represents how much useful information regarding the defect, is captured in the respective signal of a specific generation/detection element combination. There are 692 pixels in this matrix, each demonstrating 100-50% of the maximum achievable sensitivity (pixels in the yellow range from 0 to -6 dB). On the other hand there are 2070 pixels, from generation/detection combinations with signals that demonstrate 3% or less of sensitivity (pixels in the blue range from -27 to -30 dB). The total number of signals captured by FMC would be 8100, for this array and the majority of the useful information for the specific location of the defect would be contained in the 692 of these signals displayed in yellow (0 to -6 dB). This example highlights, why the FMC acquisition is highly redundant, when every element combination is captured without discrimination on how much useful information is captured in these signals.

The proposed acquisition method, named the Selective Matrix Capture (SMC), consists of two stages. The initial stage involves a rapid scan with low element count and large pitch covering the whole region to be inspected. The images generated are of low quality with the only aim being to locating defects. Having obtained information of the defects' location from the first stage, the second stage is performed, which provides an image with high quality, at the region of interest only. For the second stage, two alternative implementations are proposed, first a localised, focused scan, with the elements placed in an equidistant manner, at a location of high directivity and sensitivity. This generally corresponds to a smaller aperture than the one synthesised in the first stage. The alternative array design has the same aperture as the first stage, meaning it makes use of the entire inspection area, however it utilises a sparse array layout with varying element density. In this layout, more elements are placed in regions of high sensitivity, while keeping the number of elements low where sensitivity is lower. In the case where

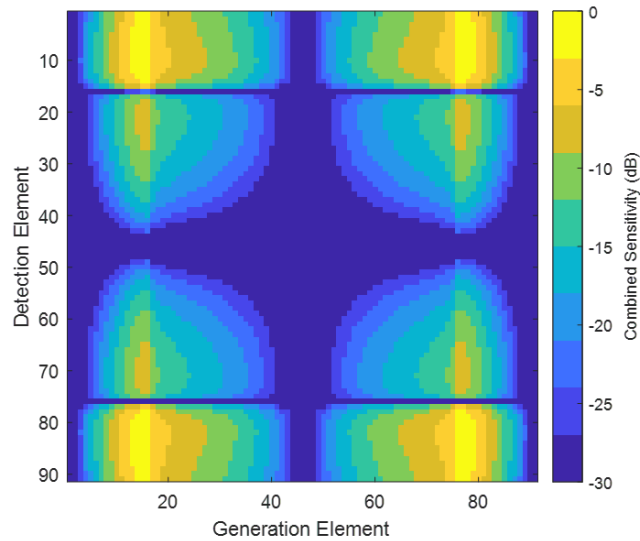


Figure 5.2: Sensitivity matrix for a 90 element array, with discretised colour-bar. Each change in colour represents a -3 dB drop in sensitivity, equal to halving the sensitivity each time. This matrix is produced by assuming that the defect is at the centre of the inspection area.

the first stage indicates no defects present in the test object, the process ends, leading to a very fast inspection, confirming a flawless test object. As there are no features to image, the low quality images obtained during the first stage provides the necessary information, confirming the lack of defect.

The following sections will detail the first and second stages. Two alternative strategies are detailed for the second stage, as mentioned previously.

5.2 SMC stage 1: Defect Detection

5.2.1 Continuous Data Acquisition

The aim of the defect detection stage (stage 1) is to identify the number of defects within the sample and locate their position. High quality imaging is not required, as defect characterisation is not performed at this stage. The goal is to capture the minimum number of signals with which the defects can be located decisively in order to achieve a high data acquisition speed. This value is found by continuously processing

the acquired data until the defects are located or a definite decision that no defects are present can be made.

However, creating an image after every A scan signal acquired is not practical and would be computationally demanding. Furthermore, acquiring the signals in a linear manner for a dense array over the imaging region would result in uneven sensitivities as the signals are continuously processed, as illustrated in Fig. 5.3 (A) by the related sensitivity maps. If we assume that all the available phased array elements are that of a dense array and acquiring signals individually, after N acquisitions (with N being the number of phased array elements) one row of the Full Matrix will be available. In this case this would correspond to detecting at all possible locations while generating at the first element position only. This provides good sensitivity towards ± 35 degrees to the first element, due to the sensitivity pattern of laser ultrasound, however the overall sensitivity throughout the image is low, with at least around half of the image (i.e.: left of the 0 mm mark horizontally in Fig. 5.3 (A)) being practically a blind zone. These blind zones have an adverse effect on imaging as all the defects located within these zones will not be detected due to the lack of sensitivity.

To overcome this and achieve a more uniform sensitivity, an alternative approach is presented: rather than processing the signals in a linear manner for the dense array, the signals can be acquired in an equally spread pattern over the Full Matrix, as demonstrated Fig. 5.3 (B). Both images shown in Fig. 5.3 were normalised to the highest intensity value from the sensitivity map in Fig. 5.3 (A). These sensitivity maps demonstrate that, while the maximum sensitivity has decreased by 3.2 dB in Fig. 5.3 (B), a significantly larger portion of the imaging region is now insonified, while acquiring the same number of signals. Thus, more uniform sensitivity can be achieved by carefully considering the strategy for continuous data acquisition, increasing the probability of detection throughout the imaged region.

5.2.2 Iterative Array Construction

Designing the continuous acquisition process is a complex subject, as the exact number of signals required to accurately locate defects is not known. In the present study the

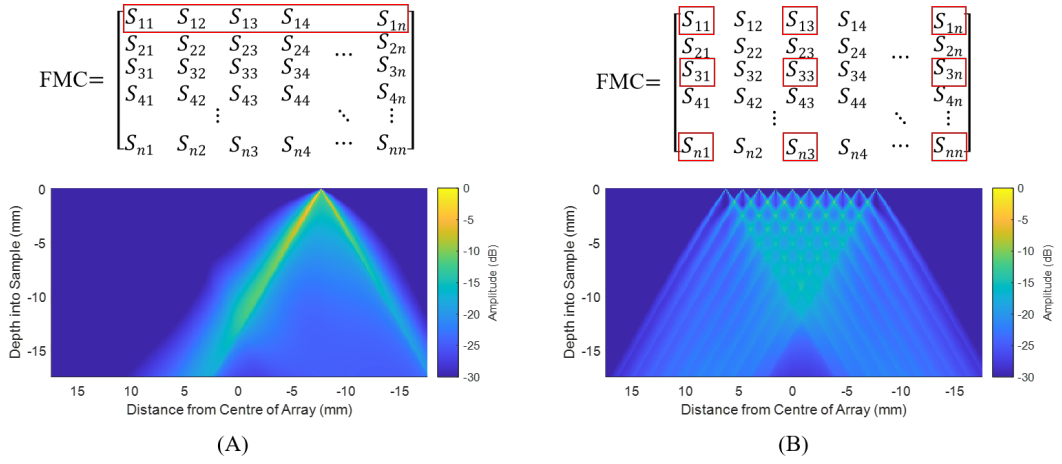


Figure 5.3: Sensitivity maps calculated for partial acquisition of a fully populated dense array with 100 possible element locations. Acquisition of 100 signals is achieved with a single generation point and all detection points used (A), compared to a sparse, periodic array of equal number of generation and detection points (i.e.: 10 generation and 10 detection positions), also acquiring 100 signals (B). The captured A scan signals of the Full Matrix are shown in each case in red squares above each map.

iterative method is proposed that finds the least amount of information required to locate defects. The first iteration consists of a sparse array with very coarse pitch that provides a sufficient aperture width to image the entire region to be inspected. In subsequent iterations the inter-element spacing is continuously decreased and the number of array elements is increased in order to acquire increasing amounts of information. Sensitivity maps for two subsequent iterations are presented in Fig. 5.4 alongside the resulting Full Matrix. The number of array elements is increased two-fold for the sensitivity map shown in Fig. 5.4 (B) when compared to (A). Both images were normalised to the highest intensity value from the sensitivity map in Fig. 5.4 (B).

If we consider halving the inter-element spacing, with each subsequent iteration, the increase in number of array elements can be defined by the following equation:

$$N_x = (N_{x-1} - 1)2 + 1 \quad (5.1)$$

Where N_x and N_{x-1} are the number of array elements used for the current iteration and the previous iteration, respectively. This is roughly an increase of a factor of 2, which translate to the Full Matrix of the current iteration containing roughly 4 times

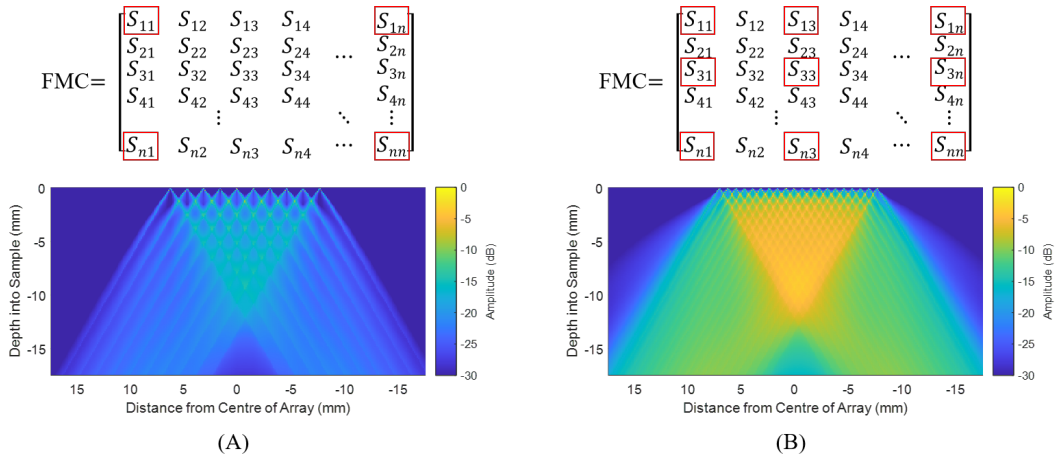


Figure 5.4: Sensitivity maps of two sparse arrays utilising 10 elements (A) and 20 elements (B). The captured elements of the N element Full Matrix are shown in each case in red squares above each map.

more signals compared to the previous iteration.

The overall sensitivity of the two subsequent sensitivity maps from Fig. 5.4, exhibits an average difference of 12 dB, which translates to a linear value of 4 time increase. This means that when the pitch was halved, increasing the number of signals by a factor of 4, the sensitivity increased by the same amount. Thereby we can conclude that there is a linear relationship between number of A scan signals captured and the array sensitivity.

As stated before, the aim of stage 1 of the SMC is to decisively locate defects within the sample, while capturing the least amount of data. Thus, as soon as the defects appear on the images, the process stops and moves on to the second stage. The criteria for measuring the appearance of defects manually is described in the following subsection.

5.2.3 Statistical Defect Detection

The first stage is concluded when the defects can be decisively located, or when the lack of defects has been confirmed. Accurate defect detection without producing false positives and false negatives is currently a prevalent challenge in the field of NDE. Automated inspection and analysis has been pinpointed as a critical target for future

NDE aims [53,79]. Currently, in most cases, NDE technicians interpret the ultrasonic data to evaluate the presence and location of defects. This approach can be prone to human error, it is time consuming and financially demanding. Human interpretation would be limiting the adaptive acquisition as images are to be formed in time intervals of the order of seconds between iterations, not providing sufficient time for manual assessment of individual images. Although this technique in its current implementation is not a fully automated process, the defect detection method presented in this subsection has the potential to provide a tool for automated decision making. By automating the defect detection stage, the speed of the process is increased, while achieving higher accuracy and reliability, as the human factor is excluded and the process is done purely on a quantitative measure.

A novel, image interpretation tool is presented in this section for defect detection and defect localisation on ultrasonic images. This method relies on the fact that the noise floor of ultrasonic images produced by TFM exhibits a Rayleigh distribution when plotted on an amplitude histogram [80,81]. The defect detection is done by analysing this Rayleigh curve on the histogram of the ultrasonic image. The amplitude of the ultrasonic noise floor will always occur with the same relative values (i.e.: a Rayleigh distribution) however its absolute values will differ depending on the ultrasonic image, due to the fact that during the normalisation process, all pixel values are re-scaled relative to the highest value on the image. As Fig. 5.5 demonstrates, a clear shift can be observed in the location of peak of the Rayleigh curve within the histogram between sections of the image with a defect (left red dashed square) as opposed to an image with no defect (right red dashed square). This can be explained by the fact that, when no defect is present, the highest intensity pixel will be that of the noise floor, thus the highest value of the Rayleigh curve is 0 dB. When a defect is present and has an SNR higher than 1 (i.e.: defect has higher value than the noise), the highest intensity pixel will be the defect, and the highest intensity pixel of the noise floor on the histogram will be shifted by the same amount that the SNR is increased by (e.g.: 10 dB SNR improvement leads to 10 dB shift of the Rayleigh curve).

This technique is used during the defect detection stage (stage 1) to established

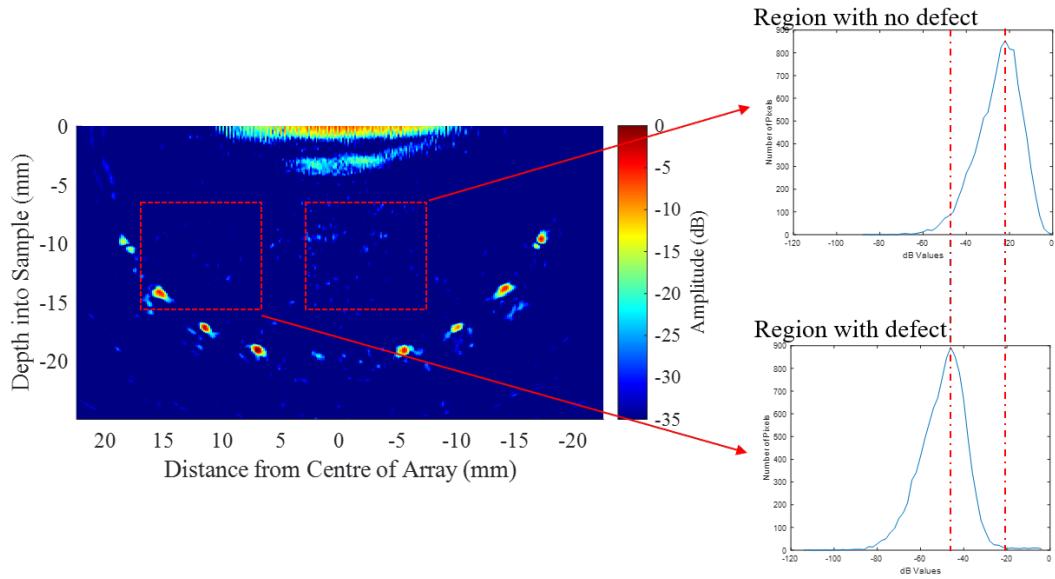


Figure 5.5: Pixel intensity distribution of a region with and without a defect. Image was produced by a 161 element LIPA, with a 0.155 inter-element spacing.

when the defects can be located. Thus, when a shift in the Rayleigh distribution is observed, the first stage of SMC is terminated and the location of the defects is stored for the subsequent stage, to be used for reconfiguring the array in order to better resolve the defect. Alternatively, when the iterative process has been running for a sufficient amount of time and the sensitivity is sufficiently high to detect any defects, if the Rayleigh curve has not shifted, the sample is declared defect-free. In this case the process terminates after the first stage, which is a rapid scan, leading to a significant inspection speed improvement over an acquisition with a conventional dense and fully populated array.

An important factor to consider is the effect that artefacts have on this defect detection process. Artefacts can appear as high intensity erroneous features on ultrasonic images caused by a wide variety of effects, such as grating lobes. A specific artefact that commonly occurs in laser ultrasonic imaging is the SAW cross-talk region, which has been described in Section 3.2. These artefacts do not exhibit a Rayleigh distribution, and they can appear at amplitudes higher or lower than the intensity distribution of the noise floor. When they appear at higher intensity than the maximum value of the noise floor, the defect detection technique detailed in this section will identify a shift

in the Rayleigh curve and thus will incorrectly conclude that a defect can be found, as demonstrated on Fig. 5.6.

To account for erroneous detection of artefacts, in its current form, the defect detection technique excludes the region containing the SAW cross-talk region. This, currently limits the technique’s ability to detect defects within this region masked by high amplitude surface waves, which can extend as deep as 3-8 mm from the inspection surface, depending on aperture, material of the sample, digital filtering, imaging mode and imaging algorithm.

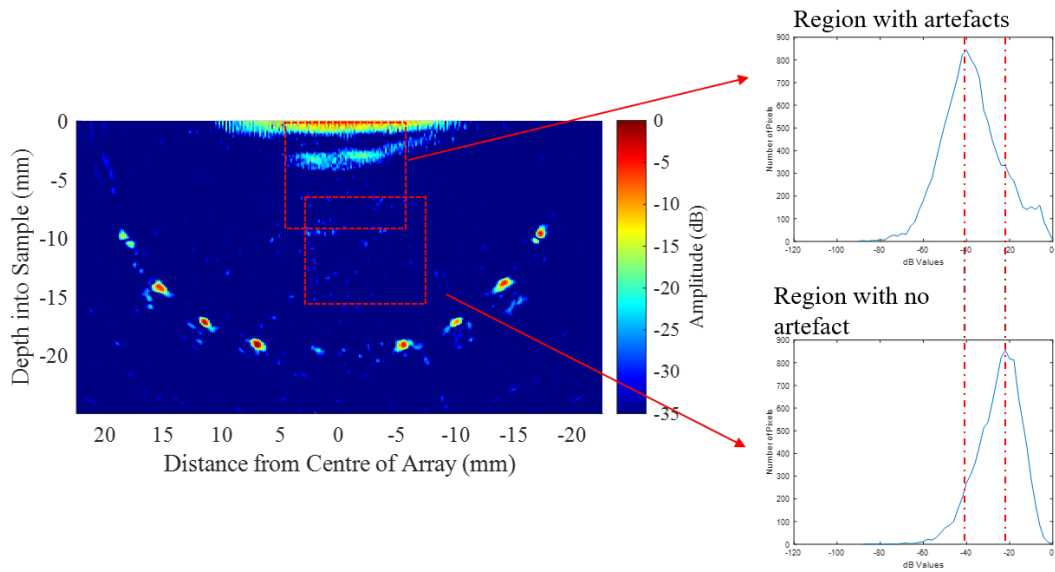


Figure 5.6: Pixel intensity distribution of a region with and without SAW cross-talk. The TFM image was produced by a 161 element LIPA, with a 0.155 inter-element spacing and a digital filter of 5 MHz centre frequency.

5.3 SMC stage 2: Defect Resolving Stage

The initial stage of SMC provides low quality ultrasonic images for detecting and locating potential defects within the test sample. The second stage, is aimed at providing a high quality image in order to resolve and characterise the defects using the information about defect location. This is achieved by optimising the phased array element positions in order to capture the most information-rich signals, by calculating the laser

ultrasound directivities and detection sensitivities at each possible generation and detection points, relative to Region of Interest (ROI). This is then used to find the optimal generation and detection positions.

The following section and Fig. 5.7 describe the process of calculating the generation and detection efficiency towards the ROI. The resulting values are named the surface projected directivity and the surface projected detection sensitivity.

The process of calculating the surface projected detection sensitivity and directivity is described by the following steps:

1. Divide the surface of the test object into multiple sampling points.
2. Calculate the angle relative to the surface normal using the relative horizontal and vertical distance between sampling points and the ROI. See 5.7.
3. Calculate the amplitude to and from the ROI by measuring the directivity and detection sensitivity patterns at the angles derived in step 2.

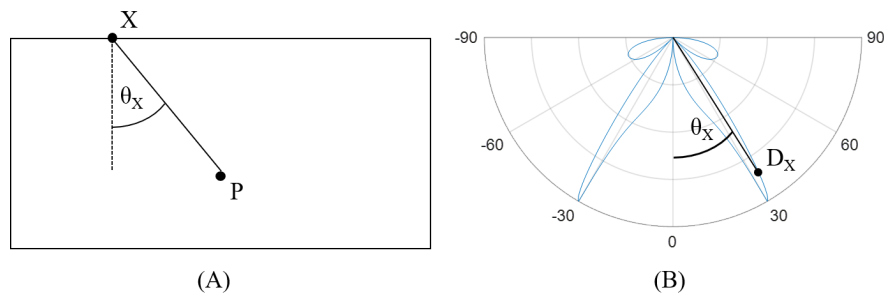


Figure 5.7: Surface projection of laser ultrasonic directivity pattern for a specific defect located at point P.

Examples of the surface projected directivity and sensitivity, produced by the above detailed method, can be seen in Fig. 5.8. In the inspection case presented in these figures, the defect, or ROI, was assumed to be located on the line defined by the centre of the LIPA aperture the test object with the possible range of LIPA scan angles of ± 54 degrees, between the two edges of the top surface.

The optimal generation and detection positions can be deduced from the maxima of the surface projected directivity and detection sensitivity. In this work two methodolo-

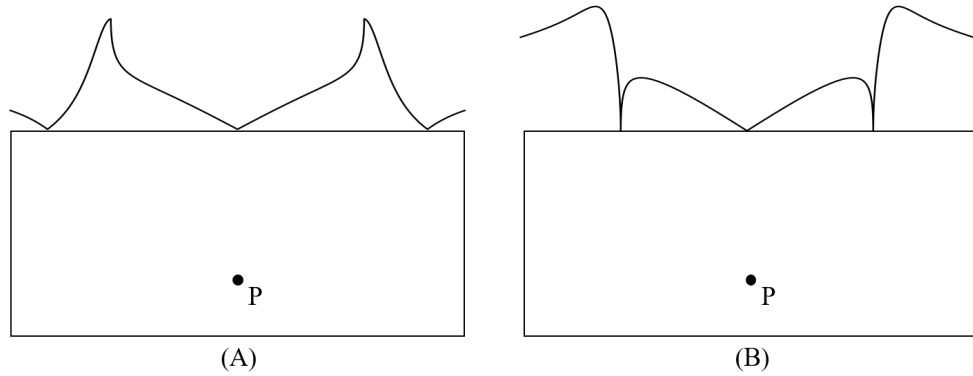


Figure 5.8: Surface projected directivity (A) and detection sensitivity (B), when the available LIPA scanning angles to point P are ± 54 degrees with respect to the two limits of the scan surface. The material was assumed to be aluminium and only shear mode was considered in the calculations (Eq. 3.2 and 3.4)

gies are proposed for designing arrays with optimised element positions, based on the surface projected patterns. The first is based on placing equidistant elements within the highest intensity regions of the surface projections, while the second utilises a novel phased array design concept in NDE, with varying inter-element spacing based on the sensitivity between each adjacent element pair.

5.3.1 Sensitivity Threshold Method

Using the concepts of common phased arrays, the simplest approach of designing an array is to place elements with constant pitch, in a periodic manner to populate the aperture. In this subsection this approach is utilised to design the optimised array. The aperture width and location is defined by applying a threshold to the surface projections. Areas of the surface where good directivity and detection sensitivity can be achieved are selected as the sub-apertures of the array, while parts of the surface where low directivity or detection sensitivity are exhibited are not populated with any elements.

This selection is carried out by placing a threshold on the surface projections: the location of the surface where the directivity and detection sensitivity are higher than the selected threshold is selected as the array sub-aperture. The threshold must be

considered carefully as this will have a high impact on the imaging. Altering the threshold directly affects the width of the aperture. A common value used in the field of NDE for evaluation is the -6 dB drop, which translates to a linear decrease of 50% relative to the maximum [82]. For this reason, in this work, the -6 dB drop is selected as the threshold for this technique. The -6 dB threshold and the consequent apertures calculated for the generation array, based on the surface projected directivity can be seen on Fig. 5.9

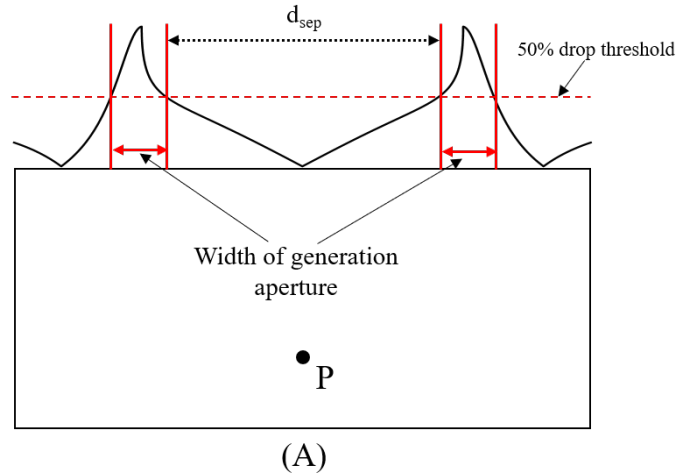


Figure 5.9: Threshold method for calculating the optimal element locations based on the surface-projected directivity for optimal inspection of point P. Red arrows indicate the generation aperture width. Black dashed arrow represents the distance between the two apertures (d_{sep}).

When comparing the surface projected patterns shown in Fig. 5.8, the surface projected detection sensitivity exhibits a considerable wider region within the -6 dB drop, than the surface projected directivity. For the directivity, -6 dB drop is achieved between $\pm 25.55^\circ$ and $\pm 35.71^\circ$ while the threshold for detection sensitivity is set at $\pm 30.86^\circ$ and $\pm 73.04^\circ$. This in most cases would lead to an array with unfeasible aperture width for detection.

To compensate for this, a restriction is applied when calculating the optimal detection element positions. In this restriction the aperture width is set to be identical to the aperture width of the generation array. The start of each sub aperture will be located at the -6 dB threshold closer to the ROI in order to reduce the inspection angles for

better focusing abilities. This is demonstrated visually on Fig. 5.10.

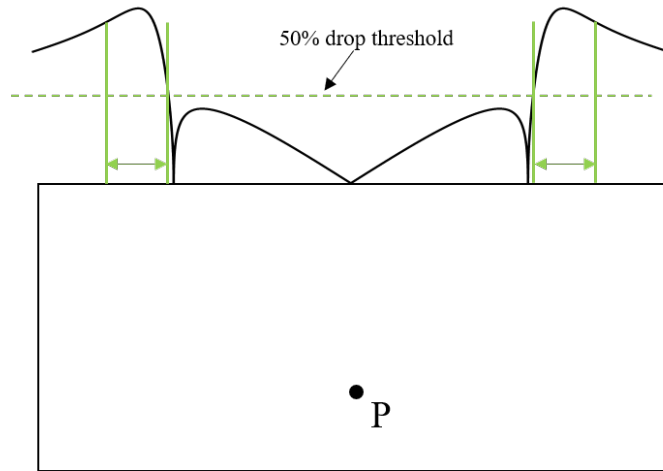


Figure 5.10: Threshold method for calculating the optimal element locations based on the surface-projected detection sensitivity for point P. Green arrows indicate the detection aperture width.

The threshold method was designed to achieve the highest possible SNR by capturing information rich signals while ignoring parts of the surface where only noise can be captured. Besides SNR, another important factor for ultrasonic imaging is the ability to focus. As described in Section 4.1, the main factor controlling lateral resolution is the width of the aperture. A direct relationship can be observed between lateral resolution and aperture, thereby a wider aperture leads to increased lateral resolution.

In the case shown in Fig. 5.9 and 5.10, the sub apertures separated by a distance (d_{sep} in Fig. 5.9) provide a large total aperture relative to the ROI. In contrast if the ROI was placed closer to either side of the test object or the inspection surface was restricted by other means (e.g.: inspection in places of restricted access, such as an aeroengine), the scanning angles might be limited to one peak of the directivity and detection sensitivity patterns. Considering this, the total aperture would be constrained to a single sub aperture, significantly compromising the lateral resolution. This is visually demonstrated on Fig. 5.11.

In the following chapter an alternative design ideology is presented that overcomes this challenge by spreading out the elements over the total scan region according to the surface projected patterns.

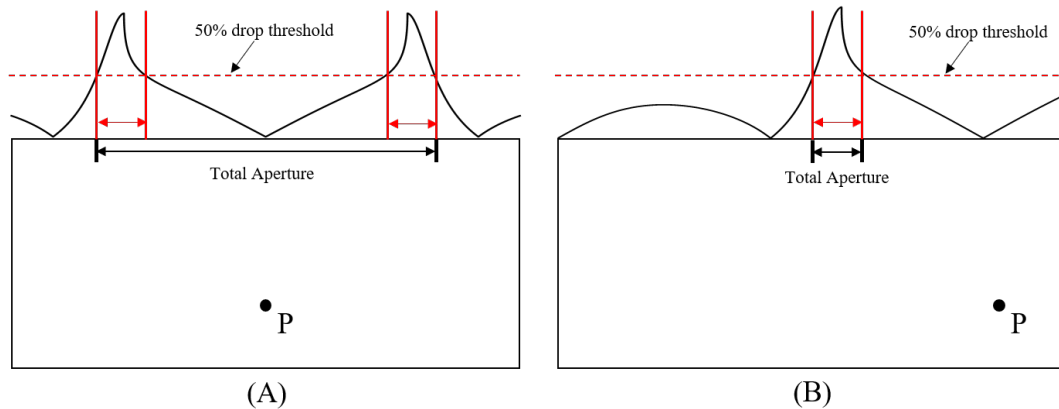


Figure 5.11: Demonstration of how the total aperture varies depending on the available inspection angle relative to the region of interest (point P). When the threshold includes peaks from both the negative and positive peaks (A) a large total aperture is achieved. In contrast when the available inspection angles are limited to one peak (B), the total aperture is significantly reduced

5.3.2 Sensitivity-Based Element Distribution

The method described in the previous subsection provided the simplest approach to selecting the element positions for highest generation and detection efficiency. As stated at the end of the subsection, a downside of this technique is the potential decrease in focusing ability when a defect is located at an unfavourable location (i.e.: scan region is restricted, limiting access to negative and positive peaks of the surface projected patterns).

This problem can be addressed by extending the total aperture. In this work, this was achieved by developing a novel phased array design concept, called the Sensitivity-based Element Distribution (SED). This design method utilises non-linear, non-periodic inter-element spacing, which is defined by the surface projected patterns. Regions on the aperture with high sensitivity and directivity towards the ROI have higher element density (i.e.: more elements, with smaller pitch), while regions with lower sensitivity and directivity contain fewer elements. By doing so the total aperture is expanded while a large number of redundant signals are not captured, as would be the case with a fully populated dense array. The arrays produced by the SED method achieve higher SNR than an equidistant array with a periodic layout, due to the high concentration of

elements in the high directivity and detection sensitivity regions. Another advantage of this technique is the reduction of grating lobe amplitudes due to the layout exhibiting a non-linear density, as demonstrated by Alles et al. [71, 83].

Calculating the inter-element spacing is done by integrating the entire surface projected patterns. The inspection surface is then divided to a number of segments dictated by the total number of array elements. The width of each section is defined such that the integral of the surface projected pattern has the same value within each section. The width of the section is then used as the inter-element spacing of the array. This process is visually demonstrated in Fig. 5.12 and mathematically, described by the following equation:

$$\int_{E_x}^{E_{x+1}} f(x) dx = \int_{E_{x+1}}^{E_{x+2}} f(x) dx \quad (5.2)$$

Where, E_x is the element at position x , with $x = 1, 2, \dots, n$, where n is the total number of array elements. $f(x)$ is the surface projected directivity when designing the generation array or the surface projected detection sensitivity when designing the detection array.

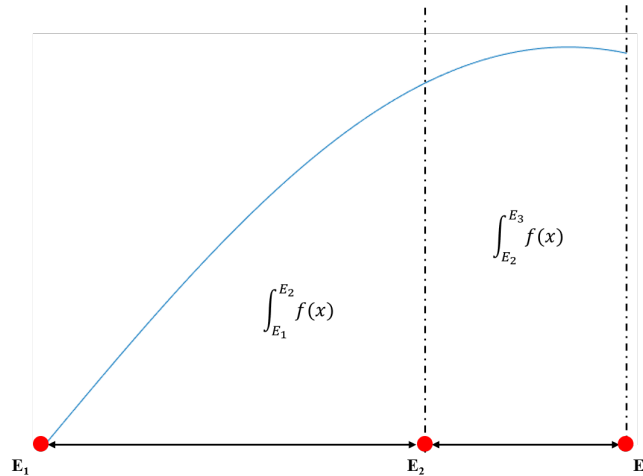


Figure 5.12: Function defining the array density and the respective elements represented by red dots. The integral of the function between each two adjacent element is equal to the integral between the other two adjacent elements

As the surface projected directivity and detection sensitivity patterns are not identi-

cal, it follows that the layout calculated through sensitivity-based element distribution will be different for the generation and detection arrays. An example demonstration of layouts produced using the SED method, can be seen in Fig. 5.13 using the surface projections from Fig. 5.9 and 5.10.

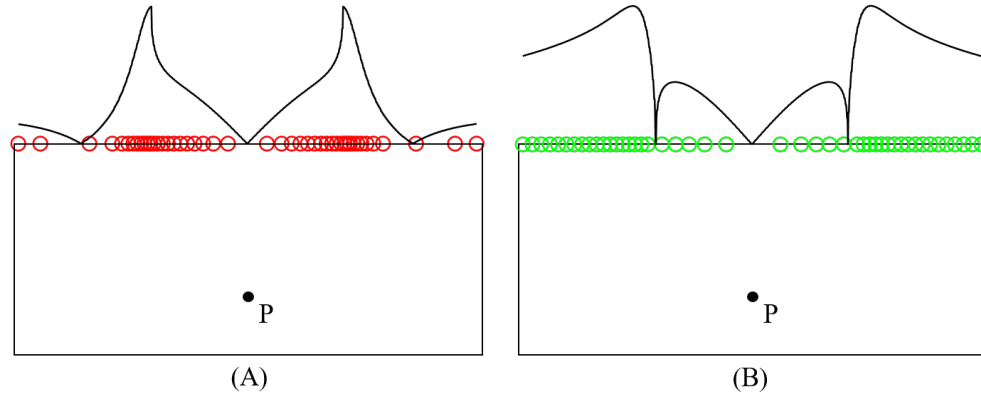


Figure 5.13: Generation (A) and Detection (B) SED layout for surface projections. Calculations were based on aluminium sample using 46 elements, with depth of defect at 11 mm with an available inspection area of 30 mm (maximum aperture for LIPA).

5.4 Experimental Validation of Adaptive Acquisition

In order to validate the proposed technique experimentally, Sample B (see Fig. 2.7) was selected to be imaged. In Fig. 5.14 a photo of the scan surface of the sample (A), and a diagram of the defect with its relative location to the array apertures (B) are shown. There are two apertures shown on this diagram, a 30 mm wide and a 22 mm wide apertures. The reason for utilising two apertures will be explained further on, in this section.

The aim of this study is to image the defect highlighted in Fig. 2.7 by the yellow arrow, which is also shown in Fig. 5.14 (B). Initially, a dense array was scanned over the entire scan region, which in this case was defined as 30 mm wide region (See Fig. 5.14), centred around the defect. The dense array was designed to satisfy the Nyquist sampling theorem up to 10 MHz, for shear wave mode propagating in aluminium, thus the inter-element spacing was defined as 0.155 mm.

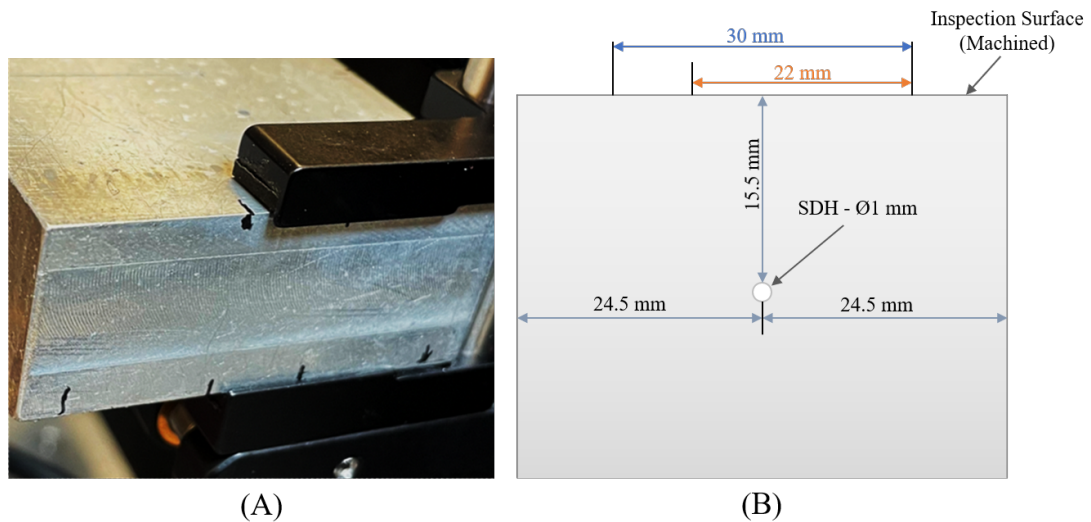


Figure 5.14: Photo of the machined scan surface (A) and a diagram of the sample showing the location of the 1 mm side-drilled hole (SDH) relative to the array apertures (B). The two aperture widths utilised in this study are indicated by a blue (30 mm wide) and an orange (22 mm wide) arrows.

Three arrays were scanned in order to demonstrate the defect detection stage of SMC (stage 1), iteratively increasing the number of elements, and decreasing the inter-element spacing between each scan. The three arrays were designed to contain 10, 15 and 30 elements, corresponding to 3, 2 and 1 mm pitch, respectively. A signal averaging of 32 was applied for each A scan signal during acquisition. Furthermore, a band-pass, digital Gaussian filter was applied to the acquired data-sets in post-processing centred at 5.5 MHz, with a bandwidth of 100%. Phase coherent weighting (i.e.: VCF) was utilised for each TFM image in order to suppress the effects of grating lobes for these sparsely populated arrays. The images that were produced can be seen in Fig. 5.15. The images produced by the first two iterations do not provide sufficiently high SNR to show the defect, however on the third image, the defect can be clearly located at around a depth of 15 mm and horizontally at the centre of the array. The images were plotted against a grey-scale colour-bar in order to achieve a higher contrast for improved visual inspection.

The defect detection is quantitatively confirmed by observing the pixel distribution of the images, shown on Fig. 5.16. Rayleigh curve fitting was performed during the

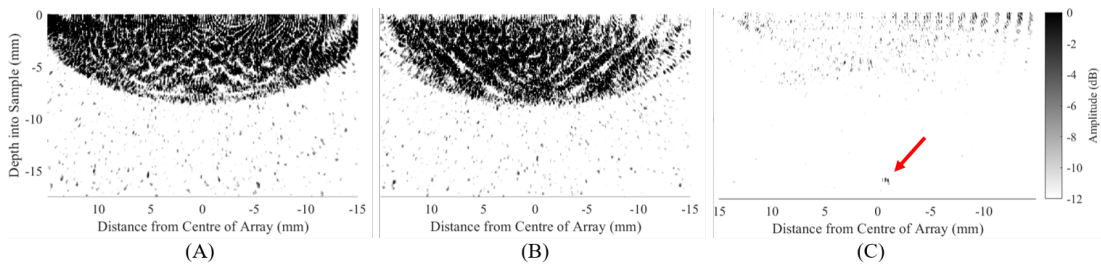


Figure 5.15: Ultrasonic TFM images produced by iterations 1 (A), 2 (B) and 3 (C) of SMC stage 1. The three arrays consisted of 10, 15 and 30 elements and 3, 2 and 1 mm inter-element spacing for iterations 1, 2 and 3, respectively. Digital filtering was applied at 5.5 MHz centre frequency, with a 100 % bandwidth. The location of the defect is emphasised by a red arrow.

production of this plot, in order to achieve a more consistent evaluation method, and reduce the effects of random fluctuations of the pixel values. A significant agreement is observed between the pixel intensity distributions for iterations 1 and 2, with both peaks of the two Rayleigh curves occurring at the same intensity bin. In contrast, a considerable shift can be detected in the Rayleigh distribution of the third image (curve shown in yellow in Fig. 5.16), where the peak occurs 11 dB lower than the peaks from the previous two iterations. The threshold set for the Rayleigh noise distribution was set to a 6 dB shift for this work, thus the Rayleigh curve produced by the third image is sufficient to trigger the defect detection algorithm.

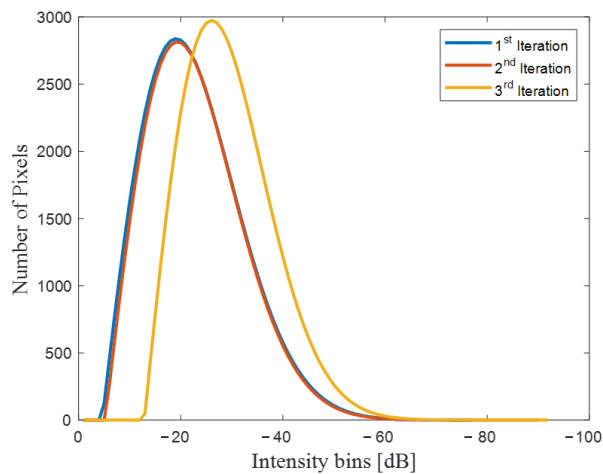


Figure 5.16: Pixel intensity distribution of images produced by the three iterations of stage 1 shown in Fig. 5.15, after Rayleigh curve fitting.

Overall, a total of 1225 A scan signals were acquired during the three iterations, requiring a total scan time of 82 seconds, while providing information regarding the location of the defect. Based on this information of the defect location the optimised array parameters (stage 2) were calculated as described previously in this chapter. For the threshold method (Subsection 5.3.1), -6 dB (i.e.: 50 % drop in directivity or detection sensitivity patterns) was selected as the limit. This provided two apertures of 3.41 mm wide each. An inter-element spacing of 0.155 mm was selected both in transmission and reception, in order to satisfy the Nyquist sampling theorem up to 10 MHz, leading to a total array element count of 46.

The alternative optimisation method, using Sensitivity-based Element Distribution (Subsection 5.3.2), was utilised to design an array containing the same number of elements as the threshold method. The 46 generation and 46 detection elements were spread over the total aperture of 30 mm, based on the directivity and detection sensitivity patterns, similarly to the designs shown on Fig. 5.13. Finally, a sub-sampled version of the dense FMC data-set was processed, by selecting 46 equally spaced elements of the dense array in order to compare the FMC acquisition method with a comparable number of array elements as the two optimised SMC arrays. For simplicity, this array is termed Sub-FMC for the remainder of this chapter. Thus, four arrays were produced in total utilising the following configurations, named after the data acquisition method required for each: 1) dense FMC, 2) sub-sampled FMC (Sub-FMC) (4.2 times Nyquist spacing), 3) SMC using the threshold method (SMC) and SMC using the Sensitivity-based Element Distribution method (SMC-SED). The four TFM images produced can be seen on Fig. 5.17. The array parameters are summarised in Table 5.1. For image processing, digital filtering was performed using a Gaussian shape, at 7 MHz centre frequency, with a 200 % bandwidth, and VCF weighting was applied to the images in post-processing.

The defect can be clearly identified on every TFM image at ~ 15 mm depth and horizontally at the centre, however a clear distinction can be made between the SNR of the four images quantitatively and qualitatively. The quantitative results, which were measured by comparing the noise floor away from the SAW regions and the defect to

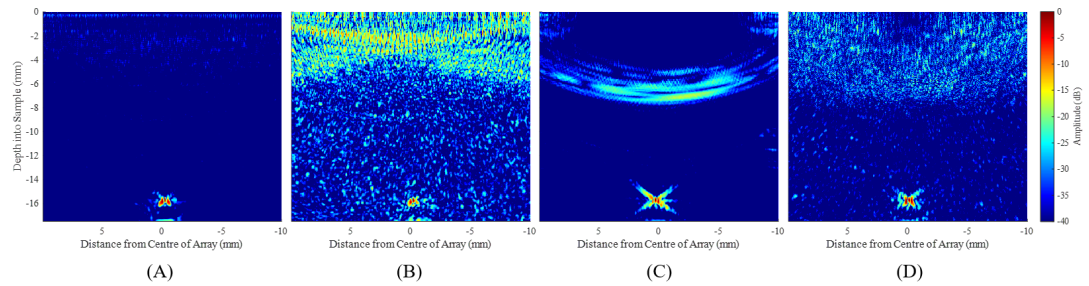


Figure 5.17: Ultrasonic TFM images produced by array configurations requiring: the FMC (A), sub-sampled FMC (B), SMC by threshold method (C) and SMC by Sensitivity-based Element Distribution (D) acquisition methods. Digital filtering was applied at 7 MHz centre frequency and 200 % bandwidth. The dynamic range used in all images is indicated on the right.

the highest defect amplitude (i.e.: 0 dB), are summarised in Table 5.1. The highest SNR was achieved by the array optimised according to the SMC threshold method (Fig. 5.17 (C)), providing an even higher SNR than the dense array utilising FMC acquisition (Fig. 5.17 (A)), despite using 17.6 times less data. The improved SNR for this array is explained by the fact that a significant number of signals in the Full Matrix (Fig. 5.17 (A)) contribute only to noise because the sensitivity is sufficiently low for these array element locations. The optimised SMC array did not capture these signals thus the image has a slightly higher SNR. In comparison, the Sensitivity-based Element Distribution (Fig. 5.17 (D)), shows a 15 dB reduction in SNR compared to the FMC and the threshold SMC method. This was expected because in this array configuration the same number of elements are used as the threshold method however now they are spread over the entire scan region, placing multiple elements in lower sensitivity regions. It is important to note here that both implementations of SMC offered significant improvements over the conventional FMC acquisition strategy with the same number of signals captured (Fig. 5.17 (B)), as this method does not perform any optimisation with respect to the laser ultrasound directivity and detection sensitivity patterns, and the sparsity of the array produces grating lobe artefacts.

Stage 2 of the SMC is aimed at providing high quality images for defect characterisation. The TFM images shown in Fig. 5.17 were sufficient to assess the SNR, however to assess the defect shapes, smaller pixel sizes are required. Further analysis

of the results is performed by using high resolution TFM image close-ups, which were processed around the location of the defect. The results can be seen on Fig. 5.18. Note that a different dynamic range was utilised in Fig. 5.17 in order to highlight the differences in SNR.

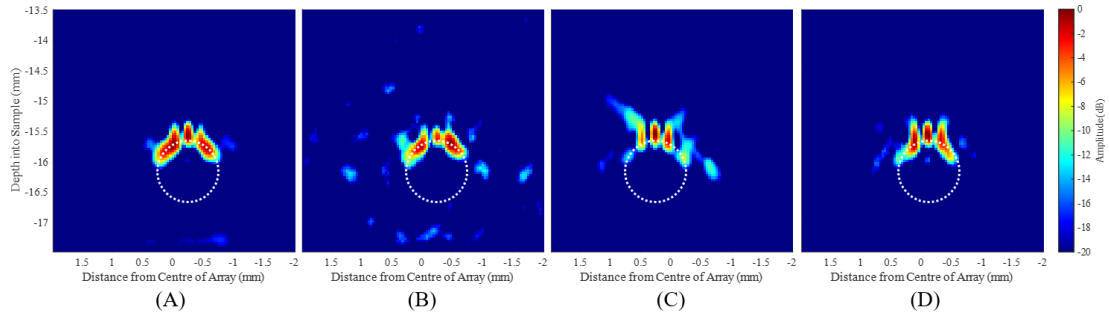


Figure 5.18: Close-up TFM images of the defect, using the same data-sets and post processing conditions as in Fig. 5.17. The dynamic range is shown on the right. White dash-circle indicates the location, shape and size of the defect.

Generally, a good agreement can be observed between the images and the location of the defect. However the image produced by the array using the SMC based on the threshold method (Fig. 5.18 (C)), shows a deterioration. This can be explained by the fact that the number of angles the defect is viewed from in this configuration is considerably restricted to the other array designs shown in Fig. 5.18 (A), (B) and (D). In Fig. 5.18 (C) the defect is only viewed from the angles optimal for generation and detection efficiency (i.e.: $\sim 25\text{-}35$ degrees for generation and $\sim 30\text{-}40$ degrees for detection).

The defect that was imaged in this chapter was a circular shaped side drilled hole of 1 mm diam. (See Fig. 5.14). Quantitative characterisation of such defects (i.e.: circular features) is currently significantly challenging in the field of NDE, requiring complex methods to evaluate circular sizing [50,51,84]. For this reason, only qualitative evaluation of the defect is discussed here. The array optimised by the Sensitivity-based Element Distribution (Fig. 5.18 (D)) achieves a comparable image shape to the fully populated, FMC array (Fig. 5.18 (A)), which is using 17.6 times more data.

These results demonstrate that the two optimised SMC methods are able to achieve comparable results to the FMC acquisition, while using 17.6 times less data and only

	Array Parameters			Imaging performance
	Number of signals	Pitch	Scan time	SNR
FMC	37249	0.155 mm	42 mins	65.92 dB
Sub-FMC	2116	0.650 mm	2.5 min	40.46 dB
SMC	2116	0.155 mm	2.5 min	65.93 dB
SMC-SED	2116	varying	2.5 min	50.44 dB

Table 5.1: Parameters and the respective imaging performance of the arrays requiring: FMC acquisition (FMC), sub-sampled FMC acquisition (Sub-FMC), SMC acquisition utilising the threshold method (SMC) and SMC acquisition utilising the Sensitivity-based Element Distribution (SMC-SED).

taking 2.5 minutes to perform data collection compared to 42 min for the FMC. Even if the acquisition time of the defect location stage (stage 1) is taken into account (82 seconds in the experimentally demonstrated case) the total, combined time for stages 1 and 2 of the SMC is 3.9 minutes. In comparison, ~ 11 times faster data acquisition was achieved, when compared to the 42 minutes total scan time of the dense FMC acquisition method, while achieving either equal levels of SNR or TFM imaging quality for defect characterisation.

In the above shown case, the defect was located in an area of overall good sensitivity with the given scanned LIPA aperture. In a different inspection scenario, the scanning region may be restricted due to limitations such as the component size or presence of other geometrical features. In order to demonstrate the technique in a more challenging scenario, the LIPA scan region was restricted, in a manner that the defect is horizontally offset by 4 mm from the line defined by the centre of the array. This results in a reduction in overall sensitivity for this specific location. After the restriction was placed, the total scan region was set to be 22 mm (See Fig. 5.14).

For this case the SMC data acquisition method was followed as described in the previous demonstration of stage 1, with the larger LIPA scan region. Three iterations were processed in total, as part of stage 1 of SMC. Each iterations was designed using

the same number of elements as in the case, as in the previous case: 10, 15 and 30 elements for iterations 1, 2 and 3, respectively. The inter-element spacing used for each iteration was 2.25, 1.5 and 0.75 mm, respectively, which was generally smaller than the case described earlier in this section, due to the reduced total LIPA scan region in this case. The digital filtering centred at 5.5 MHz with a 100% bandwidth was applied on each A scan signal.

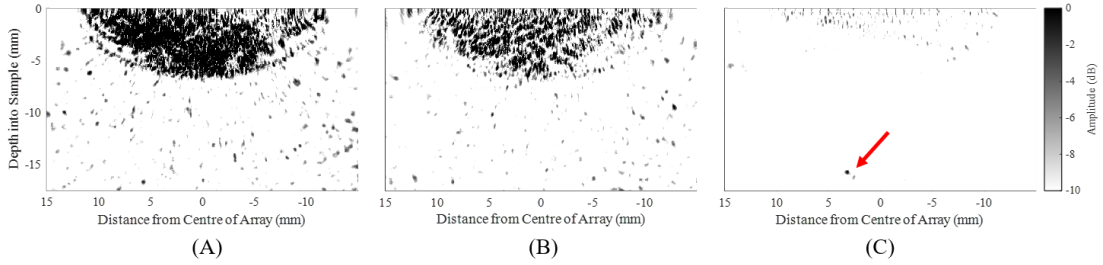


Figure 5.19: Ultrasonic TFM images produced by iterations 1 (A), 2 (B) and 3 (C) of SMC stage 1, with the limited scan region. Digital filtering was applied at 5.5 MHz centre frequency, with a 100 % bandwidth. For each image, VCF weighting was applied. The location of the defect is emphasised by a red arrow.

The defect cannot be visibly detected above the noise on TFM images produced during iterations 1 and 2. However it can be clearly detected on the TFM image produced by iteration 3. The distributions on the three TFM images can be seen on Fig. 5.20, after applying Rayleigh curve fitting. The Rayleigh curves from iterations 1 and 2 reach their maximum values within a difference of 1 dB from each other, whereas the peak for iteration 3 is offset by 11 dB compared to the other two curves, validating the detection of the defect, as per the 6 dB threshold for the Rayleigh curve defined in the previous case.

The two location-optimised SMC arrays (SMC and SMC-SED as defined earlier in this section) were configured using the location of the defect extracted from stage 1. They were then experimentally synthesised and their TFM images were compared to the dense array utilising FMC acquisition, and the sub-sampled version of it, using the same number of array elements as the optimised SMC arrays. The inter-element spacing for the dense array was again designed to fulfil the Nyquist sampling limit up to 10 MHz, thus was selected to be 0.155 mm. The total number of array elements was

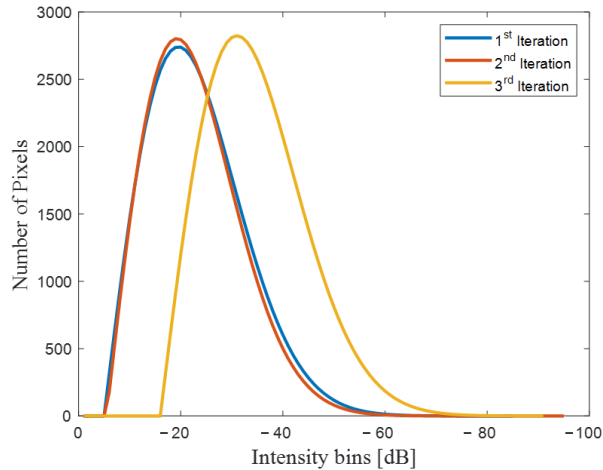


Figure 5.20: Pixel intensity distribution of TFM images produced by the three iterations of stage 1, after Rayleigh curve fitting, utilising the limited scan region.

142, compared to 193 of the previous case earlier in this section, due to the imposed limitations in the LIPA aperture. This led to a ratio of $R = 193:142 = 1.36$ between the number of array elements used in each case. During the SMC optimisation process, the array pitch was not matched to the pitch of the dense FMC array, instead the number of elements of the optimised SMC array was reduced by the same ratio ($R=1.36$) as the ration in the dense FMC array, thus the previous SMC array consisting of 46 elements was reduced to 34 for this case. In the case examined here, only one aperture was synthesised, after applying the 50% threshold, as shown on Fig. 5.11 (B). Consequently the inter-element spacing for array utilising the threshold based SMC optimisation, was 0.103 mm. The resulting images using the four acquisition strategies can be viewed on Fig. 5.21.

The comparison of SNR results observed in the produced images and information on LIPA parameters are shown on Table 5.2. Comparison of these results with those in Table 5.1 shows similar levels of SNR improvement for the SMC array configurations. However in this case, the LIPA optimised based on the SMC method achieved 6 dB SNR improvement over the dense LIPA requiring FMC acquisition, in spite of acquiring ~ 17.5 times less data. Translating this to linear values, the SNR improved by 100% by optimising the array element positions with respect to the defect location. The SMC-

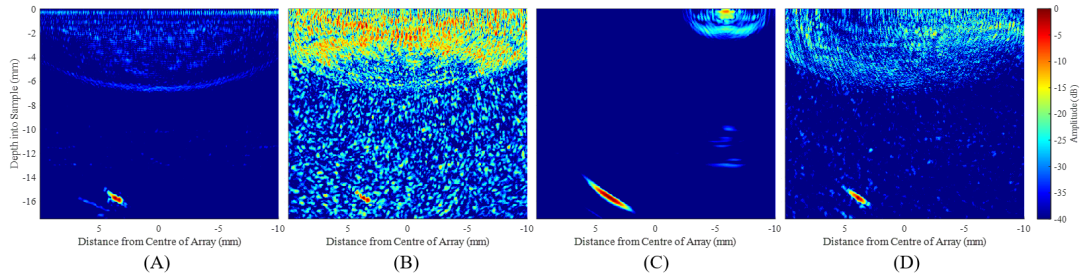


Figure 5.21: Ultrasonic TFM images produced by array configurations requiring: FMC (A), sub-sampled FMC (B), SMC by threshold method (C) and SMC by Sensitivity-based Element Distribution (D) acquisition methods, in the case of the limited LIPA scan region. Digital filtering was applied at 7 MHz centre frequency and 200 % bandwidth. Furthermore VCF weighting was applied to the images in post-processing. The dynamic range for all images is shown on the right.

SED, offers reduced SNR compared to the dense FMC array, however when compared to an FMC acquisition method using the same number of array elements, it achieves an SNR improvement of 16 dB, translating to a linear improvement of 530%.

In order to analyse the results better and extract qualitative information with respect to defect characterisation, high resolution TFM image close-ups were processed around the location of the defect. These are shown in Fig. 5.22.

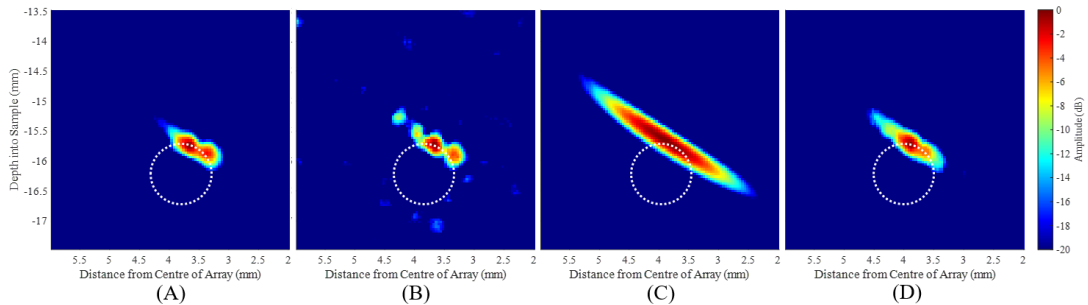


Figure 5.22: Close-up TFM images of the defect, using the same data-sets and post processing conditions as in images from Fig. 5.17, for the case of limited LIPA scan region. The dynamic range is shown on the right. White dash-circle indicates the location, shape and size of the defect.

The defects in this case are resolved mostly from the top-right segment of the circle on the images, due to its location relative to the centre of the array. In general, comparable images are produced by the dense FMC, the sub-sampled FMC and the

SMC-SED acquisition methods. The SMC acquisition utilising the threshold method achieves lower focusing, due to the limited inspection angles achieved by the small aperture relative to the other arrays, similar to what was discussed earlier in this section in relation to Fig. 5.18. In the case of the limited LIPA scan region discussed here, the angles are even more limited than in the previous case (angles are limited to one peak of the surface projected sensitivity), thus even higher distortion can be observed on the image.

	Array Parameters			Imaging performance
	Number of signals	Pitch	Scan time	SNR
FMC	20164	0.155 mm	23 mins	63.72 dB
Sub-FMC	1156	0.650 mm	1.3 min	36.52 dB
SMC	1156	0.103 mm	1.3 min	69.96 dB
SMC-SED	1156	varying	1.3 min	52.28 dB

Table 5.2: Array parameters and the respective imaging performance, of the FMC acquisition (FMC), sub-sampled FMC acquisition (Sub-FMC), SMC utilising the threshold method (SMC) and SMC utilising the Sensitivity-based Element Distribution (SMC-SED), utilising the limited scan region.

5.5 Summary

This work delves into the questions of whether the high quality of TFM imaging can be justified, when it requires the highly inefficient, and hardware demanding acquisition method of FMC. In order to address this issue, the work presented in this chapter proposes a new paradigm for ultrasonic imaging, with efficiency at its core. Currently, the same hardware (transducer-based phased array) is utilised for multiple experimental setups and inspection requirements, regardless of whether the parameters of the hardware are optimal for that setup or inspection, due to the rigid nature of ultrasonic transducers.

In this chapter the concept of adaptive acquisition method for ultrasonic phased

arrays was presented, the aim of which is to develop an infrastructure for ultrasonic imaging, that is able to optimise its hardware parameters to the needs of the inspection at hand. The reconfigurability of LIPAs was exploited in order to achieve the arbitrary locations calculated by the optimisation method. The SMC data acquisition method itself consists of two stages: 1) an initial rapid stage that provides sufficient information regarding the presence and location of defects, while providing low quality images and 2) a focused scan, where array parameters are optimised based on the location of the defect. Two alternative approaches were proposed for the second, optimised stage, one resulting in an array with equidistant pitch, with elements located to achieve highest generation and detection efficiency, while the other technique, named SMC-SED, utilised the entire scan region with the element density defined by the generation and detection efficiency.

The experimental results demonstrated that by optimising the array elements, comparable quality to what the FMC acquisition can provide, was achieved, while acquisition speed and data volume were reduced by an order of magnitude. Utilising the SMC threshold method, an SNR identical to, or 6 dB higher was achieved, compared to using the conventional FMC acquisition method, where information is acquired uniformly, regardless of the quality of information that can be acquired. The improvement in SNR was achieved even though the SMC optimised array acquired 17 times less data than the conventional dense array requiring FMC.

Regarding defect characterisation, the SMC threshold optimisation method distorted the shape of the defect on the ultrasonic images, which was a significant compromise between the improvement of SNR offered by this array configuration. This could impact decision making when assessing defects in an NDE setting. Without further improvements, this technique is more suitable for optimising SNR rather than defect characterisation.

On the other hand, the alternative optimisation method, SMC-SED, was able to achieve imaging without exhibiting defect shape distortion, reaching SNR of ~ 15 and ~ 11 dB lower than the dense LIPA requiring FMC, while achieving reduction by ~ 10.7 times for data volume and data acquisition time compared to the FMC LIPA.

The two optimised arrays were also compared to a sub-sampled FMC acquisition method. The number of elements of this array was selected such that the same number of A scan signals are captured as compared to the two arrays optimised by the SMC approach. Overall the SMC threshold method and the SMC-SED method achieved an improvement of 25 and 10 dB respectively for the case of LIPA inspection without scan limitations and 33 and 16 dB improvement for the case of LIPA with scan region limitation. These results validate the adaptive acquisition method, proving that by prioritising the acquisition of information-rich signals, an efficient phased array method is achieved that provides high quality imaging, with the minimal number of A scan signals.

In this work, the adaptive acquisition was utilised to achieve optimal SNR and defect resolving ability, however adapting this technique to other inspection requirements, the optimisation can be applied to a wide range of criteria, such as optimisation for axial or lateral resolution, reduced side-lobe levels, etc. This technique has the potential to address a variety of challenges in NDE which require remote, fast ultrasonic inspection reaching high frame rate imaging and reduction of data-sizes. Examples include inspection of large components such as rail inspection [85], inspection of aeroplane wings or wind-turbines, where the need to capture multiple FMC data-sets can exceed data size of terabytes [70].

Furthermore, this work concentrated on establishing the basic principles of adaptive data acquisition. Future developments, in terms of data processing could eliminate the drawbacks of the current technique. For example the threshold-based optimised array was able to inspect the defect from only a limited number of angles, leading to deterioration of the defect shape on the ultrasonic TFM imaging. Previously, a technique has been demonstrated that is able to infill data for a sparse array to suppress grating lobes, utilising a deep neural network [86]. This technique could be adapted for the array produced by the SMC optimisation method, in post-processing, in order to synthetically infill the data at a wider range of inspection angles. This could lead to improving the SMC method towards achieving identical SNR as well as identical defect resolving ability as compared to the conventional method acquiring significantly more

data.

Finally, a defect detection framework was proposed in this chapter. This technique offered a way for defect detection by analysing the distribution of pixel intensities of an ultrasonic image and observing the peak of the Rayleigh distribution produce by the noise floor. Thereby this method could be an effective tool for automation of NDE, which has been pinpointed as a high priority goal for future developments for NDE, by various researchers [53, 79]. The threshold set for the Rayleigh noise distribution was set arbitrarily to a fixed number (i.e.: 6 dB shift) for the research presented in this Thesis. In practice, studies must be carried out in order to establishe suitable values for this threshold for the given materials and types of defects that may be present.

Chapter 6

Volumetric Imaging for 2D Laser Induced Phased Arrays

Real physical objects, as well as the defects within them, are three dimensional. Trying to evaluate their integrity through cross-sectional ultrasound images can be misleading of the shape and size of internal features. Three-dimensional, volumetric imaging is necessary to provide accurate assessment and representative inspection of the test object.

This work presents the first experimental implementation of a laser ultrasonic imaging system for NDE that can synthesise reconfigurable 2D LIPA designs, operates remotely and can produce volumetric ultrasonic images using the TFM algorithm. This is enabled by employing the FMC data acquisition method, which captures all the possible information relative to the array position. This is achieved via scanning the generation and detection lasers independently of each other. The unique advantages of this system are:

- a wide range of post-processing imaging algorithms [50, 51, 67, 87] can be used, of which the Total Focusing Method and Phase Coherence Imaging are utilised in this work. This is enabled by the Full Matrix Capture data acquisition method.
- LIPA elements can be rearranged with any arbitrary layout including optimised sparse array designs and designs with overlapping elements and decoupled gener-

ation and detection layouts. This is due to the reconfigurability of LIPAs and the small footprint of the array elements, defined by the laser spot size. As a result, optimised arrays can be synthesised, tailored to the component under inspection.

As all the generation and detection element combinations are acquired, ultrasonic waves view the defects from a wide range of angles, providing information about their shape. This is particularly important for detecting scatterers/defects that do not scatter ultrasound uniformly in all directions (e.g.: planar defects) [88]. Imaging of such scatterers can be challenging for algorithms such as the SAFT and the C-scan as their imaging capabilities depend on defect shape and orientation [50]. Finally, rapid 2D array prototyping capability is demonstrated experimentally in this chapter by synthesising various array designs, using the same experimental setup, which would be challenging or impossible to achieve with transducer based phased arrays due to the manufacturing cost and hardware limitations (e.g. element size and/or overlapping elements).

Previous implementations of 3D laser ultrasound imaging are very few in the literature [41, 43, 46–48, 89]. All of these studies have captured only the data necessary for implementing either the SAFT or C-scan imaging algorithms with either coincidental [41, 47] or offset generation and detection beams [46, 48]. The most recent of these studies [48] produced 3D images by stacking multiple cross-sectional 2D images, thus this method did not achieve focusing parallel to the plane of imaging, thereby it is not suitable for accurate volumetric imaging in all planes, as demonstrated by McKee [13]. The only reconfigurable laser induced array previously presented is by Alles et al [46] who used an optical fibre bundle for ultrasonic generation and a single, stationary ultrasonic detection position in water-immersion. The present study expands on the concept introduced in this previous work by extending the flexibility of the synthesised array using FMC and remote delivery, which allow arbitrary 2D array designs. As the lasers are not coupled by optics fibres, and the generation and detection lasers are scanned independently of each other five distinct advantages are presented: 1) multiple elements can partially overlap, 2) the elements are not limited to a discretised layout, 3) different layouts can be produced for generation and detection, 4) the array element

location and array configuration can change during data acquisition (on-the-fly), based on information from the previously acquired data and 5) the ability to synthesise an array with any arbitrary aperture size.

A critical challenge of volumetric imaging is posed by the requirement of a considerable number of array elements in order to probe large volumes of an object, while satisfies the Nyquist sampling limit. To address this problem many researchers have been exploring spatially under-sampled array designs towards suppression of grating lobes [14, 90–93]. For Laser Induced Phased Arrays this problem is exaggerated by the requirement of slow mechanical scanning of the lasers, as well as the inability to detect multiple signal in parallel. In this work, for the first time, sparse 2D LIPA designs for grating lobe suppression are explored in order to address the previous LIPA shortcomings, towards faster, more efficient, remote volumetric ultrasonic imaging.

Furthermore, transducer-based phased array manufacturing is a costly and time-consuming process. Researchers rely on analytical models, or simulation for array optimisation, only fabricating the design with the highest theoretical performance [91, 92, 94]. The system described in this Thesis is capable of experimentally synthesising a phased array with any arbitrary layout with the possibility to achieve different designs for transmission and reception, due to the decoupled generation and detection lasers. This reconfigurability provides a unique infrastructure for experimental optimisation of 2D ultrasonic phased array designs.

Currently possible phased array designs are restricted due to geometrical limitations. The physical size of the array elements limit their location, as well as the possibility of partial overlapping. For example Ramadas et al. [91] have presented phased array layouts based on their optimisation method, that are not feasible to achieve using transducers due to the need for overlapping elements. The remote, 3D ultrasonic imaging system developed in this work, uses light for synthesising the array, thus the technique challenges the current paradigm of ultrasonic 2D arrays. The ability to synthesise any arbitrary layout with differing generation and detection arrays, with overlapping elements, significantly widens the range of possible 2D phased array designs. Fig. 6.1 shows an example 2D array design that is impossible to make using

transducers due to the overlapping elements. The LIPA is the first technique that can enable such phased array design. This capability can be exploited to propose novel array design concepts to further improve the capabilities of 2D phased arrays.

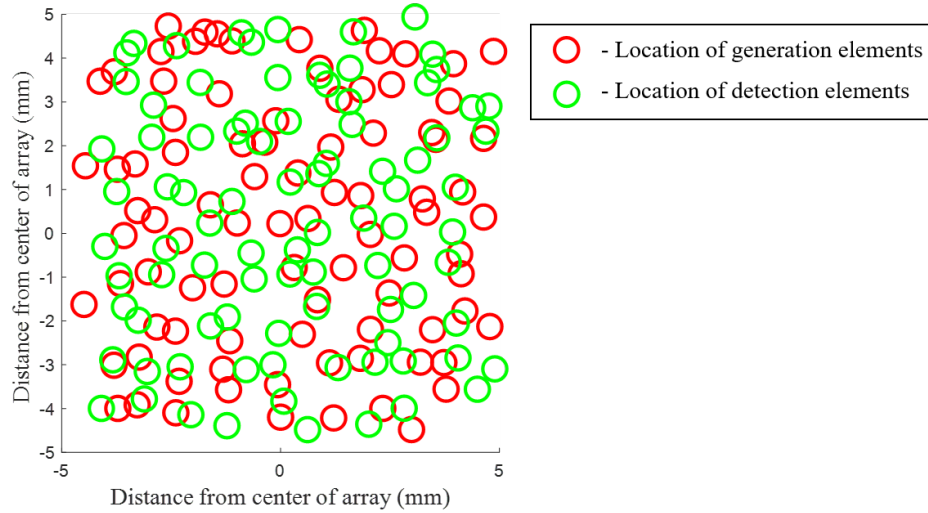


Figure 6.1: Diagram of a 2D ultrasonic phased array design enabled by the system developed in this work.

6.1 Adapting to the Third Dimension

Commonly the Total Focusing Method is used to produce cross-sectional 2D images, however it can be equally utilised for three dimensional (3D) imaging of the volume. Volumetric images require both an instrument capable of scanning in 2D as well as adapting the post-processing algorithm for 3D. The current section aims at addressing changes while progressing from 2D to 3D imaging, considering the requirements of laser generated and detected ultrasound, in order to enable 3D laser ultrasonic images.

6.1.1 Data Acquisition and Processing

3D imaging requires a system capable of generating and detecting ultrasound along a plane rather than along a 1D linear arrangement. The simplest approach to producing volumetric imaging is to synthesise multiple linear arrays parallel to each other and producing multiple slices of the test object until the entire volume is imaged, as demon-

strated in [48]. This approach, however only enables beam forming (i.e.: focusing and steering) parallel to the array, while it is not achieved normal to the array. In [13], McKee has demonstrated that due to this lack of focusing normal to the array, imaging by slices produces significantly lower image quality, with defects being distorted, when compared to using a 2D array, which is capable of beam steering and focusing in 3D. Thus this approach is not suitable for 3D defect characterisation.

In order to populate the Full Matrix, and acquire all the possible information that can be captured from a single position of the array, every generation and detection element combinations must be acquired. LIPAs can synthesise any arbitrary array layout, and have the capability to produce a different layout for generation and detection due to the decoupled generating and detecting lasers. In this work different array designs are presented to improve imaging capabilities. Regardless of the design, a signal is captured for each generation and detection element combination, to ensure the highest possible imaging quality.

Processing the data produced by a 2D array, the TFM algorithm must be extended to include, ray-tracing in volume, in order to calculate the correct delay-laws for each voxel. A voxel is the 3D equivalent of a pixel, and each of them have an x,y and z coordinate. The correct delay laws are found by calculating the distance between the generating element and the voxel, and the distance between the detecting element and the voxel, as shown in Fig. 6.2. While the algorithm to calculate the voxel intensities is the same in the 3D case as in the 2D case (i.e.: Eq. 3.6), equations 3.7 and 3.8 take the following form, respectively:

$$d_{tx} = \sqrt{(x_{tx} - x)^2 + (y_{tx} - y)^2 + z^2} \quad (6.1)$$

$$d_{rx} = \sqrt{(x_{rx} - x)^2 + (y_{rx} - y)^2 + z^2} \quad (6.2)$$

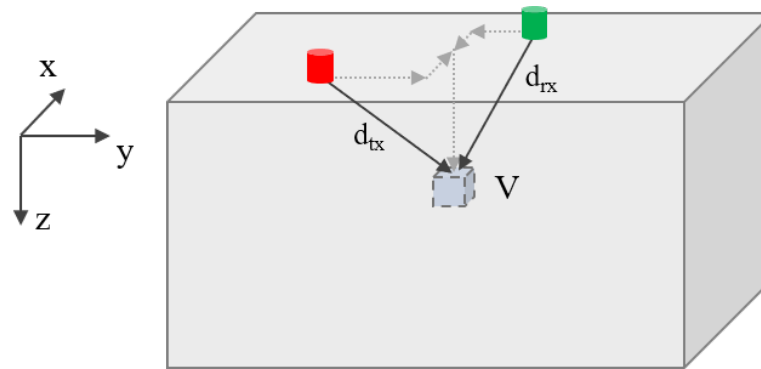


Figure 6.2: Visual demonstration of the distances between the elements and the voxels. Red and green cylinders show the position of the generation and detection laser beams.

6.1.2 Visualisation of Volumetric TFM Images

An important aspect of ultrasonic imaging is visualisation, with the goal of achieving images that are as easy to interpret as possible. In most cases for cross-sectional 2D imaging, this is relatively simple as the images are presented in a 3D plot with the three axes being the lateral distance, the axial distance and amplitude of the pixel at those distances or a 2D image that uses colour to display amplitude information.

In contrast, for imaging the volume of a test component, 4D data must be visualised, where the 4 axes are, width, length, height and the amplitude of each voxel. Applying the same visualisation technique, with each voxel exhibiting a colour correlated to its amplitude is not plausible for 3D imaging, as this would only visualise an “outer shell” of the sample. In this work two techniques for visualisation of volume are presented: Cross-sectional slicing and imaging using isosurfaces, which is a significantly more popular method.

In this case isosurfaces can be defined with a boundary between low and high amplitude regions, with the high amplitude implying a feature. Performing this process renders the regions only containing noise transparent revealing the inside and the internal features of the test object, as shown on Fig. 6.3.

The benefits of this technique include the ability to accurately resolve complex 3D features and to visualise the entire interior of the test object in one image. However, as the noise floor is not visible on these images, it can be difficult to evaluate contrast

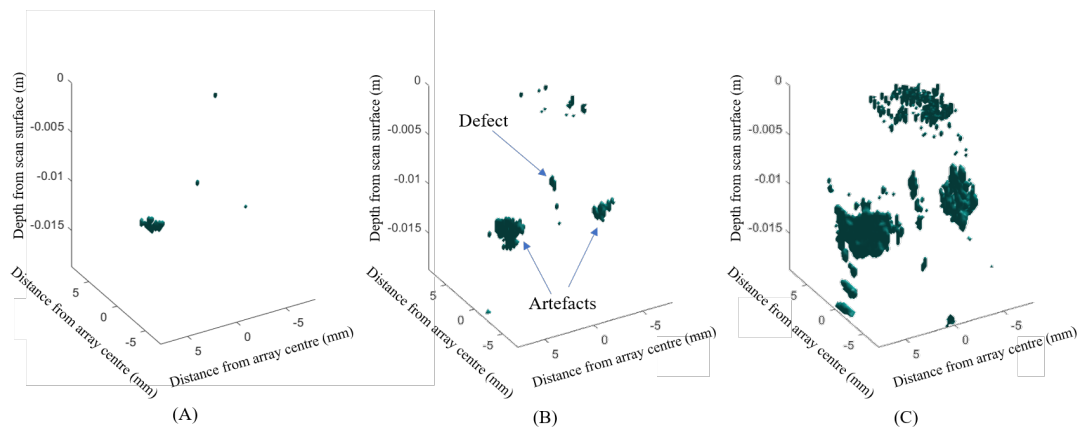


Figure 6.3: Isosurfaces, with boundaries defined at various thresholds: -3 dB (A), -6 dB (B) and -12 dB (C) relative to highest intensity pixel) with a single defect located at $[0, 0, -7.5]$ mm.

and measure SNR of the image. Furthermore, as the threshold is selected by the user, defects might not appear on the image depending on their amplitude relative to the highest amplitude defect, leading to a false negative decision when defect detection is performed. Conversely, high amplitude noise or artefacts might appear leading to false positive detection. Some of these problems are highlighted in Fig. 6.3: A false negative with respect to the real defect location would result in (A). Presence of artefacts would result in false positives in (B) and (C).

Cross-sectional imaging through slicing is an alternative method of visualising 4D matrices. This way one or multiple slices of the volume are imaged with relative distance and or angle between the slices. The individual slices each represent a section of the entire volume, plotted similar to that of a 2D image, that is each slice is plotted against 2 of the 3 dimensions of the volume and amplitude is represented as colour. Imaging entire slices of the volume enables simple evaluation of the noise floor and reduces the risk of false negative and false positive detection of defects. However, inspecting a volume through individual slices is significantly more time consuming, as well as complex features are challenging to evaluate and recognise when viewed slice by slice.

Comparison between the two methods detailed above can be seen in Fig. 6.4. The cross-sectional imaging has the advantage of showing amplitude with colours but will

fail in the case of asymmetric defects, as is a usual case in NDE (e.g. cracks, lack of fusion defects). The isosurface approach gives a better representation from a 360° angle but the colour represents every point above a certain amplitude threshold. For the purposes of this Thesis, the method using isosurfaces has been used throughout.

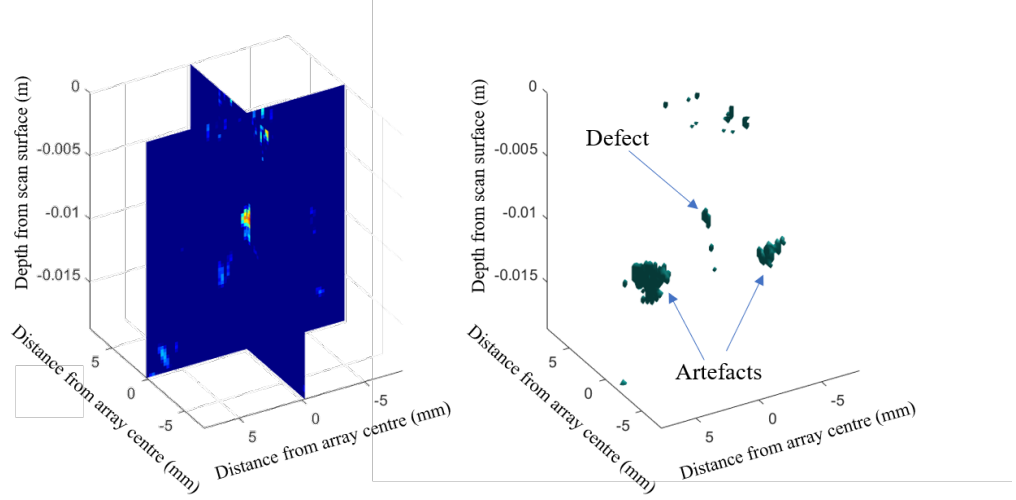


Figure 6.4: Comparison of the two visualisation tools: slices (left) and isosurfaces (right).

6.1.3 Sensitivity Maps

Sensitivity maps can be produced for 2D arrays, similar to the case of 1D arrays. As the post-processing, delay-and-sum algorithm was adapted to the 3rd dimension, the same process must be applied for calculating sensitivity maps. The equation presented for the 2D sensitivity map calculation applies for 3D sensitivity maps equally, however in this case, the angle between the centre of the elements and the voxels can be found by the following equations:

$$\theta_{tx} = \tan\left(\frac{\sqrt{(x_{tx} - x)^2 + (y_{tx} - y)^2}}{z}\right) \quad (6.3)$$

$$\theta_{rx} = \tan\left(\frac{\sqrt{(x_{rx} - x)^2 + (y_{rx} - y)^2}}{z}\right) \quad (6.4)$$

A critical aspect to consider for the sensitivity map calculations is the ultrasonic beam-spreading. For the 1D array case, the ultrasonic generation laser beam was focused into a line and ultrasonic line sources were excited, which produce cylindrical wave fronts. This ensured uniformity in the third dimension which results in ultrasonic beam spreading only occurring in two dimensions (i.e.: a cylinder with a continuously increasing diameter). Volumetric imaging however requires ultrasonic beam-forming in 3D. To reflect this, the the ultrasonic generation laser beam was focused into a circular spot and the ultrasonic generation source was changed to a point source as mentioned in Chapter 2. Ultrasonic beam spreading consequently occurs in all directions, due to the change in generation shape. This translates to the ultrasonic wavefront propagating as a sphere, compared to the cylindrical wavefront of a line source. To reflect this the ultrasonic beam spreading coefficient has been revised as follows:

$$B = \frac{1}{d_{tx}(x, z)d_{rx}(x, z)} \quad (6.5)$$

It then follows that, as beam spreading for a spherical wavefront has a linear relationship to the distance propagated, as opposed to a square root relationship in the case of cylindrical wavefront, the waves produced by a point source are expected to lose more energy as they propagate within the sample. An example of a sensitivity map of an array with 100 elements is shown on Fig. 6.5. The inter-element spacing of the array was 0.8 mm and three semi-transparent isosurfaces were produced for visualisation, at varying amplitude thresholds (-1, -3 and -5 dB), relative to the highest sensitivity (0 dB) voxel.

Compensation for blind spots and variation in ultrasonic sensitivity can be performed for 3D imaging, the same way it was detailed for cross-sectional imaging (see section 3.4). The sensitivity maps are used as weighting factors, amplifying low sensitivity regions resulting in an image with uniform sensitivity but non-uniform noise.

6.1.4 Ultrasonic Beam Forming in 3D

In order to evaluate the beam forming capabilities of 2D arrays, the model described in chapter 4.1, was developed for 3D space. In order to calculate the suitable delay-laws

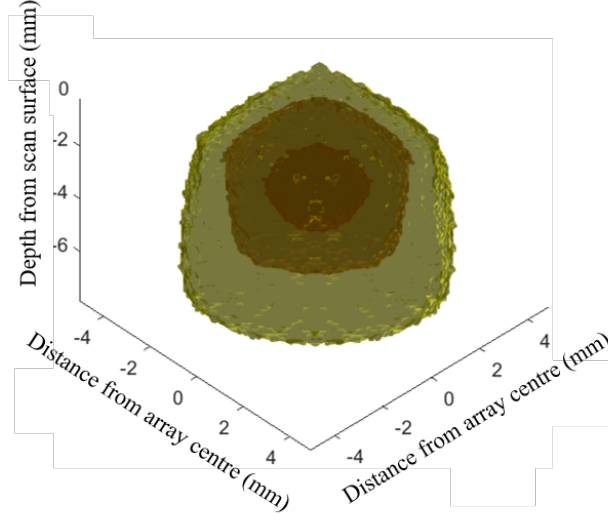


Figure 6.5: 3D Sensitivity map using semi-transparent isosurfaces. Smallest isosurface represent the voxels with sensitivity between 0 and -1 dB, middle between 0 and -3 dB and largest between 0 and -6 dB

for the desirable focusing the following equation is used:

$$t_j = \frac{\sqrt{(x_{tx} - x_f)^2 + (y_{tx} - y_f)^2 + (z_{tx} - z_f)^2} - \sqrt{x_f^2 + y_f^2 + z_f^2}}{c_{mode}} \quad (6.6)$$

Where, x_{tx} , y_{tx} and z_{tx} are the position of the generating element tx and x_f , y_f and z_f are the coordinates of the focal point. Value c_{mode} is the acoustic velocity of the selected mode.

Note that the delay-laws are calculated relative to an arbitrarily selected point within the aperture. The point is defined by the second square root in the numerator of Eq. 6.6. In this case the centre of the aperture was selected as the reference point, which provides the simplest implementation of the equation, as the distances to the focal point are calculated relative to the zero point. Finally, the delays are implemented as phase shifts, in order to calculate the pressure field, as demonstrated in Chapter 4:

$$P_{tx} = GB e^{i(k*\sqrt{(x_{tx}-x_f)^2+(y_{tx}-y_f)^2+(z_{tx}-z_f)^2}-2\pi ft_j)} \quad (6.7)$$

$$P_{rx} = DB e^{i(k*\sqrt{(x_{rx}-x_f)^2+(y_{rx}-y_f)^2+(z_{rx}-z_f)^2}-2\pi ft_j)} \quad (6.8)$$

Where, G and D are the generation and detection patterns, B is the beam spreading coefficient, k is the wavenumber (i.e.: $2\pi/\lambda$) and f is the frequency of the ultrasonic wave. The product of P_{tx} and P_{rx} then provides the calculation for the pressure field produced by focusing both in transmission and reception.

The results produced by this model can be visualised using the approaches detailed previously, Subsection 6.1.2. Previously the isosurface method was highlighted as a better overall method for the 3D imaging applications in question, however the case of ultrasonic beam forming includes additional considerations. This model is only suitable for estimating the lateral resolution (i.e.: main lobe width), side-lobe and grating lobe levels, which are estimated along a hemisphere centred to the centre of the array, at a radius defined by focusing. However plotting spherical objects on flat screens has its own challenges. A commonly used technique to tackle this challenge is to project the hemisphere onto a u-v plane, by the process of u-v mapping [95]. The elevation (θ) and azimuth (ϕ) angles can be converted to u-v space using the following equations:

$$u = \sin(\theta)\cos(\phi) \quad (6.9)$$

$$v = \sin(\theta)\sin(\phi) \quad (6.10)$$

Array directivities for 2D arrays will be plotted on u-v maps, utilising Eq. 6.9 and 6.10, for the remainder of the chapter.

6.2 2D Phased Array Designs

Satisfying the inter-element spacing requirement for 1D arrays can be achieved with relative ease for common imaging sizes. As an example, imaging within an aluminium sample ($\sim 3200/6300$ m/s – shear/longitudinal velocity) using acoustic waves at a 5 MHz centre frequency, would require an inter-element spacing of 0.32 and 0.63 mm for

shear and longitudinal waves respectively. Using these values for an aperture of 30 mm width, an element number of 96 and 48 would be sufficient to completely eliminate all grating lobes. Even for the shear imaging case the acquisition time with a LIPA would only take 13 min. In comparison for the same aperture size for a 2D array without producing grating lobes, a total element-count of 9216 (96×96) would be necessary. Using this array, the acquisition time would now be 8 days, 15 hours and 31 minutes, which is 950 times longer than the 2D imaging case. Thus, it is necessary to explore sparse 2D phased array designs that can achieve high quality imaging while suppressing grating lobe artefacts and have a realistic application potential.

In this sub-chapter, the concepts of sparse 1D LIPAs presented in Chapter 4 are advanced towards 2D arrays. The random and Vernier array layouts are compared to conventional matrix array designs.

6.2.1 Matrix Layout

Matrix arrays, sparse or dense, have the lowest design complexity. The layout of the array represents a matrix with equidistant adjacent elements. Furthermore, the array layout for ultrasonic generation is identical to the layout for ultrasonic detection. This design idea can be seen on Fig. 6.6.

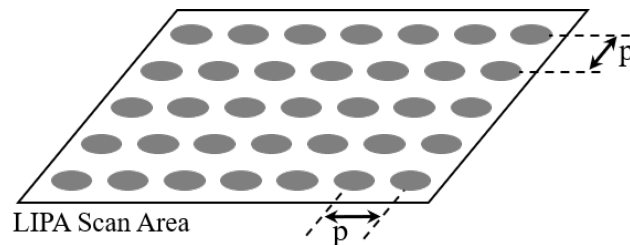


Figure 6.6: Angle view of a 25 element, 2D matrix array. Grey circles are the array elements, while p signifies the inter-element spacing.

6.2.2 Binned Random Array Layout

Binned random array layout utilises a randomised process of placing the array elements within a user-defined grid, as detailed in section 4.3. The maximum grating lobes levels

are reduced in spite of the spatial under sampling, as this array element distribution reduces the periodicity of the array. This improvement is achieved because the random layout spreads the energy of the grating lobes over the entire array directivity, unlike the matrix array where the grating lobes are concentrated at the aliasing angles. This array design has previously been shown to outperform a sparse matrix array with the same number of array elements [12,14]. Figure 6.7 shows the layout of an array with its elements located in a binned random layout.

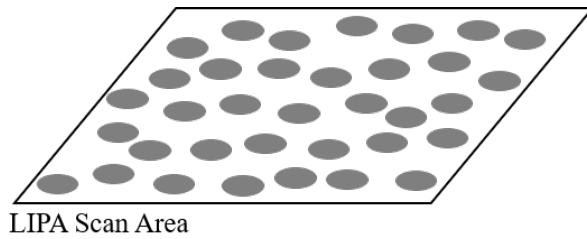


Figure 6.7: Array layout utilising binned random distribution. Grey circles are the array elements, with random inter-element spacing

While it is possible to use an entirely random array layout, it might not be efficient due to the possibility of too many elements ending up in close proximity, while leaving large sections of the aperture barren, which can compromise array performance [76]. The binned array distribution improves upon this by placing a limitation of minimum distance between two elements.

6.2.3 Two-way Radiation Pattern Optimisation - Vernier Array Layout

Two-way radiation optimisation, presented in section 4.2, can be extended for 2D arrays to reduce grating lobes for 3D imaging. Arrays that are designed this way are called Vernier arrays [90]. The generation and detection layouts differ, with each having a different number of elements and pitch (Fig. 6.8).

Similar to the 1D array case, the grating lobes for the two patterns appear at varying degrees on the array directivity, thus in the two-way radiation they cancel out. Due to the decoupled generation and detection of LIPAs, this technique can be very efficiently adapted.

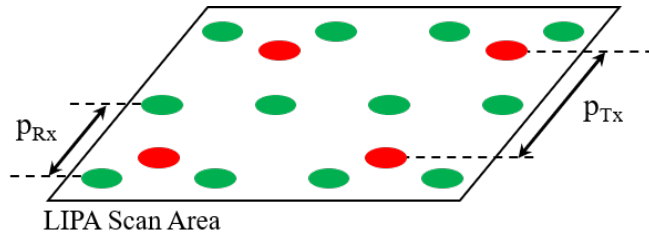


Figure 6.8: Vernier Array Layout. Generating (red circles) and detecting elements (green circles) are distributed in different patterns providing separate transmit and receive apertures, with inter element spacing of p_{tx} and p_{rx} , respectively, where $p_{tx} \neq p_{rx}$.

6.3 Adaptive Data Acquisition for Volumetric Imaging

The previous section introduced the concept of optimised sparse array designs as a way to reduce the number of array elements while suppressing grating lobes that would otherwise compromise imaging capabilities. These sparse arrays were based on optimising the spatial sampling points of the array considering the array directivity. However, this optimisation still does not consider laser ultrasonic array sensitivity. As demonstrated in chapter 5, depending on the position of a generating or detecting element, their directivity and sensitivity to a defect can vary. This is equally true for 2D arrays.

The aim of this section is to remove any elements from regions with no or low directivity or sensitivity, and concentrate all the elements within the LIPA scan region with highest generation and detection sensitivity for a particular region of interest, as it was presented in Chapter 5.

In Chapter 5, the technique was evaluated by comparing the results of the SMC scan to that of a dense FMC acquisition. The SMC array consisted of two stages: (1) initially a rapid iterative scan was performed which was followed by (2) an optimised scan based on the information obtained in the first stage. The iterative method, for 3D imaging however would require a significantly high number of elements to decisively detect the defect. For this reason an alternative approach of demonstrating adaptive acquisition is taken for volumetric imaging. The location of the defect is assumed to have been located already, by utilising a sparse array design presented in section 6.2. Then, using the concept of adaptive acquisition, a dense SMC array can be synthesised

with maximum array sensitivity for higher image quality. A significant advantage of this approach is that an array with pitch satisfying the Nyquist criterion is synthesised while concentrating all the elements within the region with highest directivity and sensitivity when compared to conventional acquisition methods. As a result, in addition to having optimised sensitivity, grating lobes are fully eliminated.

In order to find the optimal generation and detection positions in a 2D space (i.e.: LIPA scan surface) when the location of the defect is already known, the surface projected sensitivity and directivities are calculated. For cross-sectional imaging, these projections were 1D plots along the scan surface as shown on Fig. 5.8. For 3D imaging, the surface projection are 3D plots along the 2D scan area. Figure 6.9 shows the surface projected directivity on the scan surface for a defect located at a depth of 4 mm, assuming shear wave velocity of aluminium.

Conversely, longitudinal mode can be utilised to calculate the surface projections, by applying the directivity and sensitivity patterns of this mode. Furthermore mode-conversion can also be considered when a portion of the shear or longitudinal wave, incident on the reflector converts to the other wave mode. In this case shear directivity and longitudinal sensitivity patterns are considered or vice-versa. The four combined sensitivities of shear, longitudinal, shear-longitudinal and longitudinal-shear are presented on Fig. 6.10. Each projection was individually normalised to its highest amplitude.

Shear mode generation using laser ultrasound, generally has higher efficiency in metals at the thermoelastic regime compared to longitudinal wave modes, such as in aluminium where a difference of an order of magnitude can be observed [60]. For this reason only the shear mode is considered in this study. Furthermore, the mode-converted shear-longitudinal mode is also excluded in this work as approximately only 11.2% of a shear wave would mode-convert, leaving most of its energy (88.8%) in its original mode [96].

Based on the surface projected combined sensitivity, the optimal element positions can be calculated for the specific region of interest utilised for producing these projections. Similar to the 1D array approach, the simplest way is to apply a threshold on

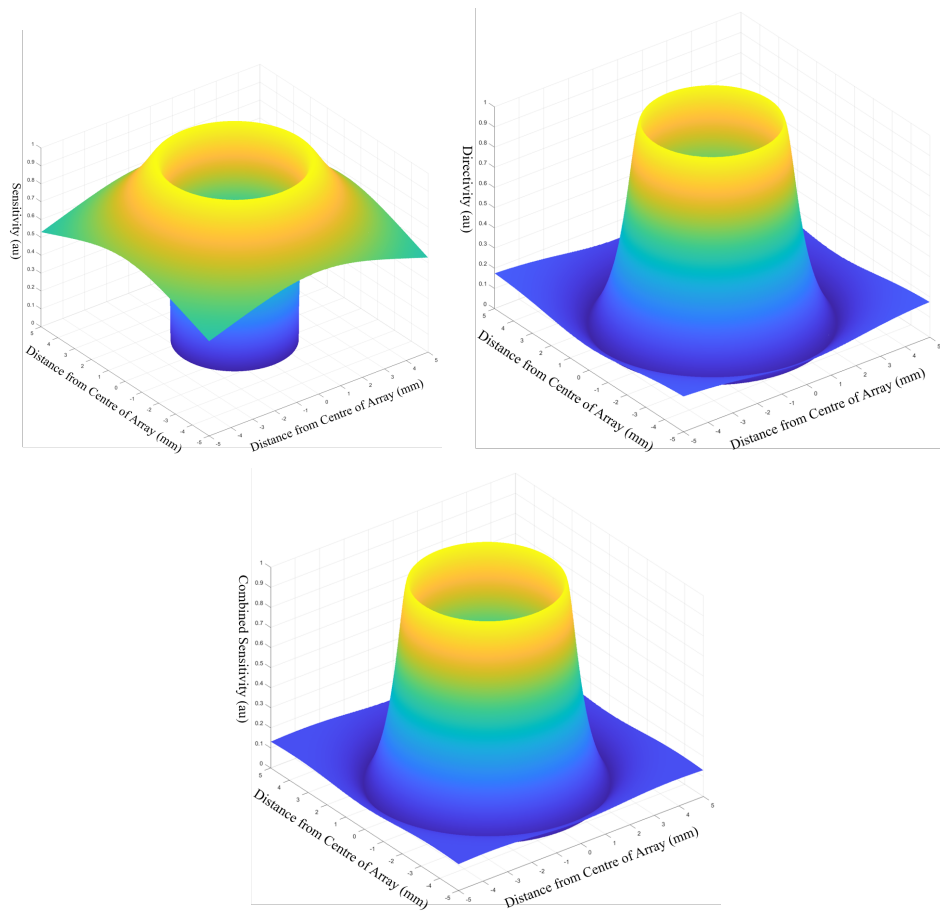


Figure 6.9: Volumetric figures of surface projected ultrasonic directivity (A) and sensitivity (B) for a 10 by 10 mm LIPA scan region, for a defect located at 4 mm deep, directly below the centre of the array. The two projections are combined through multiplication to provide a combined sensitivity (C).

to the projections. This process can be seen on Fig. 6.11. The region between the red dashed circles shows the array aperture after taking the combined array sensitivity within the -6dB from the highest value. This is emphasised in the middle figure by setting the values of pixels within this region to 1 (i.e.: yellow) and the rest of the scan region to 0 (i.e.: dark blue). Finally, the array produced within this region can be seen on the right hand-side of Fig. 6.11, where each dot represent an element of the array with a periodic layout.

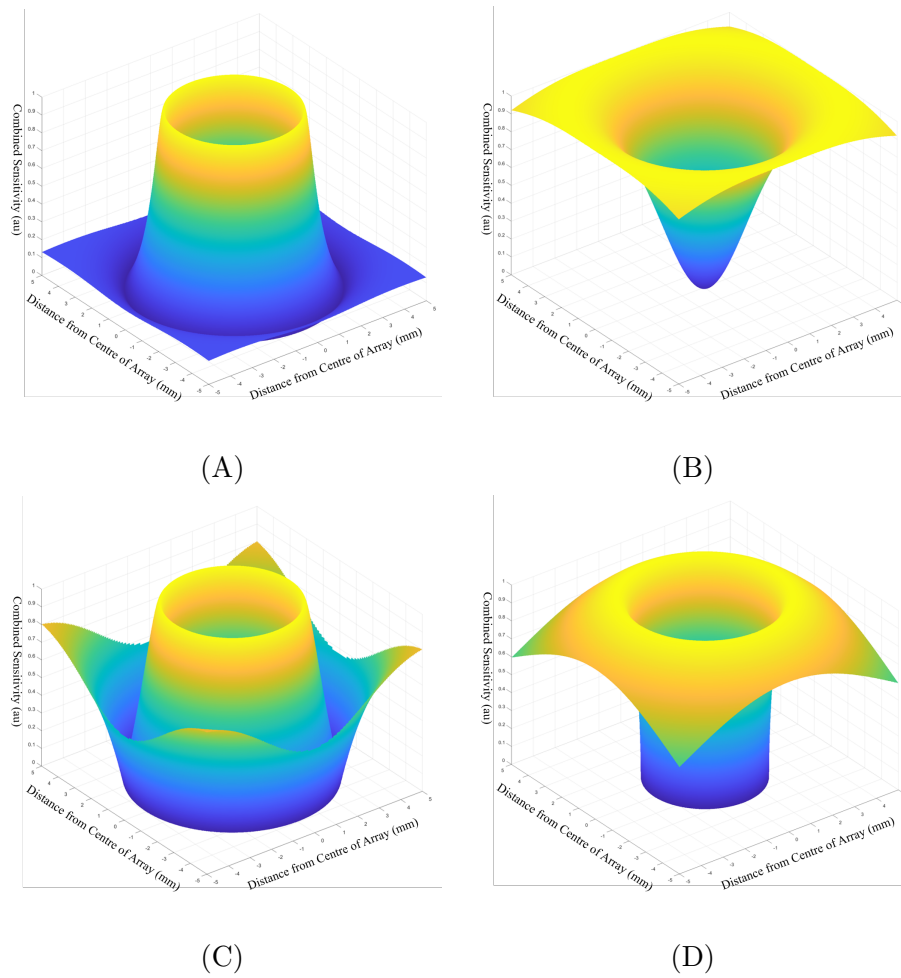


Figure 6.10: Normalised combined sensitivity for shear (A), longitudinal (B), shear-longitudinal (C) and longitudinal-shear (D) modes. Each figure was normalised to its respective maximum amplitude.

6.4 Experimental Results for Remote Volumetric Imaging

In this section the experimental results are presented for the concepts introduced so far in this chapter.

6.4.1 Volumetric Image Combinarion on an Additively Manufactured Component

The aperture of a phased array in certain cases is not large enough to inspect the entire test component, in which case image stitching can be employed [19]. This is achieved

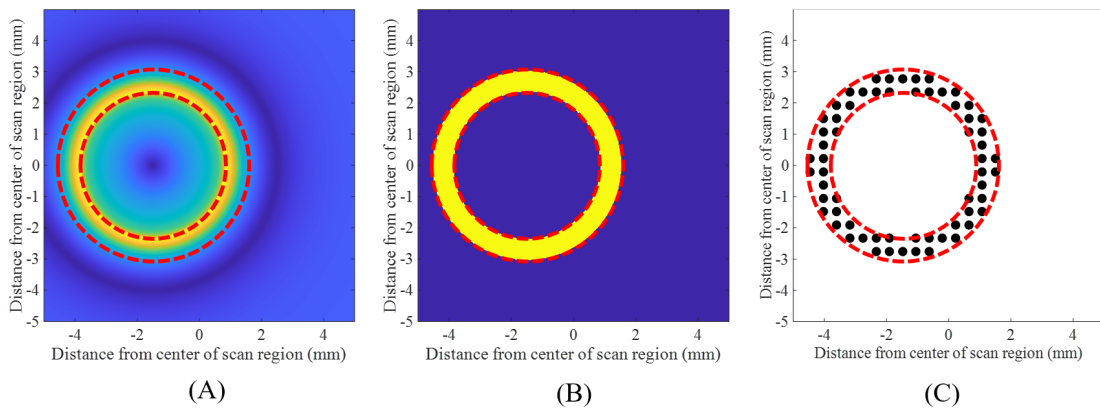


Figure 6.11: Calculation of optimum array layout based on surface projected sensitivity (A). Threshold at -6 dB drop from peak is defining the array bounds (B). Red dashed circles show the edges of the -6 dB drop, and black dots show the array elements (C).

by producing multiple images of the test sample with varying locations of the aperture, which are then stitched together to form a single image.

LIPAs are reconfigurable and the array elements are synthesised by mechanical scanning thus they are suitable to perform ultrasonic image stitching. The remote and couplant-free nature of LIPAs make them suitable for automation and multiple arrays can be synthesised at arbitrary locations, with the relative distances known between the individual apertures, then stitched together to form a large inspected area. In this work image combination for LIPAs is demonstrated by combining 6 images produced by 6 different 2D arrays. While the individual apertures do not exceed 6 by 6 mm, the overall scan surface extends over 15 by 30 mm. Each array was synthesised over one defect of Sample C (see Fig. 2.7). This steel component was produced using the Wire Arc Additive Manufacturing (WAAM) [97], a manufacturing process which has been rapidly gaining popularity in the field of additive manufacturing. The sample had a machined scan surface, which was not polished. The depth sensitivity of a LIPA is defined by the width of the aperture, with an increased aperture leading to better sensitivity at increasing depths. The defects within the sample were located at varying depth, with certain defects located closer to the surface, while others further away. In order to ensure that defects are imaged with high sensitivity, based on the laser ultrasonic directivity and sensitivity patterns, the aperture was increased for defects at

higher depths.

For image processing, shear mode was utilised both for transmission and reception. Digital filtering centred at 4.5 MHz frequency, with a bandwidth of 250% was utilised. In this study, the images were formed utilising the TFM method without applying Phase Coherence Imaging. The image produced after the combination, using the relative distances between the arrays, can be seen in Fig. 6.12. A diagram can be seen in Fig. 6.12(B), which shows the location and size of defects (diagram not to scale), as well as the naming convention of the defects (D1 to D6). On the combined ultrasonic image (Fig. 6.12(A)), all 6 defects appear at the location corresponding to the actual location on the sample (correct defect localisation). Furthermore, the back-wall can also be identified on the individual images shown in Fig. 6.12(C,D,E), at the depth of 10 mm.

In Fig. 6.12 (C, D), artefacts can be seen under the defects, which resemble the appearance of the back-wall. These artefacts are produced by unintentionally imaging undesirable modes (mode cross-talk) [98], similar to the SAW cross-talk discussed in Section 3.2. In this case this is likely a reflected signal from the shear wave that is mode-converted to longitudinal at the back-wall of the sample. This is confirmed by the location of the artefact being 7.5 mm deep, which corresponds to the 0.75 times of the true location (averaging shear velocity to the back-wall and longitudinal velocity back to the surface, i.e.: it take 75% of the time that it would for the shear wave without mode conversion). A technique has previously been proposed that is able to suppress these artefacts [99], however, multi-modal artefact suppression is outside the scope of this PhD study.

Parameters of the synthesised arrays and their corresponding defect and their true and measured characteristics can be seen in Table 6.1. Each array utilised the an equidistant matrix array layout (Fig. 6.6) and consisted of 121 array elements. Each 2D LIPA required a data acquisition time of ~ 40 mins, leading to a total scan time of 240 mins for all six arrays. A signal averaging of 128 was used to ensure low noise levels on the A scan signals.

Defect sizing was achieved by measuring the -6 dB drop relative to the centre of each defect. The width of the isosurfaces, representing the defects, was measured in the

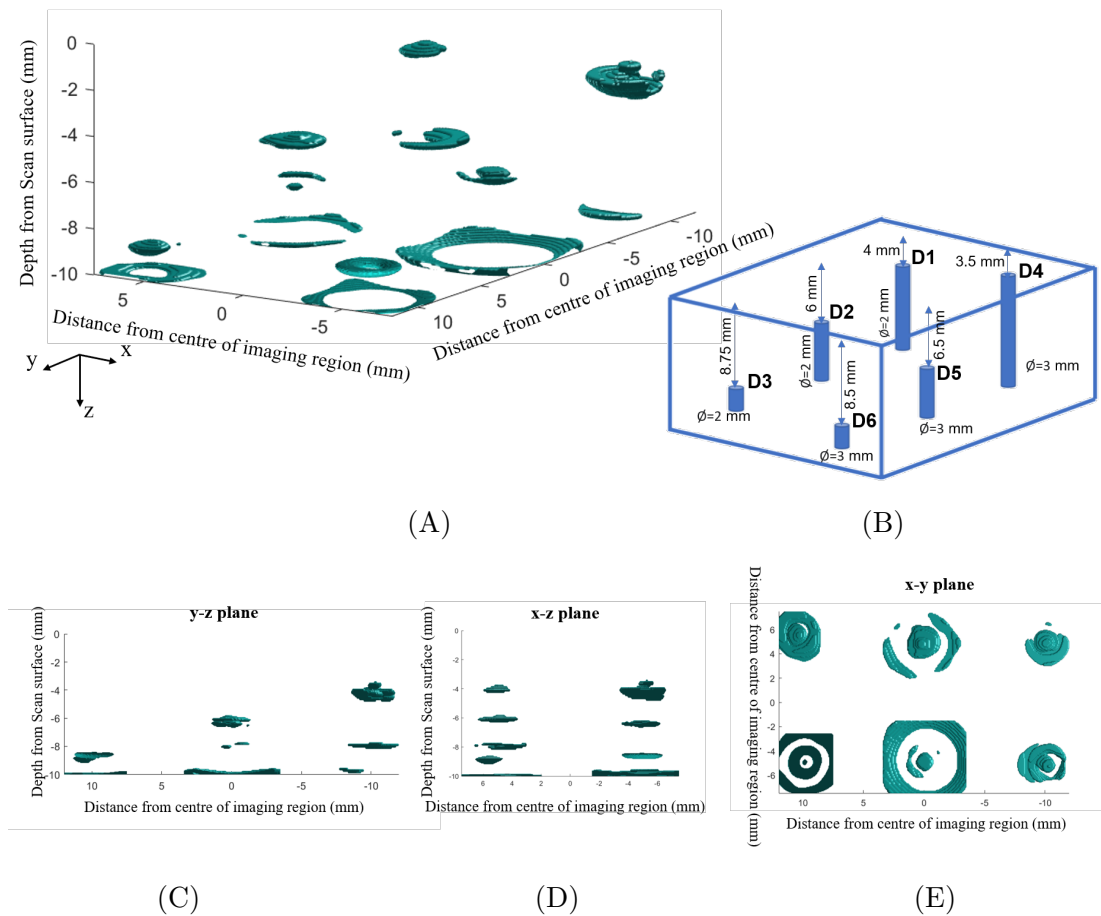


Figure 6.12: (A) Stitched ultrasonic image of 6 bottom drilled holes at varying depths; (B) Diagram of the sample; (C,D,E) image is shown from various angles as explained by x-y-z Cartesian arrows. Isosurfaces were plotted between 0 and -6 dB for all images.

x and y directions, followed by averaging these two values to produce a single averaged diameter value. Defect depth was measured by locating the tip of the isosurfaces for each defect. The true values were acquired by pouring a high resolution replicating compound (Microset - 101RF) into the defects which could then be evaluated using a caliper. Overall good agreement was observed between the true and measured values. Defect depth was measured with an average discrepancy of 0.15 mm and defect sizing with a discrepancy of 0.35 mm, relative to the true values.

The replicating compound creates an identical copy of the defects' shape, thus the resulting replicas can be used for evaluating these shapes. On Fig 6.13 the differences

	True		LIPA Measurement		Array Parameters	
	Diameter	Depth	Diameter	Depth	Aperture	Pitch
D1	2.0 mm	3.7 mm	2.0 mm	3.7 mm	3×3 mm	0.3 mm
D2	2.0 mm	5.7 mm	2.8 mm	5.8 mm	3×3 mm	0.3 mm
D3	2.2 mm	8.4 mm	1.9 mm	8.6 mm	4×4 mm	0.4 mm
D4	3.0 mm	3.4 mm	3.2 mm	3.4 mm	4.5×4.5 mm	0.45 mm
D5	3.0 mm	5.8 mm	2.7 mm	6.2 mm	5×5 mm	0.5 mm
D6	3.2 mm	8.2 mm	2.7 mm	8.4 mm	6×6 mm	0.6 mm

Table 6.1: True and measured defect sizes from ultrasonic images, with respective arrays and their parameters for defects D1-D6. Each array consisted of 121 array elements.

between the replicated shape and the 3D ultrasonic image of the defects D1 and D4 can be seen. The replicated shape shows that the top of defect D4 is shaped like a stepped pyramid. This is also shown in the ultrasonic image. The width of the top step (See d_t , highlighted by a red arrow in Fig. 6.13) of defect D4 was measured through optical means to be 1.05 mm (d_t), and using the ultrasonic sizing method described earlier, a measurement of 0.99 mm (d_m) was taken.

6.4.2 Evaluation of Array Designs

In previous subsections of this chapter, three sparse arrays have been presented: the matrix, the random and the Vernier arrays. An adaptive data acquisition has also been described for volumetric imaging, in which case a dense layout is achieved for a constrained aperture with high array sensitivity. In this section their performance is evaluated and compared. For this work, sample B (see Fig. 2.7) was utilised for volumetric imaging, concentrating on a bottom drilled hole, the tip of which was located 5 mm deep from the scan surface. The four 2D LIPAs that were experimentally synthesised can be seen on Fig. 6.14, with the array parameters shown in Table 6.2. Signal averaging of 128 was used and the total acquisition time for each array was ~ 17

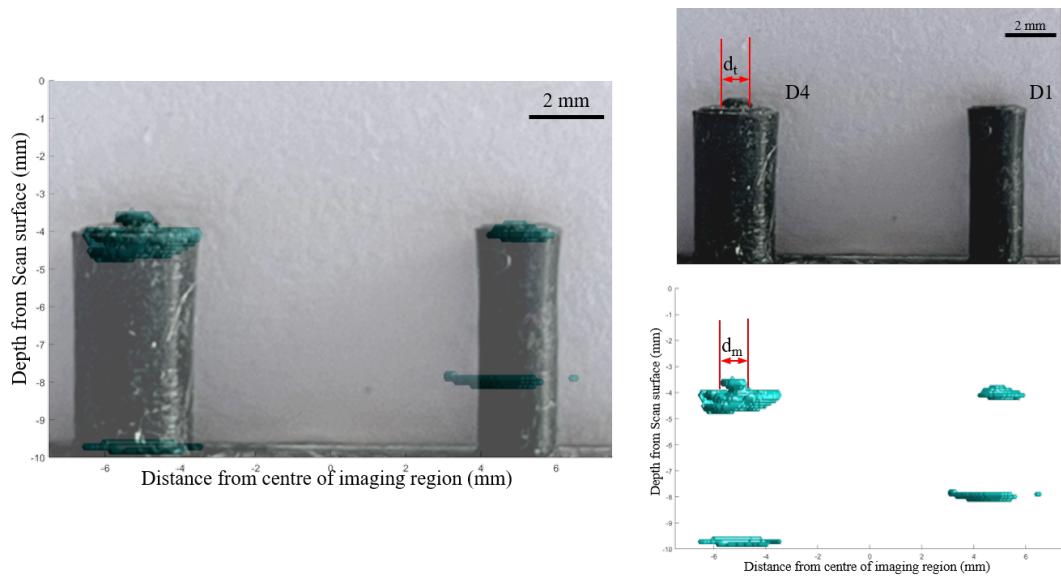


Figure 6.13: Composite image of the replicating compound poured into defects D1 and D4 (as shown on top right) and the ultrasonic image produced for these two defects in the x-z plane. On the right hand-side the two images are shown separately.

mins.

The three sparse arrays were designed to have 10×10 mm aperture. The matrix and the random array each had 121 elements in total, both for generation and detection, while the Vernier array consisted of 81 generating elements in a 9×9 element grid and 169 detection elements in a 13×13 element grid. The SMC array contained 116 elements in a circulate array pattern.

Array Design	Elements [Tx/Rx]	Pitch [Tx/Rx]	Signals Captured
Matrix Array	121/121	1 mm	14641
Random Array	121/121	Varying	14641
Vernier Array	81/169	1.25/0.83 mm	13689
SMC Array	116/116	0.3 mm	13456

Table 6.2: Array parameters for Matrix, Random, Vernier and SMC arrays

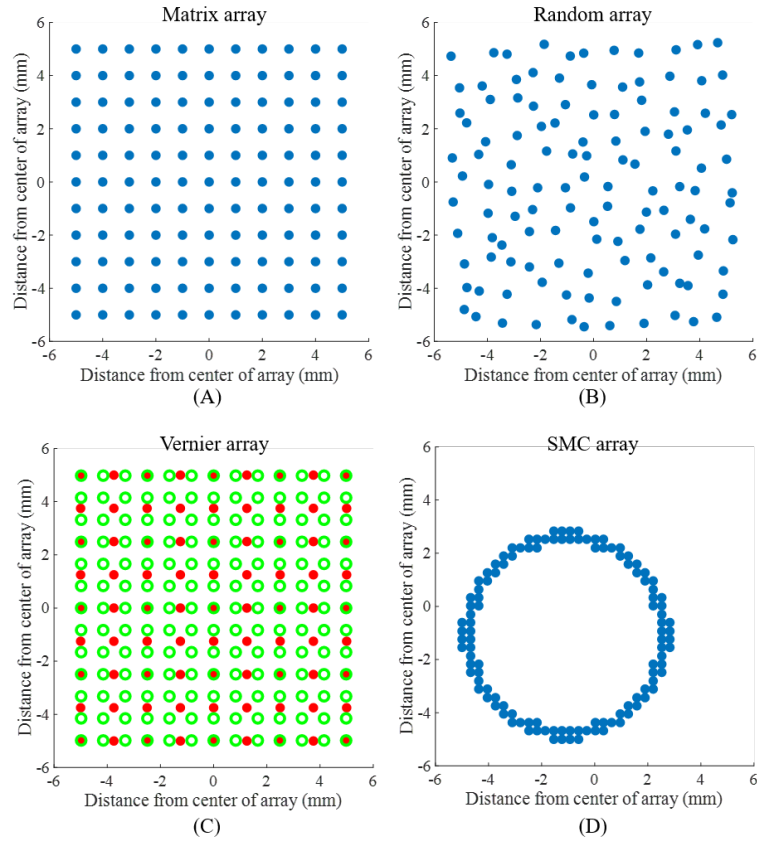


Figure 6.14: Array layouts shown for Matrix array (A), Random array (B), Vernier array (C) and the adaptive array optimised for the defect (D). Blue circles show the location of elements that both generate and detect, while red circles show location of generation elements and green circles show the location of detection elements

The digital filtering was selected to be 5 MHz with a bandwidth of 150%, a good compromise between low attenuation and high resolution. This resulted in frequency content ranging from 1.25 MHz to 8.75 MHz. At the centre frequency of 5 MHz, the acoustic wavelength was 0.65 mm for shear waves in aluminium, assuming an acoustic velocity of 3250 m/s. The inter-element spacing of the matrix array was designed to be larger than half the acoustic wavelength (under-sampled). It was 1 mm, which made it ~ 1.5 times larger than the acoustic wavelength and ~ 3 times larger than what the Nyquist sampling limit requires. These values were selected to ensure the generation of high amplitude grating lobes, in order to ease comparison of grating lobes suppression between the presented array designs.

The array directivities (not to be confused with ultrasonic generation directivities) calculated by the analytical model presented in Section 6.1 can be seen in Fig. 6.15, for each of the array designs shown in Fig. 6.14. The array directivities were calculated assuming shear velocity for aluminium, at a frequency of 5 MHz. Based on these directivities, the corresponding main lobe to grating lobe ratio was calculated and is included in Table 6.3. By analysing these calculated grating lobe levels, the matrix array is expected to produce the highest intensity artefacts. The adaptive array exhibits no grating lobes due to the dense layout, however it does produce higher amplitude side-lobes than the other arrays due to the restricted aperture. The two optimised sparse layouts, the Vernier and the random array, are shown to reduce grating lobe levels by ~ 10 dB and ~ 17.5 dB respectively.

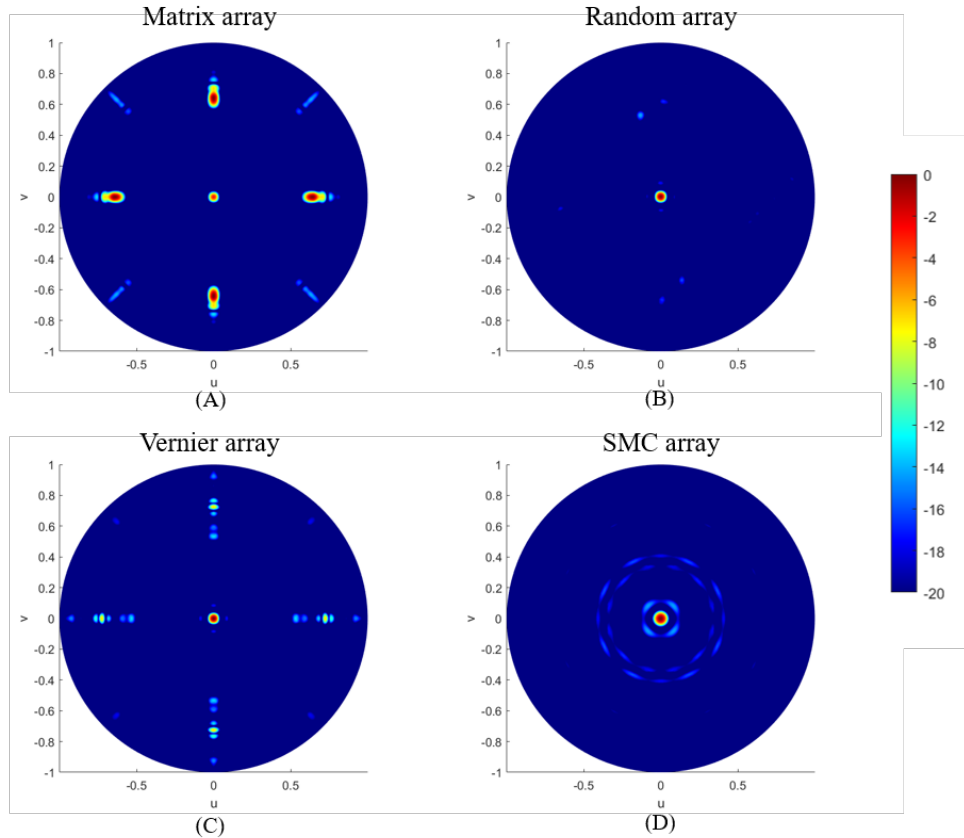


Figure 6.15: Array directivities shown for Matrix array (A), Random array (B), Vernier array (C) and the adaptive array, optimised for the known defect location (D). The dynamic range for these four directivities is indicated on the colour bar.

Array Design	Main lobe to Grating lobe Ratio
Matrix Array	-2.96 dB
Random Array	14.20 dB
Vernier Array	6.86 dB
SMC Array	No grating lobes present

Table 6.3: Table of main lobe to grating lobe ratio, calculated from analytical model

The experimental results for the above shown arrays can be seen on Fig. 6.16. For visualisation the isosurface method was selected, and the threshold was set at -12 dB, hence imaging all voxels between 0 and -12 dB. For TFM image reconstruction, the shear wave mode was utilised, and the signals were filtered at 5 MHz centre frequency, with 150 % bandwidth, as stated earlier. In the imaging process, VCF weighing was applied to enhance the images produced. Every image was normalised to its highest amplitude voxel, excluding values from the first 4 mm depth in order to ensure that the images are not normalised to the high amplitude SAW region.

Based on the ultrasonic images, the defect can be detected at 5 mm depth in the TFM images from all array designs. To analyse the images quantitatively the SNR and peak artefact values were measured. In order to evaluate the SNR, the signal was defined as the amplitude of the indication of the defect on the ultrasonic image (i.e.: 0 dB), while the noise is defined as the average of all voxels below the defect (i.e.: voxels below 5 mm). The peak artefact value is measured by taking the highest amplitude voxel within the same region, where the noise is measured. The results from this analysis can be seen on Table 6.4.

The experimental results are in good agreement with the analytical model. The random array was the most successful at suppressing grating lobes and thus reducing the effect of artefacts, and improving the overall SNR, from the three sparse array designs experimentally tested. The Vernier array offers improvements over the matrix array, however it does not achieve the same reduction in artefacts as the random array.

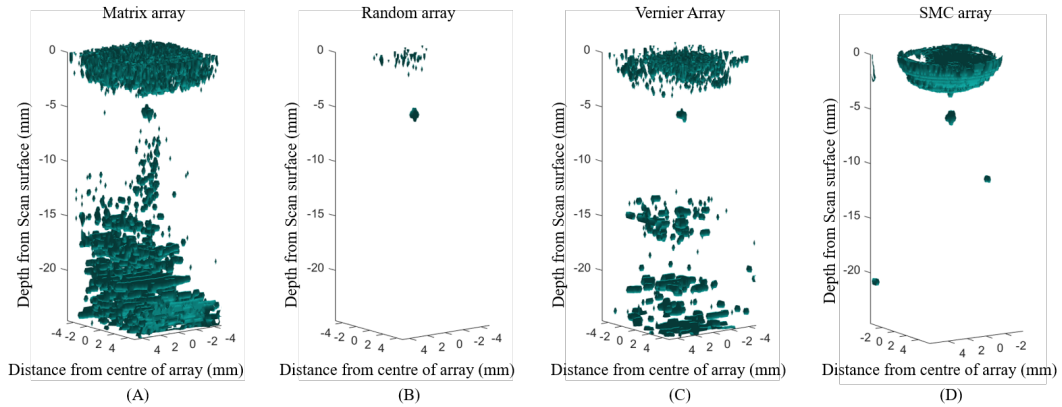


Figure 6.16: Experimental 3D images produced using Matrix array (A), Random array (B), Vernier array (C) and the adaptive array, optimised for the known defect location (D). Isosurfaces were plotted for voxels with values between 0 and -12 dB.

Array Design	SNR	Peak Artefact Amplitude
Matrix Array	26.75 dB	7.41 dB
Random Array	43.81 dB	-12.98 dB
Vernier Array	32.06 dB	1.00 dB
SMC Array	53.66 dB	-8.9 dB

Table 6.4: Signal-to-Noise Ratio and peak artefact amplitude measurements from experimental results

The SMC array was expected to not produce any grating lobe artefacts, as predicted by the analytical model, as the inter-element spacing is 0.3 mm, which is smaller than half the acoustic wavelength ($\lambda=0.65$ mm), thus the Nyquist criterion is satisfied [62]. Even though the design of the SMC array required a slight reduction of number A scan signals, it achieved the highest SNR, providing a ~ 10 dB improvement over the random array design, due to the array elements being optimised for sensitivity. Although the peak artefact value (i.e.: highest non-defect voxel) of the image produced by the SMC array was higher than that of the random array, this values are likely not artefacts produced by grating lobes, and are highly likely features caused by other modes.

An additional analysis at varying frequencies of digital filtering was done to further

compare the performance of the random array and the SMC array, as these two designs perform the best in terms of overall SNR. The aim of this comparison was to investigate the capabilities of the adaptive acquisition for 3D imaging, when compared to the sparse arrays that utilised conventional (FMC) acquisition. The results can be seen on Fig. 6.17. The VCF imaging algorithm (See Section 3.2) was applied in the overall TFM algorithm used for post-processing these results, in order to improve the SNR and suppress grating lobes. The same data-set was used as in Fig. 6.16, filtered at two frequencies: 9 MHz and 12 MHz centre frequency, both with a 150% bandwidth. For each image, isosurfaces were plotted for voxels with values between 0 and -6 dB. The SMC array is able to inspect at higher frequencies than the random array due to the smaller pitch and the optimised sensitivity.

At 12 MHz the acoustic wavelength is equal to $271 \mu\text{m}$. As the diffraction limit is one of the main governing factors of axial resolution of a conventional (i.e.: non-super resolution) ultrasonic imaging system [100], the SMC array would, in theory, enable the detection of defects as small as $135.5 \mu\text{m}$. From this we can conclude that the SMC array is able to achieve the highest maximum axial resolution, from the four array designs presented, as the other designs are not able to operate at the increased frequencies.

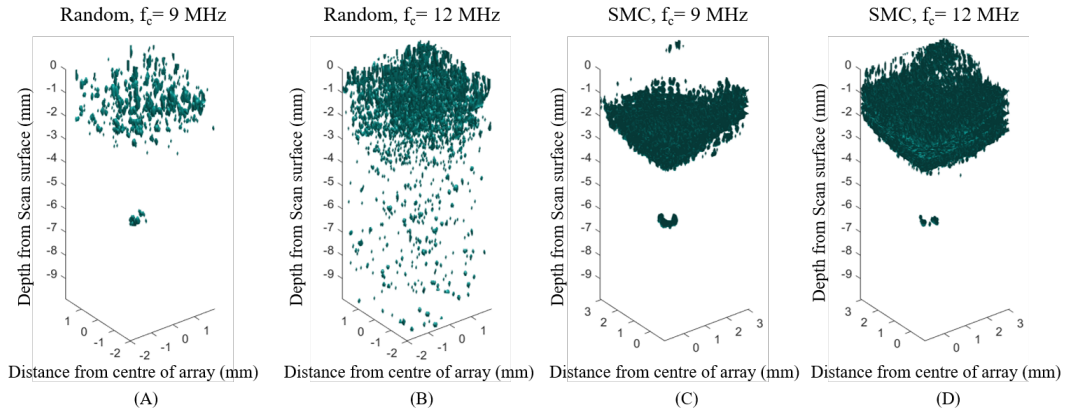


Figure 6.17: Experimental 3D images produced using Random array (A,B) and optimised SMC array (C,D) at centre frequency (f_c) of 9 MHz (A,C) and 12 MHz (B,D)

It is important to note that while the SMC array offers the best SNR and axial resolution performance, it assumes that the knowledge of the defect is known. Thus

initially a scan to determine potential defect location must be performed. This could be addressed by applying one of the three sparse arrays presented (Matrix, Random and Vernier arrays). The Random and the Vernier array were both able to improve imaging quality over the simplistic Matrix array. The Random array achieved higher SNR and lower artefact values than the Vernier array, however it is important to note that the overall performance of a Vernier array is expected to be more consistent, as the Random array is expected to provide a varying (Random) performance, in terms of grating lobe suppression, depending on the location of the defect. If sufficient time is available to optimise the random array (i.e.: evaluate performance in the analytical model, for every possible focal point), this uncertainty can be reduced, thus higher performance can be achieved, however if an array must be designed rapidly the Vernier array is expected to provide a more consistent performance. Thus the Random and the Vernier arrays offer a compromise between array design times and performance.

6.4.3 Comparison of the Conventional and Adaptive Acquisition

The concept of the Selective Matrix Capture was also adapted for volumetric imaging. The array elements of the SMC array design were optimised based on the surface projected array sensitivity, with the assumption that a sparse array has already been utilised in advance (1st stage in Section 5.2), providing information regarding to the location of the defect. For comparison, approximately the same number of elements were used by the optimised, SMC array as the matrix, Vernier and random arrays. Due to the optimised element locations, the SMC array achieved the highest SNR, with a 10 dB improvement over the random array. Furthermore, the SMC array was able to achieve the highest frequency range for imaging, which translates to the highest axial resolution. For comparison, to achieve the same inter-element spacing, and thus the same grating lobe levels, a fully populated matrix array over the 10×10 mm scan region, would require an array of 34×34 elements, or 1156 elements. Using the FMC data acquisition method, a total of 1336336 A scan signals would be captured. Assuming the same data acquisition speed as for the above shown experiments, the data acquisition time would be 22 hours and 34 mins. In comparison, using initially

a random array, followed by an optimised SMC array, a combined scan time of 34 minutes would be required, corresponding to an 45 times reduction in acquisition time data volume. These two data acquisition methods (FMC and SMC) and associated array designs are not compared experimentally for 3D imaging, because it is practically challenging to scan an array of 1156 elements due to the long acquisition time (22.5 hours). However, in Chapter 5 the FMC and SMC data acquisition methods were experimentally compared for 2D imaging where the SMC array showed a comparable performance as fully populated periodic array.

6.5 Summary

In this chapter the first 2D Laser Induced Phased Arrays was presented. The system utilised one generation and one detection laser which are independently scanned of each other. To the author's knowledge, this is the first ever remote, 2D ultrasonic phased array that is reconfigurable to any arbitrary layouts, with a differing generation and detection designs. Utilising the capabilities of scanning, and reconfigurability, LIPA imaging was demonstrated as an effective tool for image combination, where 6 defects, with varying depths and sizes were imaged. Defect localisation and sizing was performed with an accuracy of 0.15 and 0.35 mm, respectively. Furthermore the images were able to resolve the complex shapes of a non-spherical defect (non-flat drilled hole) with high accuracy.

A study was carried out into optimising 2D sparse LIPA layouts in order to suppress grating lobes, towards faster, artefact-free 3D LIPA imaging. Two designs, the random and the Vernier array were compared to the conventional, matrix array. These two sparse arrays, were designed with optimised array directivity and were shown to outperform the matrix array in terms of artefact suppression and consequently the SNR. The analysis and comparison was validated using both the analytical array directivities and the experimental 3D ultrasonic images. In addition, both the theoretical and the experimental analysis were in good agreement, as to which array (i.e.: the random array) offers superior performance out of the three sparse arrays compared. The random array achieved a ~ 17 dB improvement of SNR, and reduced the peak artefact values

from 7.41 dB to -12.98 dB, when compared to the matrix array layout. This demonstrates the possibility to optimise the performance of 2D LIPAs through array design. In future in order to further reduce acquisition speeds by improving efficiency further developments into optimised designs must be sought.

Chapter 7

Conclusions

7.1 Review of Thesis

This Thesis has investigated the capabilities of LIPAs to perform 3D imaging towards offering a technique that can address current NDE challenges, such as inspection in extreme and hazardous environments, on objects with complex geometries, and inspection in places of restricted access. A range of approaches were presented towards enabling and improving a system for 2D LIPA synthesis. From these approaches, two key advances have been the focus of this study towards the development of fast and efficient remote, 3D ultrasonic imaging: exploring novel LIPA designs and introducing a new, adaptive data acquisition method. By developing these methods, the industrial potential of 2D LIPAs was demonstrated.

Chapter 1 detailed the current need for remote volumetric imaging in the field of NDE. There is a significant need for a technique that allows for accurate defect detection and characterisation in 3D for applications where current ultrasonic imaging techniques cannot be utilised, including inspection in extreme environments, places of restricted access or on components with complex shapes. The few instances in the present literature, where laser ultrasound for volumetric imaging have been reviewed and their limitations have been identified: past attempts were not able to focus and steer in 3D in a wide range of angles, resulting in lower ultrasonic imaging quality (techniques using SAFT [41,48]). In all previous cases the Full Matrix was not captured

and TFM could not have been applied, which is currently the golden standard in NDE [14, 77, 78]. LIPAs were identified as an alternative candidate that overcome the limitations of previous techniques by the use of FMC and TFM, thus proving potential towards accurate 3D, remote imaging. Currently the slow acquisition time has been preventing the development of 2D LIPAs, thus a key aim of this study was to improve data acquisition time to the extent that would demonstrate the industrial potential of 2D LIPAs.

Chapter 2 described the experimental framework constructed for the studies presented in this Thesis. This includes the lasers, the optical components and the mechanical instrumentation (i.e.: stages and galvo mirrors). The software that was developed to control the experimental setup was also introduced. Some examples of ultrasonic imaging were presented on samples with varying surface roughness, in order to demonstrate the ability of the detector to operate on rough surfaces. Finally, the experimental samples used throughout the Thesis were described in this chapter.

The experimental setup described is capable of synthesising LIPAs on rough surfaces, however an assumption was made that samples have non-curved surfaces, such that the detection laser does not require varying focal depth to conform to curvatures. Further work will need to be carried out in order to address the need for inspection of complex components. This could be addressed by the development of a robotic LIPA system.

The theory behind Laser Induced Phased Arrays was presented in Chapter 3. This included the presentation of the laser ultrasonic generation mechanism, the properties of laser generated and detected ultrasound in the various bulk modes (shear and longitudinal waves), as well as the data acquisition and data processing used by LIPAs. In this chapter the use of phase information is proposed for LIPAs, which was demonstrated to reduce grating lobe effects for sparse arrays, and overall increase SNR for both sparse and dense arrays through the use of Phase Coherence Imaging. By doing so, the number of signals required to achieve sufficient SNR on the ultrasonic TFM images produced by LIPAs can be reduced, thereby reducing the total data acquisition time.

In Chapter 4, the concept of sparse array designs was explored for LIPAs for the first time. A model for simulating the pressure field produced by a LIPA is constructed. Using this model, the performance of LIPAs can be evaluated (e.g.: main lobe width, grating lobe level). This theoretical evaluation of the LIPA design formed the basis of the array optimisation study presented in this chapter. Three designs were compared: the conventional, equidistant, periodic array with same position for elements generating and detecting ultrasound; the random array with same position for elements generating and detecting ultrasound; and an array with the ultrasonic generation and detection position of elements optimised to each other (two-way optimised array). The analytical evaluation of the three array designs demonstrated the improvement of the two optimised arrays (random and two-way optimised) over the conventional, periodic LIPA array design. This was followed by experimental demonstration of the performance of the three arrays, where a significant improvement was achieved by the optimised arrays. The two-way optimised array and the random array achieved an SNR improvement of 10.86 and 10.83 dB respectively over the periodic array design. In addition to demonstrating the improved imaging capabilities, this study also demonstrated the reconfigurability of LIPAs. The three array designs were constructed solely through the scanning software developed during this study, rapidly synthesising arrays with arbitrary element locations, as well as arrays with different layouts for generation as detection.

The improvement in SNR achieved through grating lobe suppression achieved by the sparse LIPA designs enable LIPA imaging with reduced number of array elements. This enables faster production of LIPA imaging, leading to increased applicability where inspection time is critical, such as in the cases of in-process inspection or process monitoring.

As mentioned in Chapter 4, the highest intensity artefacts that appeared on the ultrasonic images originated mainly from the reflection of the SAWs. In this work a scan side of 50 mm was utilised, however on a larger sample the reflections would occur later in time, in which case the impact of grating lobes on the imaging quality would be reduced. This would require further studying, to the limitations of grating lobes on

LIPA imaging considering the size of the sample.

A study into a novel adaptive data acquisition strategy was proposed in Chapter 5. In this chapter, it was demonstrated that certain array elements will contribute more information to the final image than others, depending on the directivity and detection sensitivity of the array elements, and in some cases certain elements will not contribute any useful information, only noise. It logically follows that by selecting elements with the highest generation and detection sensitivity, significantly faster imaging can be achieved without degrading imaging quality. This fact was utilised to establish an adaptive acquisition method, called Selective Matrix Capture, which consisted of two stages: 1) an iterative rapid scan for locating potential defects, followed by, 2) an optimised focused scan. The first stage runs in iterations until it can confirm the presence (or absence) of defects and their location. Then, in stage 2, an optimisation method is performed in order to calculate the optimal position of elements based on the location of the defect, obtained during stage 1. Two optimisation methods were presented, one that utilised equidistant pitch, with elements located in such positions as to achieve highest generation and detection efficiency (threshold method), while the second method, utilised a varying pitch, with elements placed throughout the pre-defined, available LIPA scanned aperture (SMC-SED). Two cases were considered for the experimental demonstration: 1) where a single defect is located within a good sensitivity region, when utilising an equidistant, periodic dense array for inspection and 2) where the defect is purposefully located in a lower sensitivity region by restricting the LIPA scanned aperture. In both cases the adaptive acquisition was compared to the conventional FMC data acquisition method (i.e.: equally spaced, periodic, dense LIPA design within the entire available scan region). The defect was detected during stage 1 in both cases, while only capturing 30.4 times fewer A scan signals than the dense array design, providing information about the location of the defect for stage 2. The threshold method was demonstrated to achieve comparable (or higher) levels of SNR as in the dense array design, while utilising 17.6 times fewer A scan signals. The other optimisation method, SMC-SED achieved comparable defect imaging characterisation levels compared to the dense array, while utilising 17.6 times less data even though a 11-15

dB reduction in SNR was observed. Overall, these results demonstrate that comparable image quality can be achieved by utilising an optimised acquisition strategy compared to the conventional, non-adaptive acquisition method while capturing significantly less data. An improvement of 10 times faster data acquisition was achieved.

The optimised arrays of the adaptive acquisition method rely on the fact that defects are omni-directional point scatterers. This assumption is suitable for the defects presented in this work, cylindrical side-drilled holes. However, defects commonly encountered in the field of NDT, such as cracks, exhibit preferential scattering angles. In order to apply the adaptive data acquisition process these scattering angles must be considered in the future, to enable the application of this method for a wider range of defect types, sizes and orientations.

Another notable outcome of chapter 5, was development of an objective defect detection algorithm that can be utilised towards enabling automated defect detection. This was demonstrated by applying the method to multiple scans, and a good indication between visual detection and the proposed method was shown. While these results are very promising for the future of automation of LIPAs for NDE, this technique will have to be tested more rigorously to establish the success rate (i.e.: percentage of false positives and false negatives, compared to true positives and true negatives.).

In this work a sample with a defect was considered. However, commonly components don't contain any defects. A limitation of the proposed defect detection method is that it is only sensitive to the presence of defects and is not able to decisively confirm the lack of defects. In order to establish an algorithm that is able to identify a defect-free component, further studies must be performed that will establish the relationship between array sensitivity and the detectability of various defect types and sizes.

Finally in Chapter 6 the framework for remote, 3D ultrasonic imaging utilising LIPAs was developed and experimentally demonstrated. This included expanding the previously described data acquisition and processing algorithms from 2D imaging to 3D imaging. The analytical model previously used for array performance evaluation of 1D arrays was extended to 3D space in order to evaluate 2D arrays. The sparse array designs presented in Chapter 4 were adapted to 2D LIPAs, after which the adaptive

acquisition was also introduced for 3D imaging.

The 3D imaging capabilities of LIPAs were demonstrated on a component manufactured using the WAAM process. Six defects of varying sizes and depths were imaged by synthesising six 2D matrix LIPAs, each containing a total of 121 array elements (11×11 grid of elements). Furthermore, 3D image combination was utilised to produce a single image of the 6 defects, by accounting for the relative distances of the arrays, obtained from the scanning software. This study presented the first non-destructive, 3D laser ultrasonic images of an additively manufactured component.

Following the development of this experimental capability, the two sparse array designs, the Vernier (i.e.: generation layout different to detection layout) and the random arrays, were developed for 2D LIPAs and were experimentally demonstrated and compared to the matrix array design (i.e.: 2D periodic array with same position for generation and detection elements). It was demonstrated that artefacts were successfully suppressed, which consequently resulted in increased SNR. The random array achieved a ~ 17 dB, and the Vernier array achieved a ~ 12 dB improvement in SNR compared to the conventional, matrix array.

It is important to mention that by translating from 1D space to 2D space for sparse array design, the number of potential designs significantly increases. In this work two optimisation approaches were utilised, the Vernier and the random array, however various other array designs exist in the literature [93], which could be applied in order to further improve 2D LIPAs.

Besides implementing sparse 2D LIPAs, adaptive acquisition was also presented in this study, by optimising the array element locations (SMC array) based on the location of the defect. The defect location was assumed to be acquired from a previous scan achieved by a sparse array. The optimised adaptive scan was able to achieve a inter-element spacing for a dense SMC array with the same number of elements as the sparse arrays, thus it was able to completely eliminate the array grating lobes. This led to further enhancement of SNR of ~ 10 dB, ~ 21 dB, ~ 27 dB compared to the random, the Vernier and the matrix arrays, respectively. The advantage of this was presented by comparing the sparse array which demonstrated experimentally the highest SNR,

i.e. the random array, to the SMC array at increased frequencies, at which grating lobes appear at higher amplitudes when utilising a sparse array. It was demonstrated that the SMC array produced by the adaptive scanning was able to form images of the defect at frequency ranges 3 MHz higher than the random array, utilising the same number of array elements. The maximum frequency the SMC and the random array could utilise were 12 and 9 MHz, respectively, above which the SNR was significantly degraded by the grating lobes and the defect could no longer be visualised.

Finally, it was concluded, by extrapolating from the experimentally achieved scan times, that the scanning time for synthesising the equivalent dense 2D LIPA with the conventional matrix layout, would be ~ 22.5 hours, compared to the 34 minutes of the combined scan time of a sparse array and the consequent optimised SMC array. This comparison has demonstrated the industrial potential of 2D LIPAs for remote, ultrasonic NDE.

7.2 Recommendation for Future Work

In this Thesis the foundation for volumetric imaging using LIPAs was established. This could be advanced in various ways. An important area is to improve defect characterisation. A critical goal of 3D imaging is to achieve highly accurate defect characterisation. Currently the most accurate way for defect sizing is by measuring the Scattering matrix, from a Full Matrix Capture data-set [50,101]. Defects can be recognised and sized by observing their response at varying generation and detection angles, respective to the defect. Adopting scattering matrix evaluation to laser ultrasonics, would considerably improve the defect characterisation capabilities of Laser Induced Phased Arrays. However, this will require careful consideration of the directivity and detection sensitivity of laser generated and detected ultrasound, in order to decouple the effects of generation and detection efficiency from the scattering information. Scattering matrices have not been demonstrated for volumetric imaging, thus applying this method for 2D LIPAs would provide a 3D defect characterisation method.

Another avenue of future work to improve 2D LIPAs is to synthetically producing LIPA data, based on already acquired signals. Previously, a deep-learning based algo-

rithm has been demonstrated that was able to infill data of sparse arrays in order to synthetically produce the data as if a dense array was utilised [86]. By doing so Kumar et al. [86] were able to significantly reduce the grating lobe levels and increase overall SNR. Combining this method with the 2D sparse arrays presented in this Thesis, would reduce the data acquisition time, while comparable imaging quality could be achieved.

From the phased array improvement perspective, two optimised sparse designs were presented, the random array and the vernier array. Each design achieved grating lobe suppression through different means, the former method spread the grating lobes over the entire array directivity, while the latter optimised the generation array directivity to the detection array directivity. In future work, combining the two approaches could lead to further enhancement of the array directivity, by achieving higher suppression of grating lobes. In this approach two random designs would be utilised, one for generation and another for detection. The randomness of one layout would be specifically designed to cancel out the randomised grating lobes by the randomness of the other design. This approach would be the first time where the two concepts would be combined, as this design has not been achievable by previous 2D phased array designs, such as the transducer-based array, due to the rigidity of their configuration (i.e.: coupled generation and detection) and geometrical limitations of a transducer element.

In this Thesis an adaptive acquisition process was presented that optimised array elements based on the generation and detection efficiency for a specific defect location. This adaptive acquisition method could be improved by employing the sparse designs presented in this Thesis, for defect location, during the first stage. The sparse designs suppress grating lobes, thus their use in stage 1 could speed up the process of finding potential defects.

In this work the defect was assumed to be an ideal point reflector (i.e.: reflects ultrasound uniformly in all directions), which is an acceptable assumption when inspecting cylindrical defects, such as a side-drilled hole. This however is not true for all defects encountered in industrial applications, for example when inspecting and imaging cracks. In this case, the tips of a crack will reflect ultrasound uniformly, however the bulk of the crack will reflect ultrasound in certain directions preferentially. In future

implementations of the adaptive acquisition method, it would be useful to include coefficients that accounts for the observed scattering, making the adaptive method more efficient for imaging a wider range of defects. The first stage of the adaptive acquisition can provide indicative information regarding scattering, which can then be utilised as the basis for the coefficient.

Finally an important improvement to mention here is a technique towards eliminating the SAW cross-talk that is observed in the TFM images as mentioned in Section 3.2. A high amplitude artefact near the surface can be observed on most images presented in this Thesis (e.g. see Fig. 6.16), which is caused by the high amplitude surface waves which are generated simultaneously with the bulk waves in laser ultrasonics. The amplitude of this cross-talk region was shown to reduce by applying phase coherent imaging, however it was not fully eliminated. By developing a technique that is able to fully suppress the unwanted surface waves, the detection and imaging of near-surface defects would become less challenging for LIPAs. Some methods have been reported in the literature that are able to suppress unwanted wave modes [99, 102]. Applying these methods would improve the near-surface detection capabilities of LIPAs.

Bibliography

- [1] R. Mohammadkhani, L. Zanotti Fragonara, J. Padiyar M, I. Petrunin, J. Raposo, A. Tsourdos, and I. Gray, “Improving depth resolution of ultrasonic phased array imaging to inspect aerospace composite structures,” *Sensors*, vol. 20, no. 2, p. 559, 2020.
- [2] C. Mineo, C. MacLeod, M. Morozov, S. G. Pierce, R. Summan, T. Rodden, D. Kahani, J. Powell, P. McCubbin, C. McCubbin, *et al.*, “Flexible integration of robotics, ultrasonics and metrology for the inspection of aerospace components,” in *AIP conference proceedings*, vol. 1806, p. 020026, AIP Publishing LLC, 2017.
- [3] G. Brekow, D. Brackrock, R. Boehm, and M. Kreutzbruck, “Phased array-based saft for defect sizing on power plant components,” in *AIP Conference Proceedings*, vol. 1096, pp. 872–879, American Institute of Physics, 2009.
- [4] R. Zimmermann, E. Mohseni, R. K. Vithanage, D. Lines, E. Foster, C. N. Macleod, S. G. Pierce, G. Marinelli, S. Williams, and J. Ding, “Increasing the speed of automated ultrasonic inspection of as-built additive manufacturing components by the adoption of virtual source aperture,” *Materials & Design*, vol. 220, p. 110822, 2022.
- [5] N. Montinaro, G. Epasto, D. Cerniglia, and E. Guglielmino, “Laser ultrasonics for defect evaluation on coated railway axles,” *NDT & E International*, vol. 116, p. 102321, 2020.

Bibliography

- [6] C. Holmes, B. W. Drinkwater, and P. D. Wilcox, “Post-processing of the full matrix of ultrasonic transmit–receive array data for non-destructive evaluation,” *NDT & E International*, vol. 38, p. 701–711, 2005.
- [7] M. Marmonier, S. Robert, J. Laurent, and C. Prada, “Real-time 3d imaging with fourier-domain algorithms and matrix arrays applied to non-destructive testing,” *Ultrasonics*, vol. 124, p. 106708, 2022.
- [8] Y. Ohara, M. C. Remillieux, T. Ulrich, S. Ozawa, K. Tsunoda, T. Tsuji, and T. Mihara, “High-resolution 3d phased-array imaging of fatigue cracks using piezoelectric and laser ultrasonic system (plus),” *Japanese Journal of Applied Physics*, vol. 61, no. SG, p. SG1043, 2022.
- [9] A. Tweedie, R. L. O’Leary, G. Harvey, A. Gachagan, C. Holmes, P. D. Wilcox, and B. W. Drinkwater, “11d-2 total focussing method for volumetric imaging in immersion non destructive evaluation,” in *2007 IEEE Ultrasonics Symposium Proceedings*, pp. 1017–1020, IEEE, 2007.
- [10] R. K. Vithanage, E. Mohseni, D. Lines, C. Loukas, E. Foster, C. N. MacLeod, S. G. Pierce, A. Gachagan, J. Ding, and S. Williams, “Development of a phased array ultrasound roller probe for inspection of wire+ arc additive manufactured components,” *Journal of Manufacturing Processes*, vol. 80, pp. 765–774, 2022.
- [11] R. Zimmermann, E. Mohseni, M. Vasilev, C. Loukas, R. K. Vithanage, C. N. Macleod, D. Lines, Y. Javadi, E. E. Silva, M. Pimentel, *et al.*, “Collaborative robotic wire+ arc additive manufacture and sensor-enabled in-process ultrasonic non-destructive evaluation,” *Sensors*, vol. 22, no. 11, p. 4203, 2022.
- [12] P. D. Wilcox, “Ultrasonic arrays in nde: Beyond the B-scan,” in *AIP Conference Proceedings*, vol. 1511, pp. 33–50, American Institute of Physics, 2013.
- [13] J. G. Mckee, *Volumetric Imaging Using 2D Phased Arrays*. PhD thesis, University of Bristol, 2021.

Bibliography

- [14] A. Velichko and P. D. Wilcox, “Defect characterization using two-dimensional arrays,” in *AIP Conference Proceedings*, vol. 1335, pp. 835–842, American Institute of Physics, 2011.
- [15] J. Zhang, B. W. Drinkwater, and P. D. Wilcox, “Comparison of ultrasonic array imaging algorithms for nondestructive evaluation,” *IEEE Transactions on Ultrasonics, Ferroelectrics and Frequency Control*, vol. 60, no. 8, pp. 1732–1745, 2013.
- [16] A. Robinson, B. Drinkwater, and J. Allin, “Dry-coupled low-frequency ultrasonic wheel probes: application to adhesive bond inspection,” *NDT & E International*, vol. 36, no. 1, pp. 27–36, 2003.
- [17] R. K. Vithanage, E. Mohseni, Z. Qiu, C. MacLeod, Y. Javadi, N. Sweeney, G. Pierce, and A. Gachagan, “A phased array ultrasound roller probe for automated in-process/interpass inspection of multipass welds,” *IEEE Transactions on Industrial Electronics*, vol. 68, no. 12, pp. 12781–12790, 2020.
- [18] R. Zimmermann, E. Mohseni, D. Lines, R. K. Vithanage, C. N. MacLeod, S. G. Pierce, A. Gachagan, Y. Javadi, S. Williams, and J. Ding, “Multi-layer ultrasonic imaging of as-built wire+ arc additive manufactured components,” *Additive Manufacturing*, vol. 48, p. 102398, 2021.
- [19] J. G. McKee, R. L. Bevan, P. D. Wilcox, and R. E. Malkin, “Volumetric imaging through a doubly-curved surface using a 2D phased array,” *NDT & E International*, vol. 113, p. 102260, 2020.
- [20] P. B. Kosel, G. S. Munro, and R. Vaughan, “Capacitive transducer for accurate displacement control,” *IEEE Transactions on Instrumentation and Measurement*, no. 2, pp. 114–123, 1981.
- [21] J. Isla and F. Cegla, “EMAT phased array: A feasibility study of surface crack detection,” *Ultrasonics*, vol. 78, pp. 1–9, 2017.

Bibliography

- [22] L. Pucci, R. Raillon, L. Taupin, and F. Baqué, “Design of a phased array emat for inspection applications in liquid sodium,” *Sensors*, vol. 19, no. 20, p. 4460, 2019.
- [23] J. Parra-Raad and F. Cegla, “On the steerability of phased array EMATs: The dipole element,” *NDT & E International*, vol. 125, p. 102563, 2022.
- [24] C. B. Scruby and L. E. Drain, *Laser ultrasonics: techniques and applications*. Adam Hilger, 1990.
- [25] J.-R. Lee, H.-J. Shin, C. C. Chia, D. Dhital, D.-J. Yoon, and Y.-H. Huh, “Long distance laser ultrasonic propagation imaging system for damage visualization,” *Optics and Lasers in Engineering*, vol. 49, no. 12, pp. 1361–1371, 2011.
- [26] C. Calder, E. Draney, and W. Wilcox, “Noncontact measurement of the elastic constants of plutonium at elevated temperatures,” *Journal of Nuclear Materials*, vol. 97, no. 1-2, pp. 126–136, 1981.
- [27] C.-H. Yeh, N. Jeyaprakash, and C.-H. Yang, “Non-destructive characterization of elastic properties on steel plate using laser ultrasound technique under high-temperature atmosphere,” *The International Journal of Advanced Manufacturing Technology*, vol. 108, no. 1, pp. 129–141, 2020.
- [28] E. J. Alles, S. Noimark, E. Zhang, P. C. Beard, and A. E. Desjardins, “Pencil beam all-optical ultrasound imaging,” *Biomedical Optics Express*, vol. 7, no. 9, pp. 3696–3704, 2016.
- [29] C. Pei, K. Demachi, T. Fukuchi, K. Koyama, and M. Uesaka, “Cracks measurement using fiber-phased array laser ultrasound generation,” *Journal of Applied Physics*, vol. 113, no. 16, p. 163101, 2013.
- [30] R. J. Colchester, C. Little, G. Dwyer, S. Noimark, E. J. Alles, E. Z. Zhang, C. D. Loder, I. P. Parkin, I. Papakonstantinou, P. C. Beard, *et al.*, “All-optical rotational ultrasound imaging,” *Scientific Reports*, vol. 9, no. 1, pp. 1–8, 2019.

Bibliography

- [31] J. Chen, J. Xiao, D. Lisevych, and Z. Fan, “Laser-induced full-matrix ultrasonic imaging of complex-shaped objects,” *IEEE Transactions on Ultrasonics, Ferroelectrics and Frequency Control*, vol. 66, no. 9, pp. 1514–1520, 2019.
- [32] Z. Wan, Y. Ling, Z. Hongchao, *et al.*, “Laser ultrasonic testing for inspection of curved surface samples based on synthetic aperture focusing,” in *Journal of Physics: Conference Series*, vol. 1654, p. 012094, IOP Publishing, 2020.
- [33] M.-H. Noroy, D. Royer, and M. Fink, “The laser-generated ultrasonic phased array: Analysis and experiments,” *The Journal of the Acoustical Society of America*, vol. 94, no. 4, pp. 1934–1943, 1993.
- [34] T. Murray, J. Deaton Jr, and J. Wagner, “Experimental evaluation of enhanced generation of ultrasonic waves using an array of laser sources,” *Ultrasonics*, vol. 34, no. 1, pp. 69–77, 1996.
- [35] A. Blouin, D. Levesque, C. Neron, D. Drolet, and J.-P. Monchalain, “Improved resolution and signal-to-noise ratio in laser-ultrasonics by saft processing,” *Optics Express*, vol. 2, no. 13, pp. 531–539, 1998.
- [36] C. Scruby, “Some applications of laser ultrasound,” *Ultrasonics*, vol. 27, no. 4, pp. 195–209, 1989.
- [37] D. Cerniglia, M. Scafidi, A. Pantano, and J. Rudlin, “Inspection of additive-manufactured layered components,” *Ultrasonics*, vol. 62, pp. 292–298, 2015.
- [38] K.-N. Ying, C.-Y. Ni, L.-N. Dai, L. Yuan, W.-W. Kan, and Z.-H. Shen, “Multi-mode laser-ultrasound imaging using time-domain synthetic aperture focusing technique (T-SAFT),” *Photoacoustics*, p. 100370, 2022.
- [39] X. Kou, C. Pei, T. Liu, S. Wu, T. Liu, and Z. Chen, “Noncontact testing and imaging of internal defects with a new laser-ultrasonic saft method,” *Applied Acoustics*, vol. 178, p. 107956, 2021.
- [40] V. Schmitz, S. Chakhlov, and W. Müller, “Experiences with synthetic aperture focusing technique in the field,” *Ultrasonics*, vol. 38, no. 1-8, pp. 731–738, 2000.

Bibliography

- [41] D. Lévesque, A. Blouin, C. Néron, and J.-P. Monchalin, “Performance of laser-ultrasonic f-saft imaging,” *Ultrasonics*, vol. 40, no. 10, pp. 1057–1063, 2002.
- [42] D. Lévesque, Y. Asaumi, M. Lord, C. Bescond, H. Hatanaka, M. Tagami, and J.-P. Monchalin, “Inspection of thick welded joints using laser-ultrasonic saft,” *Ultrasonics*, vol. 69, pp. 236–242, 2016.
- [43] F. Bentouhami, B. Campagne, E. Cuevas, T. Drake, M. Dubois, T. Fraslin, P. Piñeiro, J. Serrano, and H. Voillaume, “LUCIE-A flexible and powerful laser ultrasonic system for inspection of large cfrp components,” in *2nd International Symposium on Laser Ultrasonics, Talence (France)*, 2010.
- [44] K. Zhang, Z. Zhou, and L. Ma, “Research on a laser ultrasound method for testing the quality of a nuclear radiation protection structure,” *Measurement Science and Technology*, vol. 28, no. 2, p. 025204, 2016.
- [45] S.-C. Hong, A.-D. Abetew, J.-R. Lee, and J.-B. Ihn, “Three dimensional evaluation of aluminum plates with wall-thinning by full-field pulse-echo laser ultrasound,” *Optics and Lasers in Engineering*, vol. 99, pp. 58–65, 2017.
- [46] E. J. Alles, N. Fook Sheung, S. Noimark, E. Z. Zhang, P. C. Beard, and A. E. Desjardins, “A reconfigurable all-optical ultrasound transducer array for 3D endoscopic imaging,” *Scientific Reports*, vol. 7, no. 1, pp. 1–9, 2017.
- [47] X. Zhang, J. R. Fincke, C. M. Wynn, M. R. Johnson, R. W. Haupt, and B. W. Anthony, “Full noncontact laser ultrasound: first human data,” *Light: Science & Applications*, vol. 8, no. 1, pp. 1–11, 2019.
- [48] C.-Y. Ni, C. Chen, K.-N. Ying, L.-N. Dai, L. Yuan, W.-W. Kan, and Z.-H. Shen, “Non-destructive laser-ultrasonic synthetic aperture focusing technique (SAFT) for 3D visualization of defects,” *Photoacoustics*, vol. 22, p. 100248, 2021.
- [49] T. Stratoudaki, M. Clark, and P. D. Wilcox, “Laser induced ultrasonic phased array using full matrix capture data acquisition and total focusing method,” *Optics Express*, vol. 24, no. 19, pp. 21921–21938, 2016.

Bibliography

- [50] J. Zhang, B. W. Drinkwater, and P. D. Wilcox, “Defect characterization using an ultrasonic array to measure the scattering coefficient matrix,” *IEEE Transactions on Ultrasonics, Ferroelectrics and Frequency Control*, vol. 55, no. 10, pp. 2254–2265, 2008.
- [51] P. D. Wilcox, C. Holmes, and B. W. Drinkwater, “Advanced reflector characterization with ultrasonic phased arrays in nde applications,” *IEEE Transactions on Ultrasonics, Ferroelectrics and Frequency Control*, vol. 54, no. 8, pp. 1541–1550, 2007.
- [52] D. Pieris, T. Stratoudaki, Y. Javadi, P. Lukacs, S. Catchpole-Smith, P. D. Wilcox, A. Clare, and M. Clark, “Laser induced phased arrays (LIPA) to detect nested features in additively manufactured components,” *Materials & Design*, vol. 187, p. 108412, 2020.
- [53] P. Thayer, “Enabling the fourth industrial revolution (4ir) and the role of nde and monitoring,” *Insight, Non-Destructive Testing and Condition Monitoring*, vol. 59, no. 9, pp. 469–472, 2017.
- [54] B. Pouet, S. Breugnot, and P. Clémenceau, “An innovative interferometer for industrial laser ultrasonic inspection,” in *AIP Conference Proceedings*, vol. 760, pp. 273–280, American Institute of Physics, 2005.
- [55] T. Blum, B. Pouet, S. Breugnot, and P. Clémenceau, “Non-destructive testing using multi-channel random-quadrature interferometer,” in *AIP Conference Proceedings*, vol. 975, pp. 239–246, American Institute of Physics, 2008.
- [56] D. Pieris, *Towards in-process inspection of additive manufacturing using laser ultrasonics*. PhD thesis, University of Nottingham, 2022.
- [57] J. Zhang, B. W. Drinkwater, and P. D. Wilcox, “Longitudinal wave scattering from rough crack-like defects,” *IEEE Transactions on Ultrasonics, Ferroelectrics and Frequency Control*, vol. 58, no. 10, pp. 2171–2180, 2011.

Bibliography

- [58] J. Zhang, B. Drinkwater, and P. Wilcox, “Comparison of the inspections of smooth and rough crack-like defects using ultrasonic arrays,” in *AIP Conference Proceedings*, vol. 1335, pp. 843–850, American Institute of Physics, 2011.
- [59] J. R. Bernstein and J. B. Spicer, “Line source representation for laser-generated ultrasound in aluminum,” *The Journal of the Acoustical Society of America*, vol. 107, no. 3, pp. 1352–1357, 2000.
- [60] L. Rose, “Point-source representation for laser-generated ultrasound,” *The Journal of the Acoustical Society of America*, vol. 75, no. 3, pp. 723–732, 1984.
- [61] G. Miller and H. Pursey, “The field and radiation impedance of mechanical radiators on the free surface of a semi-infinite isotropic solid,” *Proceedings of the Royal Society of London. Series A. Mathematical and Physical Sciences*, vol. 223, no. 1155, pp. 521–541, 1954.
- [62] S. C. Wooh and Y. Shi, “Optimum beam steering of linear phased arrays,” *Wave Motion*, vol. 29, pp. 245–265, 1999.
- [63] J. Camacho, M. Parrilla, and C. Fritsch, “Phase coherence imaging,” *IEEE Transactions on Ultrasonics, Ferroelectrics and Frequency Control*, vol. 56, no. 5, pp. 958–974, 2009.
- [64] J. Camacho, C. Fritsch, J. Fernandez-Cruza, and M. Parrilla, “Phase coherence imaging: Principles, applications and current developments,” in *Proceedings of Meetings on Acoustics ICU*, vol. 38, p. 055012, Acoustical Society of America, 2019.
- [65] J. Camacho, D. Atehortua, J. Cruza, J. Brizuela, and J. Ealo, “Ultrasonic crack evaluation by phase coherence processing and TFM and its application to online monitoring in fatigue tests,” *NDT & E International*, vol. 93, pp. 164–174, 2018.
- [66] J.-H. Lee and S.-W. Choi, “A parametric study of ultrasonic beam profiles for a linear phased array transducer,” *IEEE Transactions on Ultrasonics, Ferroelectrics and Frequency Control*, vol. 47, no. 3, pp. 644–650, 2000.

Bibliography

- [67] N. Budyn, R. L. Bevan, J. Zhang, A. J. Croxford, and P. D. Wilcox, “A model for multiview ultrasonic array inspection of small two-dimensional defects,” *IEEE Transactions on Ultrasonics, Ferroelectrics and Frequency Control*, vol. 66, no. 6, pp. 1129–1139, 2019.
- [68] G. R. Lockwood, P.-C. Li, M. O’Donnell, and F. S. Foster, “Optimizing the radiation pattern of sparse periodic linear arrays,” *IEEE Transactions on Ultrasonics, Ferroelectrics and Frequency Control*, vol. 43, no. 1, pp. 7–14, 1996.
- [69] H. Hu, J. Du, C. Ye, and X. Li, “Ultrasonic phased array sparse-tfm imaging based on sparse array optimization and new edge-directed interpolation,” *Sensors*, vol. 18, no. 6, p. 1830, 2018.
- [70] A. Velichko and A. Croxford, “Strategies for data acquisition using ultrasonic phased arrays,” *Proceedings of the Royal Society A: Mathematical, Physical and Engineering Sciences*, vol. 474, no. 2218, p. 20180451, 2018.
- [71] E. J. Alles and A. E. Desjardins, “Source density apodization: Image artifact suppression through source pitch nonuniformity,” *IEEE Transactions on Ultrasonics, Ferroelectrics and Frequency Control*, vol. 67, no. 3, pp. 497–504, 2019.
- [72] L. Yongfen, J. Shengchang, and L. Yanming, “Phased-ultrasonic receiving-planar array transducer for partial discharge location in transformer,” *IEEE Transactions on Ultrasonics, Ferroelectrics and Frequency Control*, vol. 53, no. 3, pp. 614–622, 2006.
- [73] Q. Xie, S. Cheng, F. Lü, and Y. Li, “A new sparse design method on phased array-based acoustic emission sensor for partial discharge detection,” *Measurement Science and Technology*, vol. 25, no. 3, p. 035102, 2014.
- [74] P. Hoen, “Aperture apodization to reduce the off-axis intensity of the pulsed-mode directivity function of linear arrays,” *Ultrasonics*, vol. 20, pp. 231–6, 1982.

Bibliography

- [75] A. Tweedie, V. Murray, and G. Hayward, “Aperiodic and deterministic 2D phased array structures for ultrasonic imaging,” in *2009 IEEE International Ultrasonics Symposium*, pp. 406–409, IEEE, 2009.
- [76] W. J. Hendricks, “The totally random versus the bin approach for random arrays,” *IEEE Transactions on Antennas and Propagation*, vol. 39, no. 12, pp. 1757–1762, 1991.
- [77] L. Lin, H. Cao, and Z. Luo, “Total focusing method imaging of multidirectional cfrp laminate with model-based time delay correction,” *NDT & E International*, vol. 97, pp. 51–58, 2018.
- [78] L. Le Jeune, S. Robert, P. Dumas, A. Membre, and C. Prada, “Adaptive ultrasonic imaging with the total focusing method for inspection of complex components immersed in water,” in *AIP Conference proceedings*, vol. 1650, pp. 1037–1046, American Institute of Physics, 2015.
- [79] N. Brierley, R. A. Smith, N. Turner, R. Culver, T. Maw, A. Holloway, O. Jones, and P. D. Wilcox, “Advances in the UK towards NDE 4.0,” *Research in Nondestructive Evaluation*, vol. 31, no. 5-6, pp. 306–324, 2020.
- [80] P. Beckmann, “Rayleigh distribution and its generalizations,” *Radio Science Journal of Research NBS/USNC-URSI*, vol. 68, no. 9, pp. 927–932, 1964.
- [81] R. F. Wagner, “Statistics of speckle in ultrasound B-scans,” *IEEE Trans. Sonics & Ultrason.*, vol. 30, no. 3, pp. 156–163, 1983.
- [82] M. V. Felice, A. Velichko, and P. D. Wilcox, “Accurate depth measurement of small surface-breaking cracks using an ultrasonic array post-processing technique,” *NDT & E International*, vol. 68, pp. 105–112, 2014.
- [83] E. J. Alles, S. Noimark, E. Maneas, W. Xia, E. Z. Zhang, P. C. Beard, I. P. Parkin, and A. E. Desjardins, “Source density apodisation in 2D all-optical ultrasound imaging,” in *2017 IEEE International Ultrasonics Symposium (IUS)*, pp. 1–4, IEEE, 2017.

Bibliography

- [84] M. Ingram, C. Mineo, A. Gachagan, A. J. Mulholland, A. Nordon, and M. Hegarty, “Determination of bubble size distribution using ultrasound array imaging,” *IEEE Transactions on Ultrasonics, Ferroelectrics and Frequency Control*, vol. 67, no. 7, pp. 1424–1437, 2020.
- [85] R. Clark, “Rail flaw detection: overview and needs for future developments,” *NDT & E International*, vol. 37, no. 2, pp. 111–118, 2004.
- [86] V. Kumar, P.-Y. Lee, B.-H. Kim, M. Fatemi, and A. Alizad, “Gap-filling method for suppressing grating lobes in ultrasound imaging: Experimental study with deep-learning approach,” *IEEE Access*, vol. 8, pp. 76276–76286, 2020.
- [87] A. Velichko, E. L. Villaverde, and A. J. Croxford, “Local scattering ultrasound imaging,” *Scientific reports*, vol. 11, no. 1, pp. 1–11, 2021.
- [88] J. Zhang, B. W. Drinkwater, and P. D. Wilcox, “The use of ultrasonic arrays to characterize crack-like defects,” *Journal of Nondestructive Evaluation*, vol. 29, no. 4, pp. 222–232, 2010.
- [89] G. Davis, R. Nagarajah, S. Palanisamy, R. A. R. Rashid, P. Rajagopal, and K. Balasubramaniam, “Laser ultrasonic inspection of additive manufactured components,” *The International Journal of Advanced Manufacturing Technology*, vol. 102, no. 5, pp. 2571–2579, 2019.
- [90] G. Lockwood and F. S. Foster, “Optimizing sparse two-dimensional transducer arrays using an effective aperture approach,” in *Proceedings of IEEE Ultrasonics Symposium*, vol. 3, pp. 1497–1501, IEEE, 1994.
- [91] S. N. Ramadas, J. C. Jackson, J. Dziewierz, R. O’Leary, and A. Gachagan, “Application of conformal map theory for design of 2-D ultrasonic array structure for ndt imaging application: A feasibility study,” *IEEE Transactions on Ultrasonics, Ferroelectrics and Frequency Control*, vol. 61, no. 3, pp. 496–504, 2014.
- [92] A. Tweedie, *Spiral 2D array designs for volumetric imaging*. PhD thesis, University of Strathclyde, 2011.

Bibliography

- [93] A. Austeng and S. Holm, “Sparse 2-D arrays for 3-D phased array imaging-design methods,” *IEEE Transactions on Ultrasonics, Ferroelectrics and Frequency Control*, vol. 49, no. 8, pp. 1073–1086, 2002.
- [94] E. J. Alles, *An Axial Array for Volumetric Intravascular Ultrasound Imaging*. PhD thesis, 2012.
- [95] D. H. Turnbull and F. S. Foster, “Beam steering with pulsed two-dimensional transducer arrays,” *IEEE Transactions on Ultrasonics, Ferroelectrics and Frequency Control*, vol. 38, no. 4, pp. 320–333, 1991.
- [96] R. White, “Elastic wave scattering at a cylindrical discontinuity in a solid,” *The Journal of the Acoustical Society of America*, vol. 30, no. 8, pp. 771–785, 1958.
- [97] S. W. Williams, F. Martina, A. C. Addison, J. Ding, G. Pardal, and P. Colegrove, “Wire+ arc additive manufacturing,” *Materials science and technology*, vol. 32, no. 7, pp. 641–647, 2016.
- [98] R. L. Bevan, J. Zhang, N. Budyn, A. J. Croxford, and P. D. Wilcox, “Experimental quantification of noise in linear ultrasonic imaging,” *IEEE Transactions on Ultrasonics, Ferroelectrics and Frequency Control*, vol. 66, no. 1, pp. 79–90, 2018.
- [99] S. Cantero-Chinchilla, P. D. Wilcox, and A. J. Croxford, “A deep learning based methodology for artefact identification and suppression with application to ultrasonic images,” *NDT & E International*, vol. 126, p. 102575, 2022.
- [100] J. de Rosny and M. Fink, “Overcoming the diffraction limit in wave physics using a time-reversal mirror and a novel acoustic sink,” *Physical Review Letters*, vol. 89, no. 12, p. 124301, 2002.
- [101] L. Bai, A. Velichko, and B. W. Drinkwater, “Ultrasonic characterization of crack-like defects using scattering matrix similarity metrics,” *IEEE Transactions on Ultrasonics, Ferroelectrics and Frequency Control*, vol. 62, no. 3, pp. 545–559, 2015.

Bibliography

- [102] N. Paul, P. Kassis, A. Ferre, A. Schumm, and P.-E. Lhuillier, “Ultrasound array probe: Signal processing in case of structural noise,” *Journal of Nondestructive Evaluation, Diagnostics and Prognostics of Engineering Systems*, pp. 1–14, 2020.